Applied Physics Reviews

REVIEW ARTICLE | MARCH 27 2024

Nonlinear optics at epsilon near zero: From origins to new materials

Dhruv Fomra ; Adam Ball ; Samprity Saha ; Jingwei Wu ; Md. Sojib ; Amit Agrawal ; Henri J. Lezec; Nathaniel Kinsey

Appl. Phys. Rev. 11, 011317 (2024)
https://doi.org/10.1063/5.0186961

Applied Physics Reviews REVIEW pubs.aip.org/aip/are

Nonlinear optics at epsilon near zero: From origins to new materials

Cite as: Appl. Phys. Rev. **11**, 011317 (2024); doi: 10.1063/5.0186961
Submitted: 9 November 2023 · Accepted: 15 February 2024 ·
Published Online: 27 March 2024 · Corrected: 2 April 2024

Dhruv Fomra,[1,2] Adam Ball,[3] Samprity Saha,[3] Jingwei Wu,[3] Md. Sojib,[3] Amit Agrawal,[2] Henri J. Lezec,[2] and Nathaniel Kinsey[3,a)]

AFFILIATIONS

[1]Department of Chemistry and Biochemistry, University of Maryland, College Park, Maryland 20742, USA
[2]Physical Measurement Laboratory, National Institute of Standards and Technology, Gaithersburg, Maryland 20899, USA
[3]Department of Electrical and Computer Engineering, Virginia Commonwealth University, Richmond, Virginia 23284, USA

[a)]Author to whom correspondence should be addressed: nkinsey@vcu.edu

ABSTRACT

In the continuously evolving realm of nonlinear optics, epsilon near zero (ENZ) materials have captured significant scientific interest, becoming a compelling focal point over the past decade. During this time, researchers have shown extraordinary demonstrations of nonlinear processes such as unity order index change via intensity dependent refractive index, enhanced second harmonic generation, saturable absorption in ultra-thin films and more recently, frequency shifting via time modulation of permittivity. More recently, remarkable strides have also been made in uncovering the intricacies of ENZ materials' nonlinear optical behavior. This review provides a comprehensive overview of the various types of nonlinearities commonly observed in these systems, with a focus on Drude based homogenous materials. By categorizing the enhancement into intrinsic and extrinsic factors, it provides a framework to compare the nonlinearity of ENZ media with other nonlinear media. The review emphasizes that while ENZ materials may not significantly surpass the nonlinear capabilities of traditional materials, either in terms of fast or slow nonlinearity, they do offer distinct advantages. These advantages encompass an optimal response time, inherent enhancement of slow light effects, and a broadband characteristic, all encapsulated in a thin film that can be purchased off-the shelf. The review further builds upon this framework and not only identifies key properties of transparent conducting oxides that have so far made them ideal test beds for ENZ nonlinearities, but also brings to light alternate material systems, such as perovskite oxides, that could potentially outperform them. We conclude by reviewing the upcoming concepts of time varying physics with ENZ media and outline key points the research community is working toward.

TABLE OF CONTENTS

I. INTRODUCTION

The study of the interaction between light and matter is a fundamental process that underpins many technologies and scientific disciplines, including communication, sensing, imaging, and more recently, quantum computing. From the ancient use of mirrors and prisms to the modern development of lasers and optical fibers, humans have always sought to manipulate light to their advantage. However, the ability to control light–matter interaction is often limited by the intrinsic properties of materials, such as their refractive index, absorption, and dispersion. More recently, various techniques have been developed to enhance, manipulate, and control the interaction between light and matter, such as plasmonics,[1–3] metamaterials,[4–8] photonic crystals,[9,10] and epsilon-near-zero (ENZ) systems.[11] Plasmonics, for example, involves the coupling of electromagnetic waves (EM) to the motion of free electrons on the surface of metals, to confine and enhance EM fields at the nanoscale. Metamaterials, on the other hand, are artificial structures that exhibit exotic optical properties not found in natural materials, such as negative refractive index,[12,13] hyperbolic dispersion,[14,15] and cloaking.[5,16,17]

In recent years, ENZ systems have emerged as another promising platform for enhancing the interaction between light and matter. ENZ systems are characterized by a vanishingly small value of their permittivity ($|\mathrm{Re}\{\varepsilon\}| \leq 1$), which leads to peculiar optical properties, such as enhanced electric field (E-field), slow light, wavelength expansion, alongside diverging group and phase velocities.[18] While the ENZ condition is only focused on the $|\mathrm{Re}\{\varepsilon\}|$, large losses, given by $\mathrm{Im}\{\varepsilon\}$, can often limit the effects. Due to this, several works focus on minimizing not only $|\mathrm{Re}\{\varepsilon\}|$, but also the $\mathrm{Im}\{\varepsilon\}$, leading to a vanishingly small refractive index, or near-zero-index (NZI) condition. Initial attempts to build a material with less than unity index date back to the 1950s, when their use was proposed for antenna applications for enhancing microwave radiation directivity.[19] However, the interest in systems with tailored permittivity and permeability, including but not limited to ENZ, took off in the early 2000s after pioneering works by Engheta and co-workers.[20–25] These works explored ENZ systems for their whole host of peculiar properties such as resonance pinning,[26] photon tunneling,[23,27] supercoupling,[24] enhanced control over emission,[20] and extreme nonlinear interactions.[28,29] Out of these, nonlinear optics plays a critical role in a broad set of applications, such as telecommunications, spectroscopy, biomedical imaging, and more recently, quantum computing and communication,[30,31] making it particularly interesting.

Given the inherent ability of ENZ systems to achieve benefits such as slow light propagation,[32] field confinement,[33] ultrafast response,[28] and relaxed phase matching conditions,[34,35] they have been heavily explored for their nonlinear properties[29,36–38] over the last decade. While earlier works focused on the large magnitude of the intensity-dependent refractive nonlinearities,[28,39] more recently the focus has shifted to understanding the mechanism and intricacies of the nonlinearity,[40–42] while expanding the capabilities using nanostructured materials and specialized excitation conditions.[43–45] This review provides a summary of the various types of nonlinearities observed in ENZ media, elucidates the role of dispersion in enhancing nonlinearities, and contextualizes ENZ systems within the larger landscape of nonlinear optical materials. More specifically, Sec. II provides an overview of nonlinearities and various enhancement mechanisms, namely, intrinsic and extrinsic. Section III introduces ENZ systems and details the role of dispersion in the enhancement of nonlinearities using a Drude-based homogenous film, as an example. Section IV provides a detailed review of the nonlinear mechanisms in homogenous ENZ systems, followed by Sec. V, which gives an overview of nonlinearities in structured ENZ media. The review ends with Sec. VI, which highlights emerging materials and applications for ENZ systems, followed by concluding remarks.

The goal of this review is to bridge the gap between the optics and materials research communities. While transparent conducting oxides are a well-studied class of materials and have been tailored for several optoelectronic applications, they have only recently been explored for their nonlinearities under the ENZ condition. Due to this, the most readily available films, ITO and doped ZnO, have been the most widely used.[28,32,39,46,47] However, now that the community has a better understanding of the mechanism behind the enhanced nonlinearities within ENZ media, the possibility of developing new materials that are tailored for enhanced nonlinearities is wide open. In this sense, for readers new to this area, Secs. II–V provide details of the nonlinear mechanism, and for readers well-versed with ENZ nonlinearities, Sec. VI provides trends in emerging materials and applications.

II. NONLINEAR OPTICAL RESPONSE OF MATERIALS

Nonlinear optics has been a captivating field of study since the 1960s and was sparked by the invention of the laser. Since then, a whole host of material systems have been explored for nonlinear processes such as harmonic generation, frequency mixing, intensity-dependent refractive index, multi-photon absorption, self- and cross-phase modulation, and others.[48,49] Typically, these materials exhibit a nearly instantaneous, but weak optical nonlinearity arising from the strong polarization of the electron cloud by an incident field. This can be modeled using an anharmonic potential which describes the binding potential $U(r)$ of an electron in a chemical bond, of size a and binding energy U_o[48,50] [Fig. 1(a)]. Upon the application of weak electric fields, the electron oscillates near the bottom of the potential, which is parabolic. This gives rise to a linear electron displacement for a given applied field. Upon the application of stronger electric fields, the electron moves further away from the bottom of the potential and reaches the non-parabolic region, where the electron displacement is no longer linearly proportional to the applied field. This, however, requires electrons to be displaced on the scale of a, which necessitates the application of electric fields on the order of atomic electric field, given by $\mathcal{E}_0 \approx U_0/qa$, where q is the electron charge Considering that the binding energy for most materials is a few eV and the inter-atomic distance is between 0.16 and 0.21 nm, atomic fields are on the order of $\approx 10^{11}$ V/m.[51] Hence, electron polarization-driven nonlinearities are typically

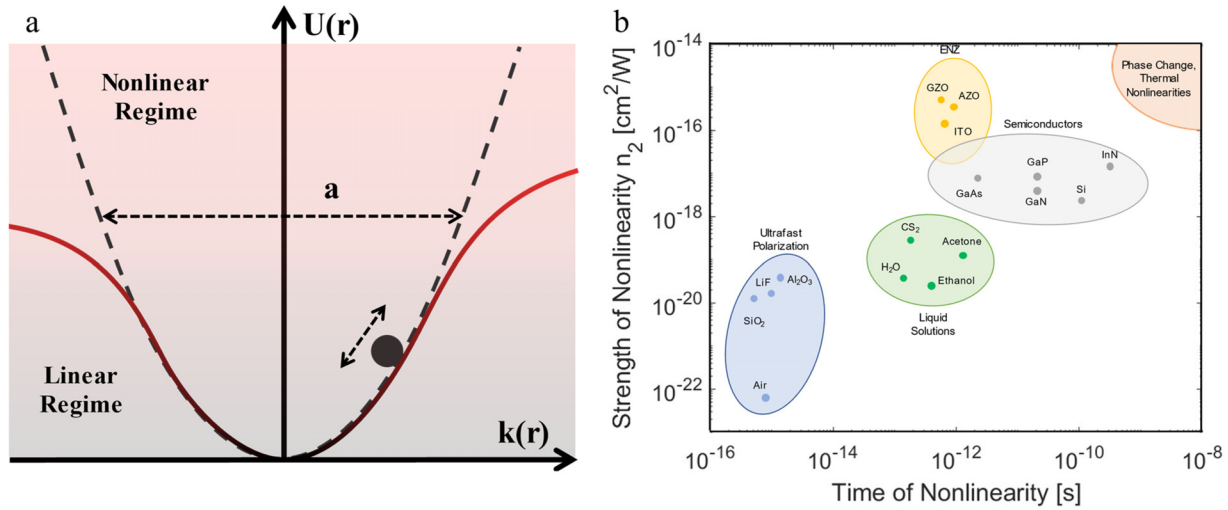

FIG. 1. (a) Anharmonic potential modeling the instantaneous nonlinearity exhibited by a polarized electron cloud. (b) Strength of a third order nonlinearities, characterized by n_2 (or similar nonlinear response) vs the characteristic time of various materials. These are an order of magnitude estimates and depict an increasingly strong nonlinearity as the characteristic time reduces. [Ga:ZnO (GZO), Al:ZnO (AZO), and $In_xSn_{1-x}O_3$ (ITO)].

weak (e.g., they require strong electric fields to generate). Despite this fact, these processes have been key enablers of wide-ranging applications, such as optical frequency combs, optical rectification, nonlinear imaging techniques, parametric oscillators, supercontinuum sources, and others for decades.[52] However, new materials with stronger nonlinear responses, whose optical properties can be significantly altered by a low-power optical field, are highly desired to achieve devices with advanced functionalities, especially for burgeoning applications such as terahertz switching and routing, single/entangled photon generation, high-efficiency frequency conversion, and quantum repeaters for communication.[53–55] To do so, researchers have explored several methods, which can be broadly categorized into two categories: intrinsic and extrinsic factors.[56] The role of the intrinsic and extrinsic factors can be distinguished by describing the nonlinear coefficient $\chi^{(3)} = EF \times \chi_o^{(3)}$, where $\chi_o^{(3)}$ is the intrinsic nonlinearity of the material and process at play (e.g., the nonlinearity of the electron potential well) and EF (extrinsic factor) is any applicable extrinsic factor enhancement (e.g., multiple round trips enabled due to the nonlinear material residing inside a cavity).

A. Intrinsic factors

The intrinsic nonlinearity represents the inherent internal nonlinearity of the process at hand. In our example, the nonlinearity of the electron potential is represented by a third-order nonlinear coefficient $\chi_o^{(3)}$, which is a material- and process-specific property. As such, it can be altered by shifting the material or nonlinear process being used. For electronic polarization nonlinearities, $\chi_o^{(3)}$ can be increased by moving to materials with smaller band gaps, since it is inversely proportional to the bandgap of a material.[57] Larger bandgap materials are typically strongly bound (high U_o) and have a short inter-atomic distance (small a). This results in a stronger inter-atomic field ($\mathcal{E}_o$), necessitating larger incoming electric fields to drive the electron into the nonlinear regime, and thus leading to a smaller nonlinear coefficient compared to narrower bandgap materials. For example, the transparent region of fused silica in the near infrared (NIR) exhibits a $\chi^{(3)}$ on the order of 10^{-22} m^2/V^2, vs that of Si which is on the order of 10^{-20} m^2/V^2.[48]

The magnitude of the intrinsic nonlinearity is also dictated by the nonlinear process that is exploited. Shifting, for example, from electronic polarization (virtual transitions) to e-h pair generation (real transitions) for nonlinear control of the refractive index can result in substantial modifications to the nonlinear coefficient. Based on the anharmonic oscillator model, the change in the index is proportional to the energy density stored or absorbed within a material.[48,50] In the case of absorption-driven effects (often the case near a resonance), this leads to the approximation $\Delta n(\omega) \approx \alpha(\omega) n(\omega) I\tau / 2NU_o$, where $\Delta n(\omega)$ is the optically induced index change, $n(\omega)$ is the linear refractive index, and $\alpha(\omega)$ is the absorption coefficient all at ω, I is excitation irradiance, τ is the characteristic time of the nonlinearity (e.g., recombination time), N is the density of states, and U_o is the binding energy.[50,58] Other than the irradiance of light I, τ is the only parameter in this expression that can be varied by orders of magnitude. This implies that moving to nonlinearities with a longer characteristic time results in a larger nonlinear effect—a well-known effect.[50]

Real transitions achieve this as carriers must move between physical states, and thus require a finite amount of time to return to equilibrium. The characteristic time of real transitions in various materials can vary between femtoseconds, for intra-band processes, and milliseconds for thermal diffusion processes, thus resulting in a comparably large range for their respective nonlinear index coefficients n_2. This coefficient, which describes the linear dependence of the refractive index n on optical intensity I (according to $n = n_o + n_2 I$) follows a typical bandwidth-strength trade-off [Fig. 1(b)]. As an example, above-bandgap nonlinearities (real transitions), given by $\chi^{(3)}$, in semiconductors such as Si and GaAs are ≈ 4 orders of magnitude larger than non-resonant nonlinearities (virtual transitions) of fused silica, as well as ≈ 4 orders of magnitude slower.

If the characteristic time τ is fixed, obtaining stronger index tuning via intrinsic effects is relegated to increasing peak irradiance, I, or

optimizing application-specific parameters such as the interaction length to maximize an induced phase shift, $\Delta\Phi_{NL} = \Delta n k_o L$. Indeed, over the past several decades, millimeter-scale and longer nonlinear crystals have been utilized along with high-power lasers to enable several applications such as parametric oscillation generation and amplification, Kerr-based mode locking, ultra-fast pulse shaping, and more.

B. Extrinsic factors

Beyond the ability to modify an intrinsic nonlinearity through material or process, extrinsic factors such as employing structure or tailored excitation schemes are complementary tools that can increase the overall efficiency of a nonlinear process. The primary objectives in leveraging these factors include enhancing the field intensity, increasing the interaction length, and introducing strong dispersion.

One example of extrinsically enhanced NL is using high-Q ring resonators (or Fabry Perot cavities), fabricated using materials such as fused silica, Si_3N_4, or MgF_2 to generate frequency combs.[59] Low power onset (≈ 3 mW) of frequency combs in these structures is primarily achievable due to the large Q-factor, even though these materials do not possess large nonlinear coefficients.[60–62] Several round trips of the photon across the ring resonator increases the interaction length, thus leading to a higher effective nonlinearity. Another method of enhancing nonlinearity is by using slow light in highly dispersive media, where the transit time is given by $\tau_{tr} = Ln_g/c$. Here L is the length, and the n_g is the group index, which can be quite large in highly dispersive media such as near the band edge of a photonic crystal,[63,64] in the vicinity of bound plasmonic surface modes,[65,66] or in the case of structures displaying Fano resonances.[67] Yet another method entails enhancing the local electric field and optical intensity through the use of structures such as plasmonic waveguides or nanoantennas.[68–70] Practically, however, systems of choice usually rely on a combination of increasing the interaction time, enhancing the electric field, and engineering slow light via strong dispersion. Over the last decade, several sophisticated resonant schemes have been explored such as electromagnetically induced transparency, several nanoantennae and metasurfaces, bound states in the continuum, anapoles, and topological modes.[71–75]

Although many efforts rightfully blur the distinction between intrinsic and extrinsic effects using a measured $\chi^{(3)}$ of the system for simplicity (e.g., treating it as a black box), it is useful to distinguish extrinsic effects from the intrinsic nonlinearity to compare materials and gain insight into optimization techniques. This is because extrinsic effects can always be employed to improve the overall efficiency of a nonlinear process whether it be naturally occurring such as group velocity enhancement due to a high material index, or by design such as employing a cavity, but they do not fundamentally modify the intrinsic nonlinearity of a material. For example, operating a nonlinear switch made of silicon near the critical angle is a useful tool to improve the absolute change in reflection/transmission, but this specific excitation scenario does not modify the intrinsic nonlinear coefficient of silicon. It simply improves the sensitivity of the approach to the induced nonlinear modifications.

While extrinsic factors have been incredibly successful in improving the overall efficiency of nonlinear processes, the success generally comes at the cost of increased complexity, higher cost, and quite often limited spectral bandwidth. As a result, one generally benefits from using a material or process with a higher intrinsic nonlinearity restricted by limits on loss and the desired speed, while extrinsic factors can be employed to further tailor the process to specific application conditions. It is in exactly this sense, ENZ materials are unique because they offer several of these extrinsic benefits naturally and do so without a significant impact on the spectral bandwidth of operation.[18,56]

III. EPSILON-NEAR-ZERO SYSTEMS

Vanishingly small permittivity can be realized in several ways, which can be broadly categorized into two categories: natural materials which exhibit ENZ locally (sub-wavelength), and structured materials which exhibit an effective ENZ condition (over several wavelengths). As an example, we consider materials that exhibit ENZ homogenously via the collective resonance of free carriers near the plasma frequency. The optical properties of these materials (such as metals and doped semiconductors), that have a large free carrier density (1×10^{19}–$5 \times 10^{22}\,\mathrm{cm}^{-3}$) are often described by the Drude model,[76] yielding a relative permittivity of

$$\varepsilon(\omega) = \varepsilon_\infty - \frac{\omega_p^2}{\omega^2 + i\Gamma\omega}, \tag{1}$$

where ε_∞ is the high-frequency permittivity contribution, ω_p is the plasma frequency, and Γ is the damping rate. The plasma frequency is related to the density of free carriers, N_c, the electron charge, q, and the electron effective mass, m^*, according to

$$\omega_p^2 = \frac{N_C q^2}{\varepsilon_0 m^*}. \tag{2}$$

Most metals or metallic compounds, such as Au, Ag, Al, TiN, and ZrN, exhibit a crossover in the UV to visible spectral range.[77–88] While some, such as transition metal nitrides, offer large tunability of the crossover wavelength, all of these are accompanied by high losses ($\mathrm{Im}\{\varepsilon\} > 0.5$) and high carrier scattering rates.[85,89–91] This limits their applicability and has led to only limited demonstrations of enhanced nonlinearities due to ENZ effects.[92–94] In contrast, transparent conducting oxides (TCO) such as doped In_2O_3, ZnO, and CdO, have been heavily explored for their nonlinearities.[28,39,95–97] These materials exhibit lower carrier densities, on the order of $\approx 10^{20}\,\mathrm{cm}^{-3}$–$\approx 10^{21}\,\mathrm{cm}^{-3}$. Therefore, the crossover wavelength occurs in the near to mid-infrared (MIR) spectral range and exhibits lower losses due to reduced scattering rates,[98–102] and the realization of NZI properties.

To illustrate the benefit to nonlinear properties of introducing the ENZ point, Fig. 2(a) plots the permittivity of doped ZnO in the NIR spectrum and compares it to fused silica and nominally undoped ZnO. The third order susceptibilities of ZnO[103] and fused silica[104] are $\chi^{(3)} \approx 5 \times 10^{-20}$ and $\approx 5 \times 10^{-22}\,\mathrm{m}^2\,\mathrm{V}^{-2}$, respectively. While two orders of magnitude apart, they follow the scaling law of $\chi^{(3)} \propto E_g^{-1}$ (observed in dispersion free spectral regions),[105] due to which the difference in third order nonlinearity is expected. However, doping of ZnO with Al ions increases the free carrier density from $\approx 10^{18}$ to $5 \times 10^{20}\,\mathrm{cm}^{-3}$. This results in the NIR spectrum being dominated by the Drude response, which introduces strong dispersion into a region that otherwise would have very little. Consequently, electromagnetic energy at wavelengths corresponding to ENZ spectral region experiences a confluence of several peculiar effects, such as a slow group velocity due to large dispersion, enhanced electric field within the ENZ media, and relaxed phase matching conditions in sub-wavelength films

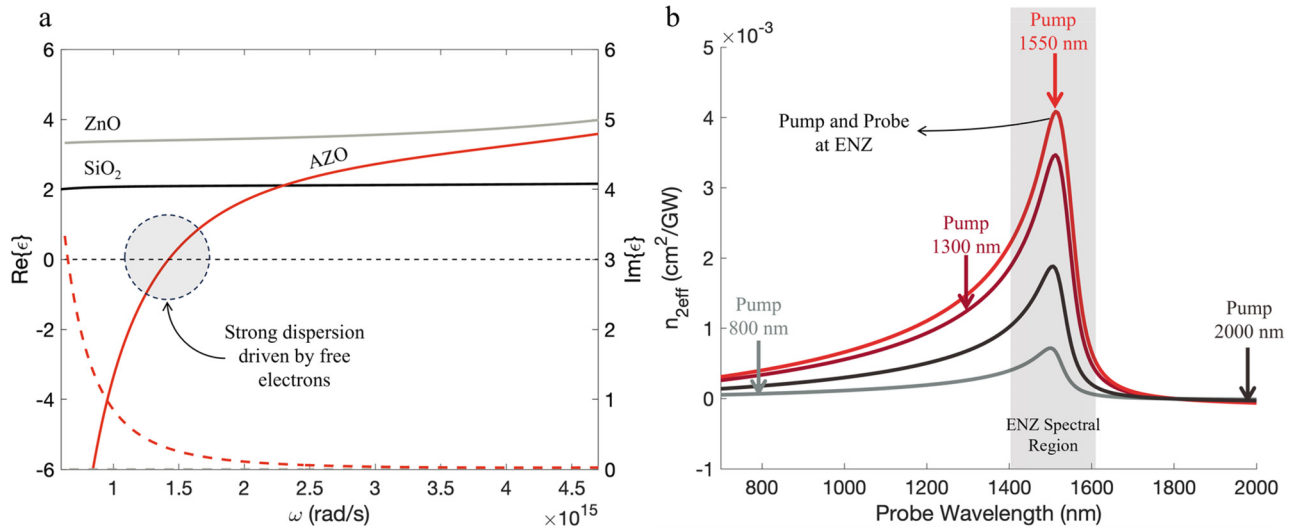

FIG. 2. (a) Free electrons induce strong dispersion in a region otherwise minimal change in the index while exhibiting low carrier scattering induced optical losses. (b) Predicted values of the n_2 coefficient of Al-doped ZnO (AZO), when pumped at four different wavelengths (800, 1300, 1550, and 2000 nm) and probed from 700 to 2000 nm. The largest enhancement is observed when the pump and the probe are within the ENZ region, defined here as the spectral range spanning a range of ±100 nm about the crossover wavelength.

due to a small n (more details to follow). These lead to enhanced nonlinearity, as seen by an enhanced effective intensity dependent refractive index (IDRI) coefficient $n_{2,eff}$, when an ENZ material is pumped and probed in the ENZ spectral region [Fig. 2(b)]. The change in refractive index as a function pump intensity I is given by $\Delta n = n_{2,eff} I$.

A. Electric field enhancement

The most intuitive ENZ effect is the local field enhancement which follows from the boundary condition of the electric field ($\mathcal{E}$) at the interface of different media. At a source-free boundary, the tangential electric field remains the same ($\mathcal{E}_{||1} = \mathcal{E}_{||2}$) and the electric field component normal to the interface must fulfill the relation $\varepsilon_1 \mathcal{E}_{\perp 1} = \varepsilon_2 \mathcal{E}_{\perp 2}$ to maintain the continuity of electric flux density. Following this, as the permittivity of one material approaches zero, the normal electric field within this material must increase to maintain equality while the tangential field component remains unaffected. As a result, there is an overall increase in the magnitude of $\mathcal{E}$ within the ENZ layer. Since the condition occurs at the boundary it extends to films of thickness much smaller than the skin depth, facilitating subwavelength confinement [Fig. 3(a)].[18] However, for free space applications, the reflection coefficient begins to dominate, especially at large angles, minimizing the amount of light entering the material and reducing the enhancement effect. This field enhancement within an ENZ medium can provide a significant improvement to the overall nonlinear response since it is intrinsically related to powers of the electric field ($P_{NL} = \chi^{(2)}\mathcal{E}^2 + \chi^{(3)}\mathcal{E}^3 + \cdots$).[29,39,106] This effect is also robust and applies even in the case when loss in the material is quite high (e.g., $\mathrm{Im}\{\varepsilon\} > 2$, achieving ENZ but not NZI). However, since only the field normal to the interface is affected, leveraging this effect in free space requires illuminating the sample at an off-normal incidence angle, which typically comes at the cost of reduced transmission due to the large index contrast experienced between air and the near-zero permittivity condition.

B. Relaxed phase matching

The ENZ condition also enables a large increase in the phase velocity, $v_p = \omega/k = c/n$, where smaller values of refractive index n result in an "expanded" wavelength $\lambda_{ENZ} = \lambda_o/n$ [Fig. 3(b)]. In the case of very small optical loss in the ENZ material, such that $\to 0$, the wavevector k also tends to zero. This results in minimal phase accumulation throughout the ENZ medium which effectively transforms light waves into spatially static or "DC" fields.[11] Minimization of phase accumulation aids in relaxing the phase-matching condition for nonlinear processes, such as second harmonic frequency generation or four-wave mixing,[34] where maintaining phase matching is a necessary condition to prevent destructive interference of the nonlinear fields as they propagate through a medium. Within ENZ media, the lack of phase accumulation throughout the propagation length greatly relaxes this constraint irrespective of incoming photon direction. This stands in contrast to traditional methods which typically achieve phase matching only in a specific direction [Fig. 3(c)].[11] However, all waves participating in the nonlinear process must belong to the ENZ region to retain the advantage of phase matching (e.g., for a second-order process $k_{1,ENZ} \pm k_{2,ENZ} = k_{3,ENZ} \approx 0$). This is practically challenging to accomplish due to the bandwidth limitation of the ENZ condition in homogenous materials [see, for example, Fig. 2(a)]. In fact, if this is not achieved phase mismatch may be exacerbated.

C. Naturally strong dispersion

Achieving ENZ naturally generates dispersion in the spectral vicinity. This is consequential when considering the group velocity ($v_g = \partial\omega/\partial k$), which governs the energy and information transfer velocity. When dispersion is strong, v_g becomes very small, leading to

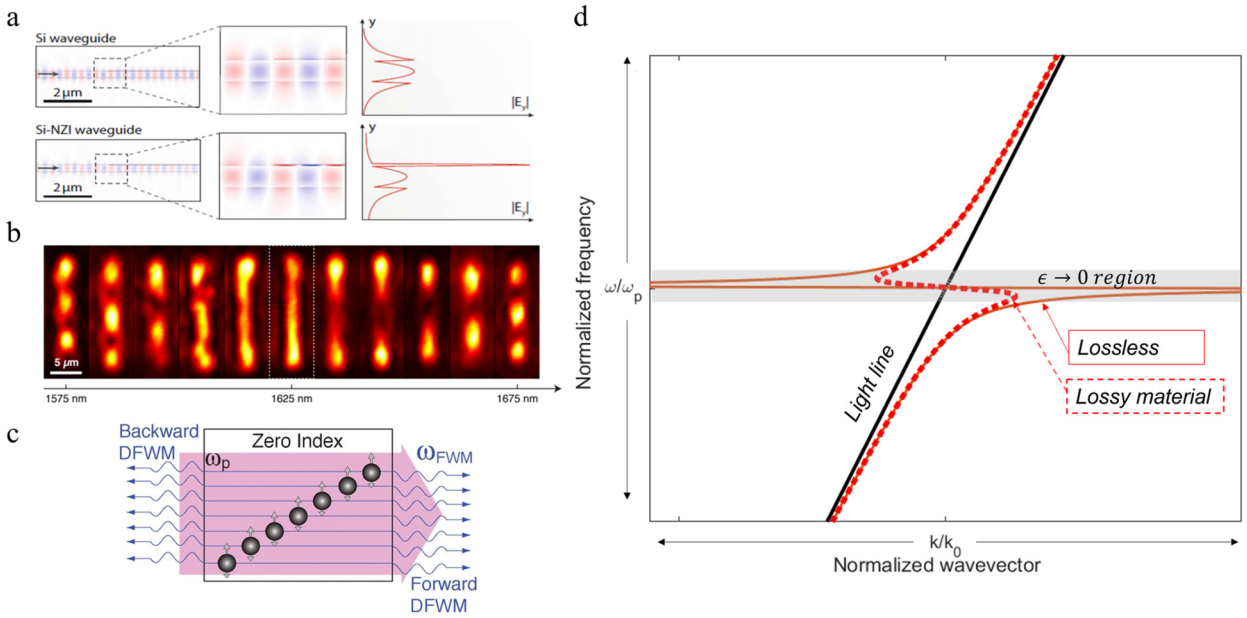

FIG. 3. Depictions of various effects associated with an ENZ condition. (a) Enhancement of normal field component observed in a hybrid (zero index material layer on top of Silicon) waveguide compared to a pure dielectric waveguide. The ENZ layer, placed on top of the waveguide, induces a strong field confinement at the interface of the layers.[18] Reproduced with permission from Kinsey *et al.*, Nat. Rev. Mater. **4**(12), 742–760 (2019). Copyright 2019 Springer Nature Limited. (b) An experimental demonstration of wavelength expansion effect observed at an ENZ condition. The excitation of counterpropagating modes over a range of wavelengths through a metamaterial-based waveguide leads to interference nodes, the distance between which is proportional to the effective wavelength of the medium. As the input approaches near zero effective index condition, the node length expands, and effective wavelength tends to be infinity (≈ 1627 nm). The figure shows this interference of nodes across the length of the waveguide for a range of wavelengths.[107] Reproduced with permission from Reshef *et al.*, ACS Photonics **4**(10), 2385–2389 (2017). Copyright 2017 American Chemical Society. (c) Theoretically, in a nonlinear four wave mixing process within an ENZ medium, sources acquire no phase as they propagate, guaranteeing a constructive interference and an increase in the signal in both directions. Panel (c) shows a general four wave mixing process (DFWM).[34] Reproduced with permission from Suchowski *et al.*, Science **342**(6163), 1223–1226 (2013). Copyright 2013 The American Association for the Advancement of Science. (d) General dispersion relation of an ENZ material under lossless and lossy conditions. As the frequency of the mode approaches the ENZ resonance, the slope of $d\omega/dk$ approaches zero marking the slow light region. However, material loss decreases the extent of flat dispersion, thus limiting the effective group index to a finite value.

the phenomenon known as "slow light."[108–111] As shown in the ω-k dispersion plot of a homogeneous ENZ medium [Fig. 3(d)], the strong dispersion near the permittivity crossover produces a minimal slope ($\partial\omega/\partial k \to 0$) and thus a reduced group velocity that is limited only by the loss within the material. The reduced group velocity then enhances the nonlinear interaction, as photons spend increased time inside the material, $\tau_{\text{prop}} = L/v_g$.[110,111] Slow light also contributes to enhancing the electric field and energy density $u = I_O/v_g$ because of energy compression in the slow propagation region.

D. Nonlinearity enhancement through combination of intrinsic and extrinsic factors

The three mechanisms mentioned above act as extrinsic factors that enhance the nonlinearity of the ENZ medium. What is intriguing is that they occur naturally in homogeneous ENZ materials, such as doped ZnO, without the need for complex design and fabrication. At the same time, common homogeneous ENZ materials are fundamentally wide bandgap semiconductors, and the introduction of the ENZ condition via strong doping [Fig. 2(a)] unlocks real transitions in the ENZ region via free carrier interactions that would otherwise be prohibited (e.g., $\hbar\omega \ll \mathcal{E}_g$). Intense light excitation is then able to modify the free carrier density N_c via interband excitation, or the effective mass m^* of free carriers within the conduction band via intraband excitation, leading to a change in $\varepsilon(\omega)$ according to Eqs. (1) and (2) (see Sec. IV for more details). These processes have been shown to have a characteristic time on the order of 0.1–1 ps and are naturally stronger than virtual transitions due to their finite relaxation time. Thus, the nonlinearity of homogeneous ENZ films is not only extrinsically enhanced but also intrinsically strong.

This unique combination of natural intrinsic and extrinsic enhancement has led to some spectacular demonstrations of index change, reaching the order of unity over the last decade.[39] Furthermore, the fact that the ENZ region is passively tunable across a wide spectrum by controlling material deposition,[98,99,112] actively tunable via electrically gating with a capacitive structure,[68,113,114] and dynamically tunable by pumping the materials optically (in both UV and IR regions),[115] has resulted in the widespread popularity of Drude-based homogeneous materials in device demonstrations.[114,116–118] However, the introduction of the ENZ condition via doping introduces optical losses and only provides enhancement over a limited bandwidth spectral region near the permittivity crossover.

In this sense, ENZ is not a "free" enhancement, and the cost of utilizing it should be weighed within the scope of a desired application (see the paragraph "Slow Free Carrier, Intraband Nonlinearities" in Sec. IV for details). In many cases, the broad nature of the ENZ region

(≈400 nm bandwidth in the 1–2 μm spectral window) does not severely limit applications. Similarly, while the losses typically limit the interaction length to less than 1 μm, the absolute nonlinearity (third harmonic efficiency or $\Delta R, \Delta T$) can be comparable to or higher than bulk material platforms.[29,39,93]

E. Alternative ENZ approaches

As a concluding note for this section, it is important to point out that ENZ in naturally occurring materials can also be achieved through the interaction of light with bound electron motion, lattice vibrations, or molecular vibrations. All these responses can be modeled using a Lorentz oscillator, which represents physical processes such as interband, band edge absorptions, and vibrational resonances. For example, one important such process is surface phonon polariton (SPhP) excitation in polar dielectric crystals. Such polarons result from atomic vibrations generated from the interaction between polar optical phonons and long wavelength irradiation in the mid-IR (e.g., for SiC) to sub-10 THz regions (e.g., for GaAs, and CaF_2), within the well-known Reststrahlen band, i.e., between longitudinal (LO) and transverse optic (TO) phonon frequencies.[119,120] If the strength of the resonance is sufficient, it can result in a spectral region where the permittivity is negative (Fig. 4). The Reststrahlen band is characterized by exceptionally low losses due to the slow scattering rates of optical phonons, which typically occur on the timescale of picoseconds, in comparison to the faster scattering of free carrier plasmons.[120,121] Moreover, upon TO phonon resonance the permittivity crosses zero once again (from negative to positive, Fig. 4). While intriguing due to the extreme dispersion, this epsilon-near-pole (ENP) region is also characterized by an extremely high loss, which limits applications.[120]

Although phononic ENZ materials, or some of the more recently explored organic ENZ materials,[122–124] have commonalities with free-carrier ENZ materials in the linear regime,[125] the nonlinear processes at play are fundamentally distinct owing to the stark difference between phonons, polarons, and free carriers (e.g., the presence of a restoring force). The remainder of this review is focused on free-electron effects, but additional information on phononic ENZ materials can be found in a recent review by Foteinopoulou *et al.*[126]

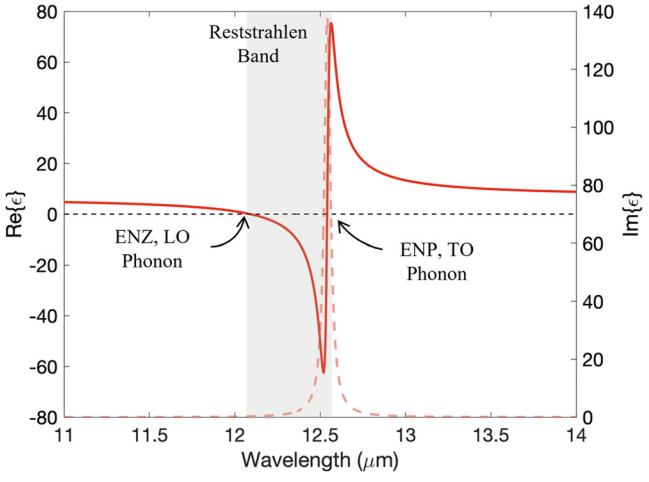

FIG. 4. Lorentz-induced ENZ response observed in SiC due to phonons. Adapted from Ref. 120.

IV. DRUDE-BASED ENZ MEDIA

Section IV A provides details into the nonlinear processes exhibited by Drude-based ENZ materials, broadly categorized into two categories, those having fast and slow nonlinearities. Fast nonlinearities encompass instantaneous (typically sub ≈1 fs)[127] processes like electronic polarization (virtual transitions) and the collective oscillation of the free electron gas within the conduction band (real transition).[58] They are responsible for driving processes such as harmonic generation. Electronic polarization nonlinearities in semiconductors are well covered in various nonlinear textbooks[48,128] and will not be repeated here. On the other hand, slow nonlinearities involve real transitions that have a decay time, typically on the order of hundreds of femtosecond to 1 ns, and lead to processes such as the intensity-dependent refractive index[28,39,46,129–131] and adiabatic frequency shifts.[33,70,93,132] Of the slow response, we describe two components, the interband and intraband driven response. Figure 5(a) presents a flow chart categorizing the above-mentioned nonlinearities.

With reference to the wavelength of the excitation beam (assuming the probe is fixed to the permittivity crossover), Fig. 5(b) highlights the spectral regions where each of these responses occur in a typical ENZ material such as ITO. First, for excitation energies $E > (3–4)\ E_g$ [Fig. 5(b), dark gray region on left side of permittivity vs wavelength graph], slow interband nonlinearities reliant on band-to-band absorption tend to dominate. The change in carriers in turn affects the free-carrier density of the Drude term which leads to index changes in the NIR part of the spectrum. Second, for energies between $2\hbar\omega_p < E < (3/4)E_g$ [Fig. 5(b), medium gray region in middle] lies a transparent low loss region. This region is dominated by fast virtual transitions and leads to electronic polarization nonlinearities such as Kerr index modulation. Third, for excitation energies $E < 2\hbar\omega_p$ [Fig. 5(b), light gray region on right], free-carrier effects term begins to dominate the optical response. In this spectral region, depending on the experimental condition, either a fast or a slow intraband process can dominate. Slow intraband processes that lead to excitation of hot carriers in a non-parabolic conduction band (CB) have been the most widely explored. The fast intraband nonlinear processes are driven by the movement of free electrons around the Fermi level in the non-parabolic CB and tend to benefit from slow light and electric field enhancement that occur around the ENZ spectral region.

A. Physical mechanism of fast free-carrier nonlinearity

While slow free carrier effects are most often discussed in ENZ literature, a fast free-carrier process in Drude ENZ materials exists at all wavelengths and can dominate the response for $\hbar\omega < (3/4)E_g$. Khurgin *et al.*[58] describe this process as the incident energy driving the oscillation of free electrons within a non-parabolic conduction. Under small driving fields, the electrons oscillate predominantly in the parabolic region of the band where the electron velocity grows linearly with momentum—giving rise to a current density $J = -q_k\, v(k,t)$ that is linear. However, under large driving fields, electrons reach the nonlinear regions of the band, where the velocity is no longer proportional to the change in momentum—giving rise to a nonlinear current density [Figs. 6(a) and 6(b)]. In this case, the total current density can be expanded into powers of the electric field E, similarly to the Taylor

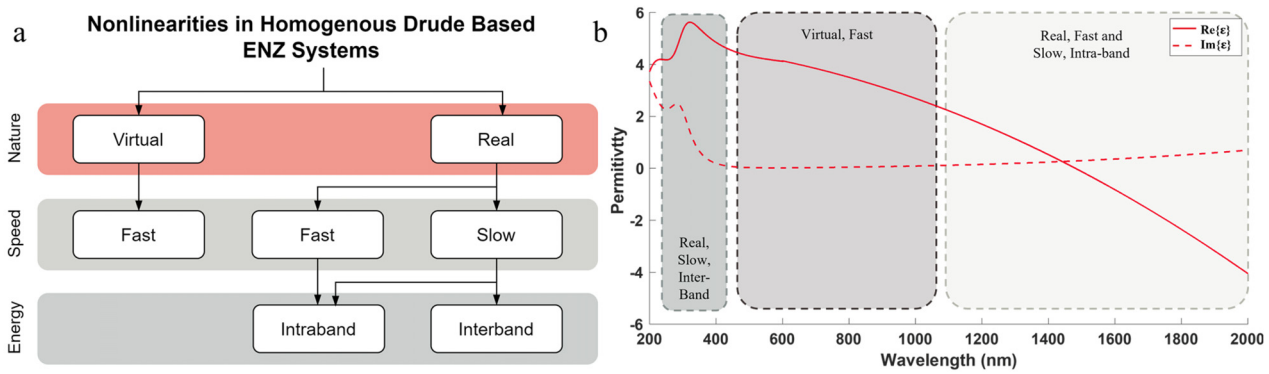

FIG. 5. (a) A flow chart categorizing the different types of nonlinearities commonly observed in a Drude based ENZ system. The first row classifies the nonlinearity on the nature of transition: real or virtual. The next row classifies it based on speed and finally, the third row classifies it based on the energy at which they occur, inter-band [(3/4)E_g] and intra-band [(1/2)E_g], where Eg corresponds to the bandgap of the material. (b) Epsilon-near-zero nonlinearities spectrally distributed, based on type of nonlinearity. Around the bandgap of the material ($\lambda \approx 300$ nm) real, slow inter-band processes occur. In the spectrally transparent region ($\lambda \approx 500$–1100 nm) virtual, fast processes occurs. Finally, in the NIR region ($\lambda > 1100$ nm) real, fast and slow intra-band processes occur.

series expansion for the polarization $P(t) = \chi^1\ \mathcal{E}(t) + \chi^2\ \mathcal{E}^2(t) + \chi^3\ \mathcal{E}^3(t) + \cdots$.

The velocity of the electron is described through the first (α) and second derivative (β) of effective mass in a non-parabolic band as

$$v_z(k,t) = \hbar\left[m_t^{(-1)}\delta k(t) + \frac{1}{2}\alpha\delta k^2(t) + \frac{1}{6}\beta\delta k^3(t)\right], \tag{3}$$

where k is the momentum, and m_t is the transport effective mass. Taking the time average velocity under harmonic excitation, the first- and third-order current densities can be written as

$$\begin{aligned} J^{(1)}(\omega_{1,2}) &= \frac{(iNq^2\langle m_t^{(-1)}\rangle)}{(\omega_{1,2}) + iy}\mathcal{E}_{1,2}\, e^{(-i\omega_{1,2},t)} + c.c., \\ (J^{(3)}(\omega_{1,2}) &= \frac{-iNq^4\langle\beta\rangle}{6\hbar^2}\left(\frac{\mathcal{E}_1 e^{-i\omega_1 t}}{\omega_1 + iy} + \frac{\mathcal{E}_2 e^{-i\omega_2 t}}{\omega_2 + iy} + c.c.\right)^3, \end{aligned} \tag{4}$$

where the second-order term cancels in the case of a symmetric conduction band about the band minimum. This can be connected to a nonlinear susceptibility for a four-wave-mixing process:

$$\chi^3_{fast}(\omega_3 = \omega_1 - \omega_2 + \omega_1) = \chi_{fc}{}^{(1)}(\omega)\frac{e^2 f_\beta}{2\hbar^2 k_0^2(\omega^2 - \gamma^2)}, \tag{5}$$

where $f_\beta\ (k_F) = k_0^2\ \langle\beta\rangle\langle m_t\rangle$. For a typical ENZ material such as ITO, $N_c = 1.1 \times 10^{21}\ \mathrm{cm}^{-3}$, $k_F = 3.2\ \mathrm{nm}^{-1}$, and $k_0 \approx 2\ \mathrm{nm}^{-1}$ (via fitting). This results in $\chi^{(3)}_{fast} = 2.5 \times 10^{-19}\ \mathrm{m}^2\,\mathrm{V}^{-2}$ for an excitation at 1 eV, typical of an ENZ region.

This value of $\chi^{(3)}_{fast}$ is similar in strength to that of the bound electron nonlinearity found in most materials (e.g., Al_2O_3: $\chi^3 \approx 10^{-20}\ \mathrm{m}^2\,\mathrm{V}^{-2}$).[133] Thus, while the process is entirely different, free carrier motion does not give rise to a nonlinearity that is significantly stronger than that of bound electrons. Yet, ENZ provides field enhancement and slow-light effects to increase the magnitude of

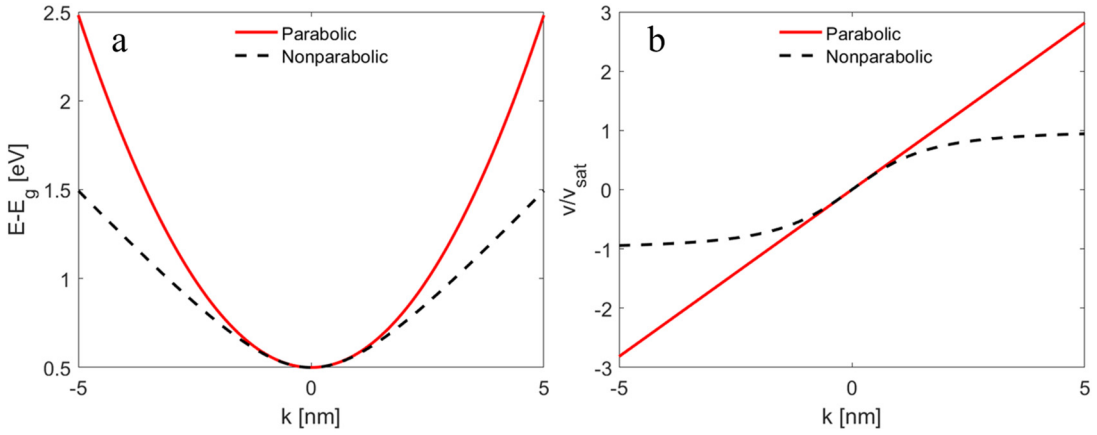

FIG. 6. (a) Parabolic and non-parabolic approximation of the E–k band structure dictating the fast and slow nonlinearity in materials. (b) Carrier velocity in the parabolic and non-parabolic conditions corresponding to the bands in (a).

electric field E and provide longer light–matter interaction time. This combination can lead to a higher effective nonlinearity compared to that observed in conventional crystals without nanostructuring (see Sec. IV B for details). However, the ability to increase the overall conversion efficiency of processes such as harmonic generation and four wave mixing by increasing the interaction length (such as applied to fiber- and $LiNbO_3$-based systems) is ultimately limited by loss in the ENZ regime and the limited transparency bandwidth of ENZ materials. As such, efficiency-sensitive applications would continue to favor low-loss materials, despite the enhancements available via ENZ, while space-constrained applications or scenarios dependent on complex phase matching could benefit from fast nonlinearities in thin ENZ films.

B. Literature on fast free-carrier nonlinearity

Fast nonlinearities in ENZ materials have not been studied as extensively as slow nonlinear effects, neither theoretically nor experimentally. Fast nonlinearities are of increasing interest for frequency-control applications. Fast processes stand to particularly benefit from the near-zero effects such as slow light, electric field enhancement, and relaxed phase matching conditions. Several reports have demonstrated second- or third-harmonic generation using ENZ films.[33,70,93,121,136–139] This has been achieved leveraging surface-symmetry breaking, phonon response, or structuring. In 2015, Capretti *et al.*[93] described the first use of ITO for second harmonic generation, while comparing it to metallic TiN thin films. This sparked interest in fast nonlinearities in ENZ materials, leading to demonstrations of small, yet technically interesting conversion efficiencies of $\eta_{SHG} \approx 10^{-13}$. Consequently, Yang *et al.*[33] demonstrated high harmonic generation, of up to the ninth harmonic, using doped-CdO with the pump positioned at $\lambda_{ENZ} \approx 2100$ nm. Subsequently, Tian *et al.*[134] began with a pump at a higher frequency pump ($\lambda_{ENZ} \approx 1050$ nm), than Yang *et al.*, and demonstrated high harmonics reaching UV wavelengths with high efficiencies of, 10^{-4} and 10^{-6} for fourth and fifth harmonics, respectively [Fig. 7(a)]. Finally, with the use of second and third harmonic generation in ENZ films, Jaffray *et al.*[135] presented a method of ultrafast pulse characterization based on frequency resolved optical gratings (FROG) [Figs. 7(b) and 7(c)]. Such demonstrations move ENZ films closer to the realm of practical niche applications.

C. Physical mechanism of slow free-carrier nonlinearity

For refractive index modulation in degenerately doped semiconductors, real transitions involving free carriers dominate the permittivity tuning effect in the Drude region. The modified Drude equation with bound electron high-frequency contribution is employed to model the free-carrier effects [Eq. (1)]. The tunable parameters within the Drude model are N_c and m^*, which can be altered by optical excitation. Photon absorption can occur both above and below the band edge leading to two separate processes that can modify permittivity. It is important to note that the damping rate Γ can also change in the Drude model with excitation, however because it is often the case for

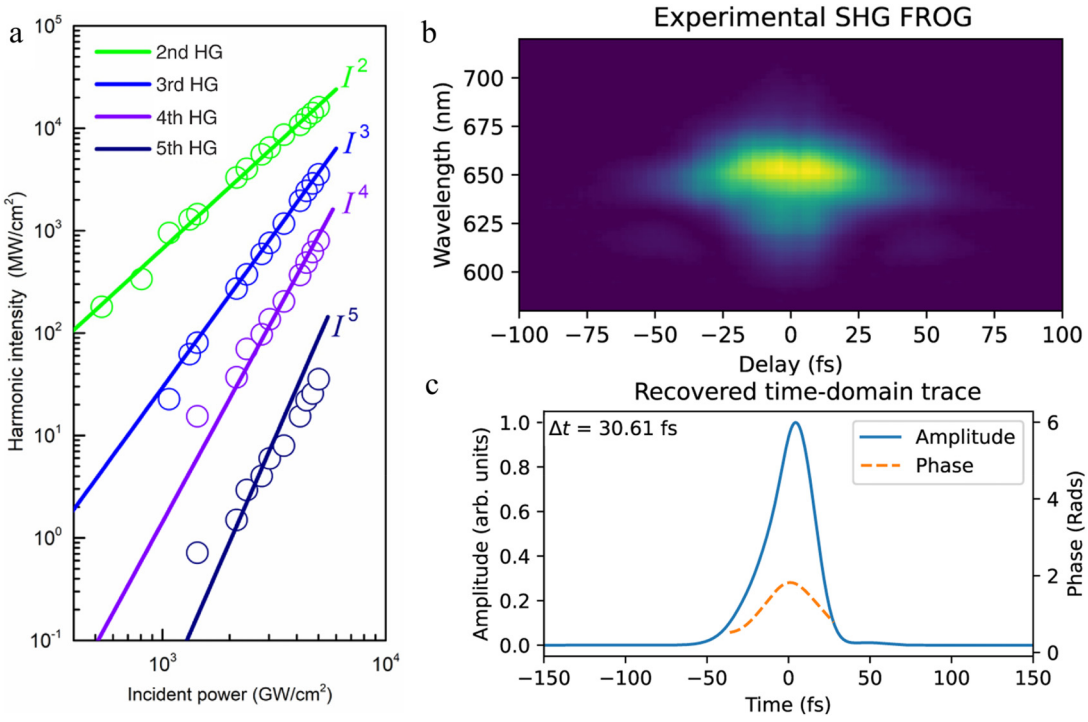

FIG. 7. (a) ITO film (≈ 103 nm thick) illustrating second through-fifth harmonic generation (HG).[134] Reproduced with permission from Tian *et al.*, Photonics Res. **9**(3), 317 (2021). Copyright 2021 Authors, licensed under a Creative Commons Attribution Unported License. (b) Frequency resolved optical grating (FROG) trace from an ITO film showing second harmonic generation (SHG) for pulse characterization.[135] (c) Recovered temporal amplitude and phase profiles. Reproduced with permission from Jaffray *et al.*, Nat. Commun. **13**(1), 3536 (2022). Copyright 2022 Authors, licensed under a Creative Commons Attribution Unported License.

TCOs that $\Gamma \ll \omega_p$, any change of Γ is negligible and the change in permittivity is dominated by N_c and m^*. However, for high loss materials this may not be true, and modifications to Γ may be equally important. These tuning mechanisms are not unique to ENZ materials. As an example, pumping a low doped Si film ($N_c \approx 1 \times 10^{14}\,cm^{-3}$) at energies above the bandgap will lead to index modulation in a similar manner, although the ENZ condition may not be reached. Various modeling efforts by Liberal,[11] de Leon,[42] Sivan,[41] Wang,[140] and Secondo,[40] have successfully matched experimental measurements for both intra- and inter-band measurements of ENZ materials and have been extensively discussed and built upon over the past decade.

1. Intraband absorption

First, for case of doped semiconductors, when the excitation energy is less than the bandgap (typically, $E < 2\hbar\omega_p$) intraband, or free carrier, absorption tends to dominate the optical response.[40] The effect can be modeled directly from the Fermi-Dirac statistics by following carrier and energy conservation. For intraband absorption the number of carriers in the system must remain constant before and after optical excitation

$$\int f(E, \mu(I), T_e(I))\rho(E)dE = N, \tag{6}$$

where $f(E, \mu(I), T_e(I))$ is the Fermi–Dirac distribution, E is the energy of the carrier, μ is the chemical potential, and T_e is the electron temperature, $\rho(E)$ is the density of states, and N is the number of carriers. The second condition is that the change in energy in the system must be equal to the absorbed energy

$$\int (f(E, \mu(I), T_e(I))E\rho(E)dE \int f(E, \mu_0, T_{e0})E\rho(E)dE = \delta Uabs - \frac{AL\tau}{d}, \tag{7}$$

where A is the absorptivity, I is the intensity, τ is the temporal FWHM of the laser, and d is the thickness of the film. In conjunction, the non-parabolic conduction band results in the effective mass being a function of energy $m^*(E)$ (Fig. 8 right side of band diagram).

When an electron absorbs energy, it is promoted to a higher energy state, $E+dE$, where it is no longer in equilibrium with the rest of the electron population. The electron quickly relaxes back to the Fermi level through electron–electron scattering. As a result, the absorbed energy dE is then distributed throughout the sea of electrons raising their overall temperature T_e. The heated electron sea then scatters with lattice phonons (at a rate dictated by the electron–phonon coupling coefficient G), transferring the energy to the lattice and raising its temperature T_l until $T_e = T_l$. The system then relaxes to its initial state through thermal conduction (phonon–phonon scattering), radiation, etc.

The temporal nature of this process is captured by the two-temperature model (TTM).[141] This phenomenological model tracks the electron temperature in the band as it sharply rises with a fs-pulse then decays according to heat transfer between electrons and the lattice

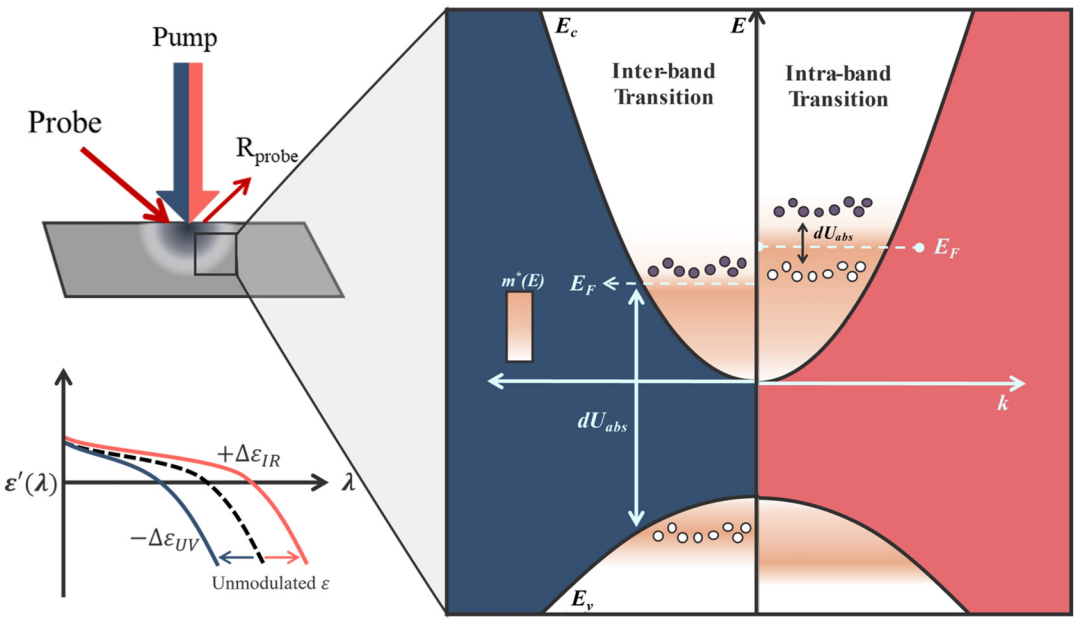

FIG. 8. Figure describes the inter-band (band diagram, left) and intra-band (right) excitation process and the corresponding effects on ε. Inter-band pumping leads to the excitation of electrons from E_v to E_c, resulting in an increase in density of electrons. This results in a blue shift of the plasma frequency, or in other terms, a decrease in the ε at a given wavelength. Figure on the bottom left depicts this effect, where the dashed line corresponds to the unmodulated ε of the thin film, and blue curve corresponds to the modulated ε, after inter-band pumping. On the other hand, intra-band pumping results in excitation of electrons to higher levels of the conduction band, which tend to be characterized by heavier effective masses (color bar, varying from white to peach, corresponds to m^* varying from low to high, respectively). This results in a red shift of the plasma frequency, or an increase in ε at a given wavelength. Purple circles: electrons, White circles: holes, E_F: fermi level, dU_{abs}: pump energy, E_c: conduction band, E_v: valence band, m^*: effective mass, ε: permittivity.

$$C_e(T_e)\frac{\partial T_e}{\partial t} = \frac{\partial}{\partial z}\left(\kappa\frac{\partial T_e}{\partial z}\right) - G(T_e - T_l) + H, \tag{8a}$$

$$C_l(T_l)\frac{\partial T_l}{\partial t} = G(T_e - T_l). \tag{8b}$$

Equations (8a) and (8b) describe the electron and lattice temperatures (T_e and T_l), the volumetric heat capacities of electrons and lattice (C_e and C_l), the thermal conductivity κ, the electron–phonon coupling constant G, and the source term H.[142–144]

Under high intensity, the resulting free-carrier absorption can lead to a significant increase in the electron temperature. This tends to broaden the Fermi–Dirac distribution in energy, increasing the occupation probability of higher energy states. Combining this with the Fermi statistics equations, the average effective mass in the conduction band becomes

$$m^*_{avg} = \left(\frac{1}{N}\int\frac{f(E,\mu,T_e)}{m^*(E)}\rho(E)dE\right)^{-1}. \tag{9}$$

The final piece to the puzzle is the Drude model. Equation (1) shows the plasma frequency ω_p depends on electron effective mass m^*. If m^* is modified by the absorption process, so are the ω_p and relative permittivity $\varepsilon(\omega)$. Given that the effective mass typically increases at higher energies, the occupation of higher energy tends to increase the overall effective mass of the electron sea, resulting in an increase in the permittivity of the material in the ENZ region.

Under the assumption that the effective mass of the carriers is approximately the effective mass at the Fermi level, the effective intensity dependent refractive index (IDRI) coefficient evaluated within the ENZ region at the screened plasma frequency (ω_p) can be described as[40]

$$n_{2,eff}(\omega_p) = \frac{\varepsilon_\infty \alpha_0 n_g \tau}{2n'(\omega_p)NE_F}, \tag{10}$$

where α_0 is the linear absorption coefficient, n_g is the group index, τ is the excitation time, $n'(\omega_p)$ is the real part of the refractive index at the plasma frequency, and E_F is the Fermi energy. For a film with ENZ wavelength $\lambda_{ENZ} = 1550$ nm, $\alpha_0 = 1\times10^5\,\mathrm{m}^{-1}$, $n_g = 6$, $\tau = 100$ fs, $N = 10^{21}\,\mathrm{cm}^{-3}$, and $E_F = 4.5$ eV, the calculated value of the index coefficient is $n_{2,eff} \approx 10^{-16}$ m^2/W, which is an order of magnitude higher than that of semiconductors such as Si or GaAs ($n_2 \approx 10^{-17}$ m^2/W), and four orders of magnitude higher than that of dielectrics such as SiO_2 or Al_2O_3 ($n_2 \approx 10^{-20}$ m^2/W), as shown in Fig. 1(b).

Finally, it is important to note that in most cases the lattice temperature rise of ENZ materials is small (a few degrees K). However, if the material is not given enough time to relax between excitation pulses (commonly nanoseconds to microseconds in metals), the lattice temperature can continue to rise and generate a strong thermal index gradient in the film, or even damage it.[142,145] Thus, ENZ materials cannot be driven fast without corrective action. As such, dissipating thermal energy quickly and lowering the irradiance threshold are important frontiers to being able to push the boundaries of ENZ materials in terms of speed.

2. Interband absorption

If the excitation energy is larger than or equal to the bandgap ($\hbar\omega \geq E_g$) interband absorption occurs. This results in the formation of e–h pairs, modifying the carrier density in the material until the carriers recombine. The density of carriers can be tracked in time according to the two-level rate equation

$$\frac{dN}{dt} = G(t) - \Delta N e^{-t/\tau_n}, \tag{11}$$

where $G(t)$ is the carrier generation rate, τ_n is the characteristic relaxation time of the carriers (typically on the order of picosecond to nanosecond scale, although it can be smaller in the presence of significant defects), and ΔN is the difference in electron density between the excited state and the steady state.[28,146,147]

For interband transitions, the number of free carriers can change as well as the overall energy. In this case, the conservation equations governing energy and number of carriers in the system are given by Secondo *et al.*[148]

$$\int f(E,\mu(I),T_e(I))E\rho(E)dE - \int f(E,\mu_0,T_{e0})E\rho(E)dE = \delta U_{abs} \approx \delta N\left(\mu + \frac{\delta N}{\rho(\mu)}\right), \tag{12a}$$

$$N = N_0 + \delta N = \int_0^\infty f(E,\mu,T_e)\rho(E)dE, \tag{12b}$$

where δN is the produced excess electron density and N_0 is the base electron density. Also, in this case, the density of additional carriers must be related to absorbed energy density of the pump.

Based on Eqs. (1) and (2), an increase in the density of free carriers will lead to an increase in plasma frequency and corresponding decrease in the permittivity of the film in the ENZ region. The effective IDRI coefficient for interband can then be equated to Refs. 40 and 48,

$$n_{2,eff}(\omega_p) = -\frac{q^2\tau\alpha_0}{2\hbar\varepsilon_\infty n'(\omega_p)m^*_{avg}\omega^3}. \tag{13}$$

Finally, it is important to note a few additional effects that can arise under interband excitation. First, when pumping above the Fermi level ($\hbar\omega - E_F > 0.1$ eV), photon generated carriers will initially occupy states above the Fermi energy but will quickly scatter to equilibrate with the rest of the electron sea near the Fermi-level. In this scenario, both the free carrier density and effective mass can be modified since any energy that is larger than the bandgap would translate to an increase in the electron temperature. These processes tend to have opposed effects on the permittivity and therefore should be simultaneously considered by combining the descriptions above. Second, strong interband excitation can also modify the bandgap through renormalization, (due to Coulombic interaction between the charged particles) and the Moss-Burstein shift (due to band filling as carriers populate the lowest available states). These processes tend to spectrally broaden the absorption edge and modify its amplitude. When modeling the permittivity of the doped material via Drude–Lorentz oscillators which include the band edge, these effects alter the properties of the Lorentzian term [equivalent to variation in ε_∞ in Eq. (1)], which in turn affect the permittivity in the ENZ spectral region. While similar effects have been explored for crystalline semiconductors such as Si and GaAs,[150–152] physical models of these processes for common TCO materials such as doped ZnO and doped Sn_2O_3 are currently lacking in the literature and provide an opportunity to significantly improve interband modeling.

D. Literature on real transitions

Numerous studies have demonstrated, TCOs such as doped ZnO, doped In_2O_3 and CdO, exhibit large and rapid intensity dependent index changes.[28,39,95,97,129,153] Building from works of Chang *et al.*[154] on nonlinear effects in oxide nanowires as well as ENZ effects in thin films and plasmonic systems, Kinsey *et al.*[28] studied pumping a highly doped AZO film in the UV to generate free carriers in the conduction band [Figs. 9(a) and 9(b)]. The authors observed the index at crossover to change from $0.5 + 0.25i$ to $0.33 + 0.45i$. Moreover, the recombination time was found to be ≈ 100 fs, which was considerably faster than that typically exhibited by compounds such as Si and LT-GaAs (>10 ps).[155,156] This was attributed to defect states within the bandgap that facilitated recombination,[98,157] like in the case of low-temperature-grown (LT) GaAs.[158,159] Subsequently, a similarly large nonlinearity was observed in ITO by Alam *et al.*[158,159] This involved degenerate pumping of the film in the NIR to generate hot carriers. Since the pump was also positioned in the ENZ region, enhanced absorption was observed which led to a record index change of 0.7 (at off-normal angle of incidence). This was followed by a study by Clerici *et al.*,[129] who utilized both inter-band and intra-band pumps to generate opposing effects on the plasma frequency [Fig. 9(c)]. By appropriately spacing the two pumps in time and space, unique and ultra-fast effects were realized. Some of the more recent works have expanded such studies to Ga-doped ZnO and CdO [Fig. 9(d)].[148,149]

E. Drude-based ENZ in perspective

With an understanding of the nonlinear processes in Drude-based ENZ materials, we can revisit the description of intrinsic and extrinsic effects to place the benefits of ENZ materials in context. Here, we will focus the discussion on the slow intraband nonlinearities that modify the index as they are the most often investigated in the literature.

Figure 10(a) shows examples of the effective intensity dependent refractive index coefficient, $n_{2,eff}$, measured for popular ENZ materials, indexed by the respective conditions of absence, separate presence, or joint presence of the excitation and probe optical beams. Values included here are selected to maintain parameters such as excitation

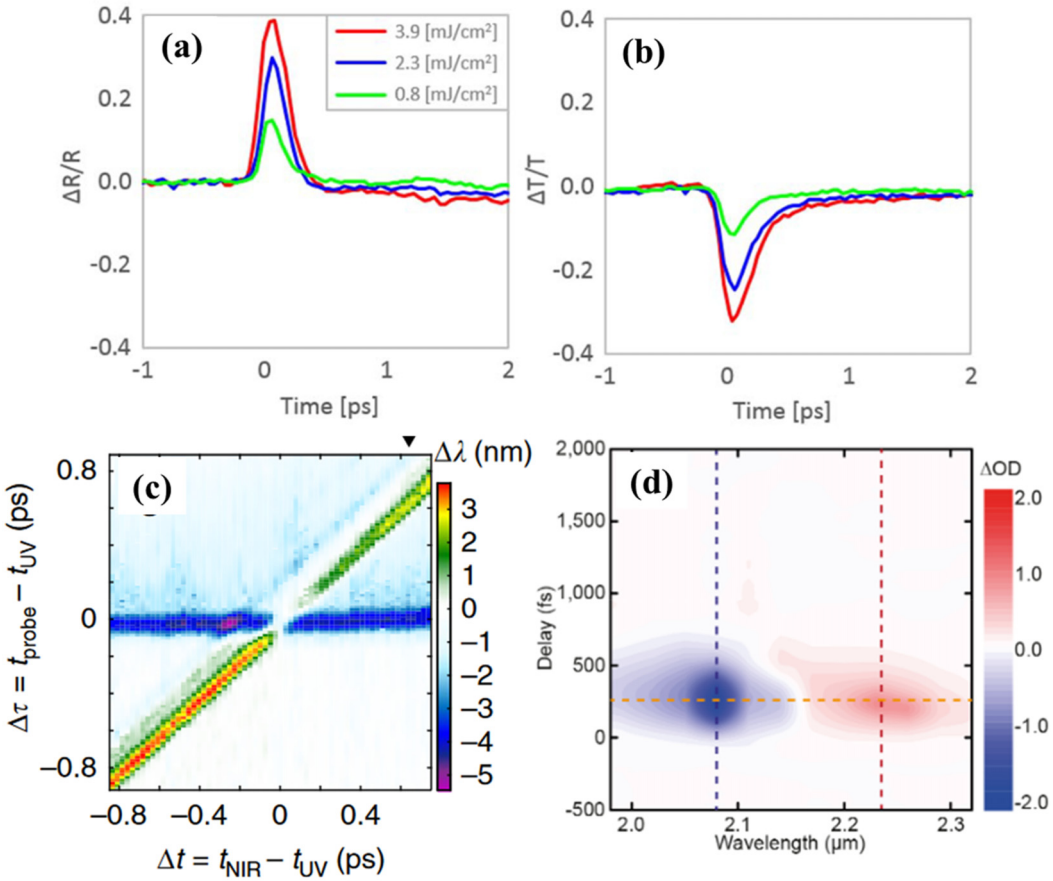

FIG. 9. (a) and (b) Al:ZnO film pumped in the UV showing transient reflection and transmission.[28] Reproduced with permission from Kinsey *et al.*, Optica, **2**(7), 616 (2015). Copyright 2015 Optical Society of America. (c) Two color excitation of an Al:ZnO film showing measured wavelength shifts with varied UV and IR excitation pulses.[129] Reproduced with permission from Clerici *et al.*, Nat. Commun. **8**, 15829 (2017). Copyright 2017 Authors, licensed under a Creative Commons Attribution Unported License. (d) Doped CdO film change in optical density vs probe wavelength and delay time.[149] Reproduced with permission from Yang *et al.*, Nat. Photonics **11**(6), 390–395 (2017). Copyright 2017 Springer Nature Limited.

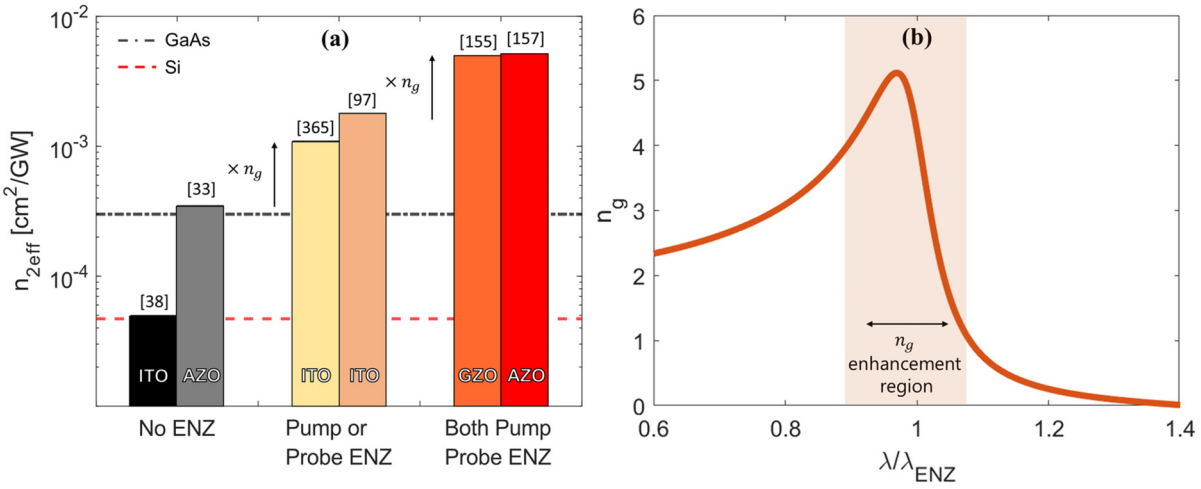

FIG. 10. (a) Effective intensity dependent refractive index coefficient, $n_{2,eff}$, for popular materials showing intrinsic enhancement from group index when pumping and probing at the ENZ condition, compared to that of typical semiconductors Si and GaAs. Values for this plot are denoted in table S1 of the supplementary material section. The labels on the x-axis denote whether the pump and/or probe beams are within the group index enhancement region, expressed as $1 \pm 0.1\,\lambda/\lambda_{ENZ}$. (b) Group index of a typical ENZ material normalized to the ENZ wavelength. A sharp enhancement region is denoted by the shaded region where pumping or probing in this region would yield a 3–5 times enhancement of the nonlinearity as shown in (a).

pulse width, repetition rate, and normal incidence, while allowing variation in other conditions that are key to the comparison, namely, the probe and excitation wavelengths.

Focusing first on the condition where both pump and probe are ENZ-detuned, the measurements illustrate intrinsic free-carrier nonlinearities of TCOs that are comparable in strength to the free-carrier nonlinearities of conventional semiconductors (e.g., Si and GaAs) within the same spectral range. These values are ≈ 3 orders of magnitude larger than those of bound electronic nonlinearities of common reference materials such as SiO_2 or Al_2O_3, but this is expected (see Sec. II) due to the shift from below-gap bound electronic processes (virtual transitions) to above-gap free-carrier processes (real transitions). When one beam is placed near the permittivity crossover of the film, a rise in the average value of the nonlinearity is observed. This can be understood by examining Eq. (10). Here, we note that all terms remain approximately constant with respect to the excitation/probe wavelength except n_g and $n'(\omega_p)$. As a result, we can expect that placing one of the optical beams within the ENZ region would provide an improvement of $n_g(\omega_p)$ (note that at ENZ, $1/n'(\omega_p) \approx n_g(\omega_p)$).[110,148,160] As illustrated in Fig. 10(b), the value of n_g is in the range of 3–5 for the transparent conducting oxides.[18,58] and corresponds quite well to the increase in nonlinearity observed in experiments [Fig. 10(a)]. From the same argument, when the second beam is located near the permittivity crossover of the film, another rise in the nonlinear coefficient is observed that is again proportional to n_g.

As a result, ENZ in TCO materials at normal incidence can be viewed as facilitating two simultaneously occurring features: (1) an intrinsic excitation of stronger free-carrier nonlinearities in the near infrared spectral region as opposed to excitation of weaker below-gap virtual transitions, had the ENZ wavelength not been present in NIR spectrum; (2) an extrinsic slow-light enhancement wherein an enhancement factor of up to n_g^2 is introduced. The result, when compared to Si and GaAs that utilize free-carrier effects in the same spectral window, is an overall improvement in the nonlinearity of one–two orders of magnitude ($n_{2,eff}$ of 10^{-5} to 10^{-3} cm^2 GW^{-1} depending on the exact material and experimental conditions[161]), predominantly due to the added dispersion and slow-light effects achieved by introducing the ENZ condition. In this case, the slow-light effects provide two distinct enhancements: (1) to the absorptivity of the film—which facilitates more efficient use of the excitation intensity, (2) to the spectral sensitivity of index—which maximizes the observed change in index for a given shift of the crossover frequency [see Eq. (10) and Fig. 10(b)]. These effects can be utilized separately or in combination by appropriately defining the operational wavelengths.

It is important to reiterate that while Drude-based ENZ does not radically improve the intrinsic free-carrier nonlinearity of the material, it achieves enhancement through the introduction of slow light effects. This extrinsic effect is bound by the typical trade-off between strength and bandwidth, wherein a steep dispersion (e.g., high n_g) can only be achieved in a limited spectral range. As the ENZ condition in most TCOs is relatively broadband (≈ 200 nm), it therefore provides only a moderate enhancement ($n_g \propto \partial n/\partial\omega$) to the nonlinearity of the film, as shown in Fig. 10(b). As a result, large irradiance values (>10 GW cm^{-2}) are still required to achieve the strong index modulations on the scale of $\Delta n \approx 0.1$–1 reported in the literature.[47,97,154,162–165] Although the broad enhancement is beneficial, unfortunately it necessitates the introduction of loss within the film via the introduction of a high density of free carriers. While this impacts the efficiency for transmissive applications, the loss in most popular TCOs remains sufficiently low ($\mathrm{Im}\{n\} \approx 0.1$–0.5 at crossover)[18] such that sub-micron films can achieve transmissivity values of 80% and higher. More critically, under extreme irradiances or high-repetition rates, the energy absorbed through free-carrier processes leads to a collective increase in the lattice temperature of the material. This can produce a slow (1 μs to 1 ms scale) and strong thermal index effect that limits the potential speed of operation and can lead to material degradation.[166–169]

Thus, while the nonlinearity in Drude ENZ relaxes on the scale of picosecond, operating films at a high-repetition rate requires the mitigation of the thermal energy buildup either through the reduction in the required irradiance or through thermal engineering; this remains an open area of study.

Despite these limitations, Drude-based ENZ materials offer several key benefits. Primarily, ENZ materials offer the ability to simultaneously employ intrinsic and extrinsic enhancements over a broad spectral range naturally, without requiring nanofabrication. Moreover, the materials employed are well-developed, can be readily tuned during deposition to meet specific requirements, and can be integrated with various device platforms.[68,98,116,170–176] Additionally, the TCOs have been shown to exhibit quite impressive damage thresholds in excess of 1 TW cm^{-2} for thin films.[32,134] Thus, while the nonlinearity may not be significantly enhanced, the damage threshold is so high that ENZ materials unlock the potential of extreme refractive index changes on the scale of unity that are not possible with typical semiconductors or metals.

F. Boosting ENZ nonlinearity via extrinsic enhancement

To reduce the irradiance required to achieve a desired nonlinear response, such as strong index shift or frequency conversion, boosting the extrinsic enhancement of ENZ films has been pursued. As noted in Sec. II, these techniques seek to employ structure or specific excitation schemes to improve confinement, generate strong dispersion in reflection, transmission, and absorption, interaction length, or interaction time, providing a multiplier for the intrinsic nonlinearity of the constituent materials. For homogeneous ENZ films, both the fast and slow nonlinearity can benefit from these effects. Researchers have explored the prospect of coupling metasurfaces to ENZ films,[43,44,70,75,177,178] by utilizing highly confined modes such as the ENZ or Berreman mode,[65,66,69,149,179,180] or by placing ENZ structures inside cavities.[106,181–183] Ultimately, by adding structure to a bulk film one can modify the material dispersion and light confinement with additional resonances or anisotropy.

One of the early approaches to achieving this was by tuning highly confined modes in thin homogeneous films such as the ENZ and Berreman modes.[65,66,187] These modes, often excited by tuning the incident angle, or by providing the necessary momentum using gratings, lead to a sharp and strong absorption resonance that can effectively modulate properties like transmission and reflection. As shown in Fig. 11, both modes are characterized by flat dispersion and low group velocity, resulting in slow light and enhanced absorption within the thin films. While both these modes exhibit similar effects, they often require different coupling conditions. Since the ENZ mode is a high-momentum, non-radiative mode, prism/grating couplers are needed to provide the momentum necessary for mode excitation. On the other hand, the Berreman mode lies to the left of the light line, is radiative in nature and can be excited from free space. Additionally, Berreman modes have been heavily focused in ENZ materials for showing enhanced nonlinearities at higher angles of incidence.[65,66,121] Perfect absorption can indeed be achieved by these films,[179] which requires specific properties and geometric constraints, leading to improved nonlinear index tunability.

To broaden the design space to improve nonlinearities, researchers also considered utilizing nanoantenna structures coupled to homogeneous ENZ layers. For example, frequency conversion was achieved

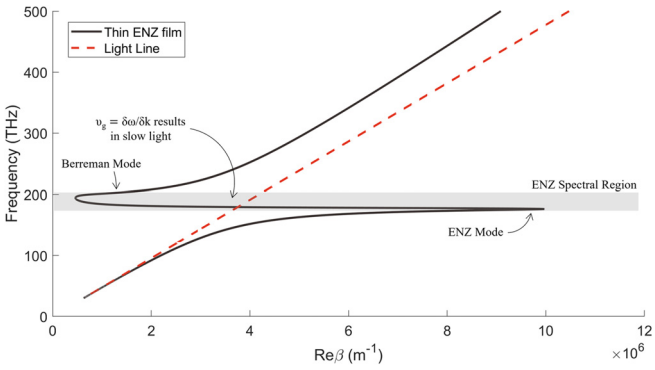

FIG. 11. ω–k dispersion curve for a 20 nm thick AZO film (representative ENZ material). The curve is highly dispersive in the vicinity of the ENZ spectral region. As a result, group velocity dω/dk tends to 0. Depending on the position of the mode in the momentum space, either a Berreman mode or and ENZ mode can be excited. While both these modes result in slow light, only the Berreman mode can be coupled to from free space. The ENZ mode on the other hand requires gratings or prisms to impart the additional momentum required for excitation.

using a structured medium consisting of titanium nitride (TiN) split ring resonator arrays [Fig. 12(a)]. The TiN nanoantennas exhibited a double resonance effect in which the SHG was enhanced due to the simultaneous presence of a plasmonic resonance at the excitation frequency, and an ENZ resonance at the second harmonic frequency.[184] Counteracting the enhancement from the dual resonance, was the relatively large optical losses of TiN. Since TCOs are known to exhibit lower losses than metals at their crossover wavelength, J. Deng *et al.*[70] utilized gold nanoantenna coupled to a 15 nm thick ITO film. They demonstrated a 10^4 fold enhancement of SHG by coupling into the ENZ mode. More information on harmonic enhancement observed in ENZ media can be found in the report by Solis *et al.*[188]

For refractive index modulation, efforts have primarily involved the use of ITO and gold.[44,125,185,189] Alam *et al.*[44] reported a gold dipole antenna array on top of a 23 nm thick ITO layer [Fig. 12(b)]. The nanoantennas were designed such that their resonance overlapped with the ENZ point of the ITO film at 1420 nm, providing a 50 fold enhancement of peak intensity. Additionally, Wang *et al.*[185] showed that anisotropy can be modified in these materials with Au nanoantennas on an ENZ layer [Fig. 12(c)]. The temporal response displayed a change in polarization of a probe beam due to pump absorption aided by the nanoantennas. Yu *et al.*[186] showed enhanced terahertz (THz) conversion efficiency when using ITO split ring resonance [Fig. 12(d)]. Finally, researchers also considered embedding these films within cavities, such as in the work by Hu *et al.*[181] To improve the Q-factor of the broad ENZ resonance, a Dy:CdO film was embedded in a Brag microcavity [Fig. 12(e)]. While the study achieved a large ΔR of 94% at 7 μJ/cm^2 of pump fluence, it came at the cost of a greatly reduced bandwidth (<10 nm). Other, more exotic approaches to enhancing ENZ nonlinearity have consisted of exciting whispering gallery modes in dielectric nanospheres coated with ITO,[190] or achieving momentum matching between light and thin-film ENZ modes using a prism.[97]

When fixing key output quantities, such as change in reflection/transmission or conversion efficiency, adding extrinsic enhancement via structure to a homogeneous ENZ film enabled researchers to reduce the required irradiance. This lessens the impact of the

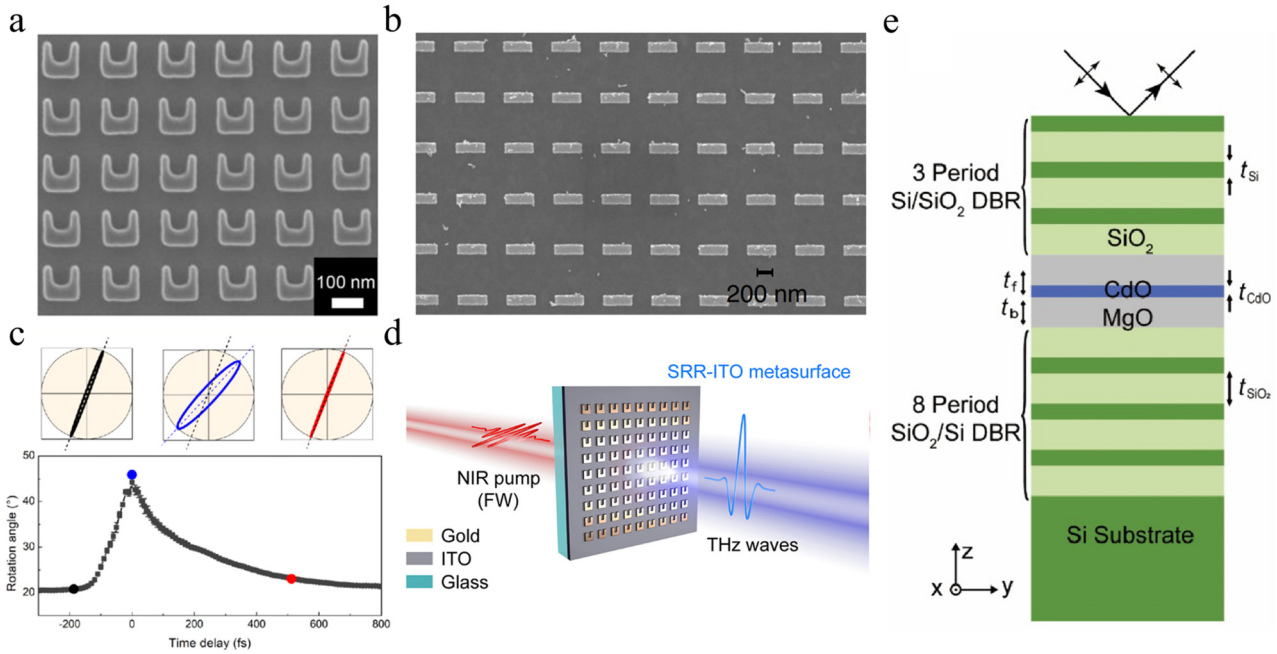

FIG. 12. (a) SEM image of TiN split-ring resonators (SRR) on a sapphire substrate. To enhance SHG, this structure combines a plasmonic resonance at the pump frequency and ENZ resonance of TiN at the SHG frequency.[184] Reproduced with permission from Wen *et al.*, ACS Photonics **5**(6), 2087–2093 (2018). Copyright 2018 American Chemical Society. (b) SEM image of 27 nm thick gold dipole nanoantenna, on a 23 nm thick ITO coated glass substrate. The ENZ resonance coincides with the plasmonic resonance of the gold nanoantenna, leading to strong coupling. As a result of modified dispersion and improved coupling of free space light, values for $n_{2,\text{eff}}$ as high as $\approx 3.5\,\text{cm}^2/\text{GW}$ are reported.[44] Reproduced with permission from Alam *et al.*, Nat. Photonics **12**(2), 79–83 (2018). Copyright 2018 Authors, licensed under a Creative Commons Attribution Unported License. (c) Graph showing the rotated angle of the polarization azimuth as a function of irradiated fluence. The structure consists of rectangular gold nanoantenna on a 310 nm thick ITO film. Due to the anisotropic response of the system, p-polarized light is selectively transmitted with a phase delay based on the pump fluence, whereas s-polarized light is transmitted irrespective of pump fluence.[185] Reproduced with permission from Wang *et al.*, ACS Photonics **8**(9), 2791–2799 (2021). Copyright 2021 American Chemical Society. (d) Schematic of an ultra-fast THz wave generator. The device consists of gold SRRs coupled to a ≈ 20 nm thick ITO film on a glass substrate. Upon resonant pumping with NIR femtosecond laser pulses. this metasurface yields a peak THz intensity that is enhanced by a factor of $\approx 1 \times 10^4$ times compared to that of a similar metasurface for which the ITO film is absent.[186] Reproduced with permission from Lu *et al.*, Nano Lett. **21**(18), 7699–7707 (2021). Copyright 2021 American Chemical Society. (e) Schematic of a high-Q perfect absorber based on a simulated doped CdO film coupled to a Bragg microcavity. The dimensions are: $t_{\text{Si}} = 291$ nm, $t_{\text{SiO2}} = 714$, $t_{\text{CdO}} = 10$ nm, and $t_f = t_b = 586$ nm. While the high Q resonance theoretically yields a large ΔR (94%), the bandwidth is limited to ≈ 10 nm.[181] Reproduced with permission from Hu *et al.*, Opt. Exp. **27**(19), 26405 (2019). Copyright 2019 Optical Society of America.

drawbacks of homogeneous ENZ materials, namely, optical loss and subsequent thermal dissipation, while providing a larger design space through which to optimize the response. The drawback of these approaches comes in the form of a limited bandwidth (e.g., introduction of resonance) and fabrication complexity, and thus typically must be tailored to a specific application or operation condition.

V. STRUCTURED ENZ MEDIA

In addition to homogeneous materials, vanishing permittivity can also be achieved by engineering an effective medium based on structural dispersion where the composite medium exhibits ENZ response as a whole, rather than exhibiting an ENZ condition for each individual constituent material.[160] These intrinsically structured systems provide access to new spectral regions and more freedom in design to meet specific application conditions when compared to homogeneous materials. An important difference between structured and natural homogeneous systems, in the context of ENZ interactions, is that structured materials exhibit their optical effects as an average across several unit cells, while naturally occurring materials do so at the nanoscale. Thus, optical interactions in structured ENZ may differ greatly between the wavelength and sub-wavelength scales.

Perhaps one of the most straightforward methods to achieve an effective ENZ condition is through the formation of alternating layers of metal and dielectrics. The resulting permittivity is derived from effective medium theory (EMT) according to Ref. 4

$$\varepsilon_\perp = \frac{\varepsilon_m d_m + \varepsilon_d d_d}{d_m + d_d} \quad \text{and} \quad \frac{1}{\varepsilon_\parallel} = \frac{\frac{d_m}{\varepsilon_m} + \frac{d_d}{\varepsilon_d}}{d_m + d_d}, \tag{14}$$

where $\varepsilon_\perp$ and $\varepsilon_\parallel$ are the effective permittivity components perpendicular and parallel to the plane, and d_m (d_d) and ε_m (ε_d) are the thickness and dielectric constant of the metallic (dielectric) layer, respectively. A judicious mixture of materials with opposite signs of permittivity (i.e., positive dielectric and negative metallic materials) and subwavelength thicknesses will act effectively as an ENZ medium while offering flexibility in the design process to tune the ENZ crossover across the spectrum. Implementations in various forms such as lamellar sheets, rods and inclusions,[14,192–194] have been shown to generate exceptionally

strong anisotropy in the permittivity by achieving ENZ only along certain axes, even achieving the hyperbolic dispersion [Fig. 13(a)]—in other words a hyperbolic metamaterial (HMM).[85] Note that, due to the large mismatch between the dielectric and metallic permittivity, very thin uniform layers of metal are often needed—which can be challenging to realize, especially in the case of noble metals.[195] Yet, the epitaxial growth of ultrathin (≈5 nm) ultra smooth layers has been reported as a viable approach to reduce loss and achieve better optical performance.[196]

Another approach to achieve an effective zero permittivity it to utilize Dirac-like cone dispersion-based metamaterials. These Dirac cone zero index metamaterials (DCZIM) are often all dielectric in nature.[191,197] They are formed by the accidental threefold degeneracy of two linear bands (conical dispersion) and a quadratically dispersive band, occurring at the center of the Brillouin zone. Because of this degeneracy, the group velocity of the two linear bands changes signs, implying that the effective index crosses 0. Furthermore, the effective permittivity and permeability also cross zero [Fig. 13(b)], which can be shown via rigorous effective medium homogenization approaches. Accordingly. these metamaterials are also referred to as epsilon-mu-near-zero (EMNZ). As an example of a DCZIM, Li *et al.* demonstrated a square lattice of Si nanopillars embedded in a SU-8 (see disclaimer section) matrix.[191] The presence of spatially and spectrally degenerate electric monopole, transverse magnetic dipole, and longitudinal magnetic dipole resulted in Dirac-like cone photonic band structure [Fig. 13(b), inset]. While the zero effective ε and μ aids in impedance matching, these structures do not exhibit slow light enhancement, critical to optical nonlinearities. Due to the linear dispersion, DCZIMs are characterized with a finite group velocity at the frequency where effective ε and μ properties vanish.[56] As a result, DCZIMs have largely been used in the demonstration and manipulation of linear optical effects as their lack of slow light largely precludes enhancement to nonlinear processes.[191,197]

Yet another approach is to take advantage of dispersion engineering with the help of a composite metal-dielectric waveguide. For example, consider a rectangular metallic waveguide.[198] For the waveguide supporting the fundamental transverse electric TE_{10} mode, the propagation constant is expressed as

$$\beta = \sqrt{(2\pi n f/c)^2 - (\pi/w)^2}, \tag{15}$$

where w is the width for the corresponding magnetic field, n is relative refractive index of the plasma, c is the speed of light in vacuum, and f is the operating frequency. The relative effective index for the TE_{10} guided mode can be expressed as[199]

$$\varepsilon_{eff}/\varepsilon_0 = n^2 - c^2/(4f^2w^2). \tag{16}$$

As implied by Eqs. (15) and (16), when the waveguide is operated at the cutoff frequency of its TE_{10} mode (i.e., $\beta = 0$, indicating an infinite phase velocity), the waveguide appears as an effective medium having effective zero permittivity [Fig. 13(c)].[198,199] In the optical regime, a nanoscale plasmonic waveguide with hollow dielectric core surrounded by metallic cladding could mimic an ENZ medium when operated at the cut off frequency of its fundamental TE_{10} mode. The propagation constant for the resulting mode becomes zero. Such structures are quite challenging to realize and thus far have not been extensively explored for their nonlinear properties, although energy squeezing and tunneling of electromagnetic waves have been experimentally realized.[199,200]

A. Nonlinearities in structured ENZ media

Among the techniques mentioned above, achieving an effective ENZ condition using metal-dielectric composites has been the most widely used technique to modify nonlinear optical interactions. Such metamaterials have been successful in extending the ENZ and NZI condition into the visible spectral range (500–1000 nm)[200,201] where existing homogeneous ENZ materials are too lossy to exhibit NZI and the strong index dispersion needed for slow-light enhancement (see the review by Kinsey *et al.*[18]).

Rashed *et al.*[194] reported a multilayer metamaterial sample composed of 4 alternating layers of 16 nm of Au and 32 nm of TiO_2, resulting in a 605 nm ENZ wavelength, along with 30% and 10% modulation of the transmitted ($\Delta T/T_{lin}$) and reflected ($\Delta R/R_{lin}$) probe signals, respectively. The total increase in $\Delta\varepsilon_{eff,real} \approx 0.16$ (420% change) and the temporal nonlinear dynamics related to the relaxation of hot electrons was investigated by a two-temperature model (2TM).

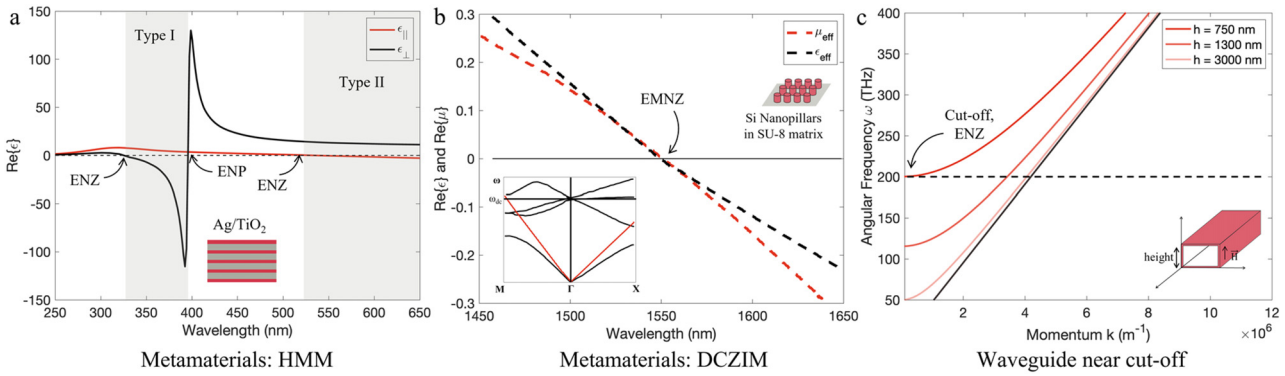

FIG. 13. (a) Anisotropic optical response of Ag/TiO_2 stack metamaterial calculated using effective medium theory, with a 35% fill ratio of Ag. (b) Degenerate electric monopole, longitudinal magnetic dipole and transverse magnetic dipole induce a Dirac-like material response resulting in effective permittivity and permeability crosses zero at the degeneracy point between the 3 resonances. Adopted from Ref. 191. (c) Waveguide near cutoff, achieving ENZ condition.

To further confirm the enhancement of the nonlinear optical response in ENZ metamaterials, Suresh *et al.*[201] fabricated a sample consisting of five bilayers of Ag and SiO_2 (with respective thicknesses of 16 and 65 nm) that resulted in an ENZ wavelength of 509 nm [Fig. 14(a)]. The experimental results showed the advantages of an ENZ metamaterial over a bulk metallic thin film, achieving an effective nonlinearity of $n_{2,eff} = (1.2 \pm 0.1) \times 10^{-12}$ $m^2 W^{-1}$ and lower loss $\beta_{eff} = (-1.5 \pm 0.2) \times 10^{-5}$ $m W^{-1}$. Subsequently, Genchi *et al.*[202] demonstrated that the nonlinear optical parameters of Au/Al_2O_3 ENZ multilayer metamaterials could be continuously modulated in a broad range of the visible spectrum at different incidence angles with transverse electric (TE) or transverse magnetic (TM) polarized light.

In addition to stacked metal-dielectric layers, embedding metallic pillars into a positive permittivity dielectric can also result in an ENZ condition. Neira *et al.*[203] electrodeposited Au into nanoporous AAO (anodized aluminum oxide) templates on a glass substrate to achieve a plasmonic nanorod metamaterial sample with the ENZ wavelength around 600 nm. The nanorod metamaterial geometry provided more than two orders of magnitude larger intensity dependent index nonlinearity than the interband nonlinearity of the plasmonic metal itself at any designed wavelength. Next, Kolmychek *et al.*[136,204] demonstrated an order of magnitude enhancement of second-harmonic generation (SHG) for p-polarized fundamental wavelength of 820 nm at the angle of incidence of 15°[136] and self-focusing/defocusing[204] [Fig. 14(c)] effects in ordered arrays of Au nanorods in porous aluminum oxide. The observed phenomena were tightly associated within the spectral vicinity of the ENZ wavelength where the transition occurred from the elliptic to hyperbolic dispersion and the maximum $|n_{2,eff}|$ and $|\beta_{eff}|$ were, respectively, 4×10^{-13} m^2 W^{-1} and 10^{-6} m W^{-1}, for an incidence angle of 30°.

Although the prevailing ENZ metamaterials are polarization dependent, they can also be designed to be polarization insensitive. A free-standing metal-dielectric fishnet nanostructure that had polarization- insensitive NZI properties was demonstrated by Yun *et al.*[205] By optimizing the metal-dielectric fishnet structure to simultaneously balance the electric and magnetic responses, both the effect permittivity and permeability were close to zero at 1.55 μm, leading to produce a zero index and matched impedance to free space. It should be noted that these structures do not always possess slow light effects which are crucial for enhanced nonlinearities, due to a lack of rapid dispersion.

Furthermore, a metal-insulator-metal (MIM) cavity with engineered effective permittivity exhibited multiple ENZ points and could simultaneously increase absorption and the Purcell factor at the excitation and emission wavelengths, respectively.[183] These structures can be readily designed to exhibit ENZ wavelengths which are responsive to both TE- and TM-polarized excitation. Additionally, their spectral positions can be adjusted by controlling the refractive index and thickness of the embedded dielectric. On this basis, Kuttruff *et al.*[206] demonstrated an all-optical, ≈3 ps switching of the reflectance of a MIM nanocavity approaching a relative modulation depth of 120% in the VIS-NIR spectral range.

In addition to the metal-dielectric stack structure, all-dielectric metamaterials can also enhance the nonlinearity while opening a route to tailor the loss. Although not ENZ in the passive state, negative permittivity and free-carrier losses can be optically induced, allowing a route to control the impact of loss while using structure to further enhance the nonlinearity. However, the corresponding ENZ wavelength is generally located in the IR range. Kelly and Kuznetsova[207] numerically studied the pump-probe ultrashort pulse modulation in the AZO/ZnO metamaterial whose ENZ wavelength was 1778 nm. While the structure was dielectric in the passive state, UV pumping the metamaterial introduced free carriers and resulted in an ENZ condition at shorter wavelengths. At the permittivity crossover, the amplitude and FWHM duration of the pump pulse were the main factors affecting ultrashort probe pulse propagation. The short pump pulse (100 fs) with the highest investigated pump pulse amplitude (restricted by the damage threshold) caused a rapid and significant change in optical permittivity, leading to a highly asymmetric shape of the output probe pulse. Additionally, Xie *et al.*[208] theoretically investigated the ultrafast dynamic switching of optical response using tunable hyperbolic metamaterial (HMM) that consisted of 5 pairs of alternating layers of ITO and SiO_2 [Fig. 14(b)]. The proposed HMM platform showed the largest intensity dependent index nonlinearity ($n_{2,eff} \approx 5.87 \times 10^{-16}$ $m^2 W^{-1}$ and $\beta_{eff} \approx -1.27 \times 10^{-9}$ mW^{-1}) at an ENZ wavelength of 1454 nm, higher than that of the bulk ITO.

Beyond ENZ metamaterials, the ENZ and NZI condition can also be realized using the structural dispersions of waveguides. With this approach, a nonlinear plasmonic waveguide with effective ENZ condition was designed by Li and Argyropoulos[207] to achieve efficient tunable nonlinear coherent perfect absorption response at the nanoscale. In this case, the local electric field at the ENZ coherent perfect absorption (CPA) point was intense (≈ 35 times stronger) and uniform. This led to the prediction that nonlinearities such as the intensity dependent index could be improved and ultimately triggered by reduced input intensities.[210] Also, as shown in Fig. 14(d), Gosciniak *et al.*[209] proposed a bistable resonator-free all-optical device based on ENZ ITO material in a slot waveguide. A bistable nonlinear activation function, developed based on this configuration, showed a prediction accuracy of 98% for MNIST (Modified National Institute of Standards and Technology), 89% for Fashion MNIST, and ≈52% for CIFAR-10 (Canadian Institute for Advanced Research) datasets.

To conclude this section, the formation of an effective ENZ condition via structured systems is a collective property and is of course dependent upon the constituent materials and their structure. This can be designed to provide extrinsic enhancements via slow light effects and confinement, like in the case of homogeneous ENZ materials. Yet, the intrinsic nonlinearities, and their subsequent process (e.g., virtual/real), strength, and relaxation characteristics, are founded in the properties of the constituent materials used to form the structure. The effective nonlinearity can thus be viewed as a combination of nonlinear processes occurring within the constituent materials ($\chi^{(3)}_{o(1,2)}$), weighted by the ratio of the electric field overlap with, and multiplied by an extrinsic enhancement due to the structural response $[\Delta\varepsilon_{eff} \approx EF(\chi^{(3)}_{o,1}|\mathcal{E}_1|^2 + \chi^{(3)}_{o,2}|\mathcal{E}_2|^2)]$. As an example, a lamellar composite of Ag and SiO_2 can be engineered to form an effective ENZ condition in the visible spectral range, despite neither constituent material being ENZ. The nonlinear processes ($\chi^{(3)}_o$) will be equivalent to the nonlinear processes in the bulk versions of the constituent materials at the same excitation wavelength, a free-carrier Fermi-smearing nonlinearity for Ag and a virtual nonlinearity for SiO_2. Upon excitation, an incident field will then be distributed within the material, leading to absorption within Ag (which drives the free-carrier Fermi-smearing nonlinearity), and propagation within SiO_2 (which drives a virtual Kerr process). The distribution of this field can be altered by the

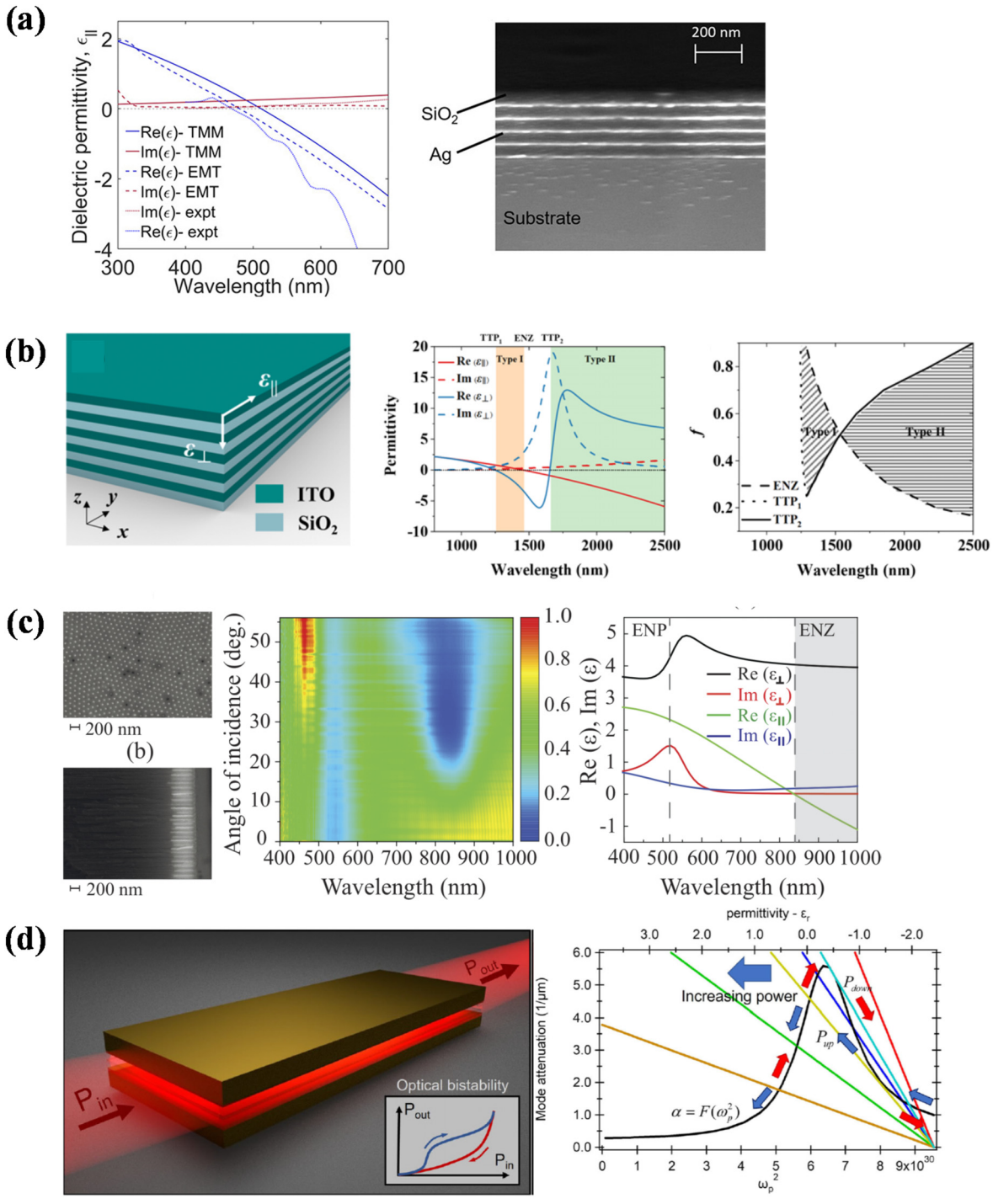

FIG. 14. (a) Effective parallel permittivity and cross-sectional image of the fabricated Ag-SiO_2 multilayer stack.[201] Reproduced with permission from Suresh *et al.*, ACS Photonics **8**(1), 125–129 (2021). Copyright 2021 American Chemical Society. (b) Sketch of ITO/SiO_2 multilayer, the permittivity and the optical phase diagram.[208] Reproduced with permission from Xie *et al.*, Opt. Express **30**(12) 21634–21648 (2022). Copyright 2022 Optical Society of America. **(c)** Cross view images of the HMM sample, the angular-wavelength transmission spectrum and the spectra of the calculated effective permittivity tensor components.[204] Reproduced with permission from Kolmychek *et al.*, Opt. Lett. **47**(22), 6009 (2022). Copyright 2022, Optical Society of America. (d) The proposed bistable all-optical device based on an ENZ ITO waveguide and corresponding simulated bistable switching as a function of optical power.[209] Reproduced with permission from Gosciniak *et al.*, Laser Photonics Rev. **17**(4), 2200723 (2023). Copyright 2023 Authors, licensed under a Creative Commons Attribution Unported License.

structure or excitation condition, enabling coupling to confined plasmonic modes on thin silver films, while also facilitating an overall slow light effect due to the effective material dispersion. Relaxation of the system would then be driven by thermal relaxation within the Ag films while the Kerr process is instantaneous. Although this discussion is somewhat obvious, we find it a useful picture. Only observing the material in the homogenized view blurs the physical insight into the nonlinearities at play and preludes key points through which the response may be tailored. For example, utilizing materials with higher intrinsic nonlinearities would of course be beneficial, while engineering field confinement can be used to focus light onto lower loss materials or higher nonlinearity materials, while still utilizing an overarching slow light effect provided through an effective ENZ condition. Unlike homogeneous materials, structured approaches provide significant flexibility to engineer these conditions through an expanded material pallet as well as geometric design that can be particularly powerful at improving the strength of the nonlinearity within the constraints of the intrinsic and extrinsic effects being employed. However, this comes at the cost of increased fabrication complexity and excitation conditions. This trade-off should be weight based on the intended application.[183] More information on nonlinearities in structured materials, can be found in Refs. 201 and 211–216.

VI. OPPORTUNITIES FOR ENZ NONLINEARITIES

With an understanding of the origins of nonlinearities in ENZ materials as well as how they can be tailored by various techniques, we can now turn our attention to a consideration of the opportunities that ENZ materials provide. This section will focus on two aspects: (1) the potential to explore new materials and balance performance tradeoffs and (2) the potential use of the large and fast index contrast to study space-time optical effects.

A. Alternative ENZ materials—beyond doped indium and zinc oxides

As seen from Table S1, and recent demonstrations, most of the studies on homogeneous ENZ nonlinearities have been limited to three materials, doped In_2O_3, ZnO, and CdO.[80,98,102,148,149,217,218] This is largely because degenerately doped ITO is readily commercially available[219] and high solubility of Al in ZnO[220] leads to straightforward sputtering[221,222] and pulsed laser deposition processes.[223,224]

While these films have led to demonstrations of exceptionally large and ultrafast intensity-dependent index nonlinearities at ENZ frequencies, the high optical pump power requirements have posed a significant challenge to practicality. This naturally leads to the question—are there materials better suited to exhibit larger or more efficient nonlinearities around the technologically relevant wavelengths?

Considering that TCOs have been researched for several decades[225–227] and tailored for specific applications such as flat panel displays,[228] solar cells[229,230] and LEDs,[231] it would be short sighted to dismiss the possibility of materials better suited for ENZ nonlinearities.[18] This section of the review is aimed leveraging the understanding of nonlinearities in ENZ materials to highlight other material systems that could potentially serve as an alternative to (and perhaps even outperform) the conventional TCOs. It begins by highlighting the ideal characteristics of a material with a crossover in the NIR, followed by introducing material systems.

1. Ideal characteristics

In the case of Drude materials, a zero crossing of the permittivity occurs when, physically, the contribution of free electron resonance becomes strong enough to counter high frequency resonance(s) (bound electrons, interband absorption, excitonic absorptions). Mathematically, this occurs when the ε_∞ term equals in magnitude the Drude term. From Eq. (1), it is evident that the ratio of N_c/m^* and ε_∞ are key to achieving the zero crossing at technologically relevant wavelengths. This implies that materials with a low ε_∞, high N_c and low m^* are well suited to exhibit ENZ and NZI properties in the NIR. Out of these, ε_∞ and m^* are material specific and can be tuned by changing the composition of ternary or quaternary compounds making the process intricate. Free carriers (N_c) on the other hand can be readily tuned, up to the dopant's solubility limit in the host matrix. Since tuning free carriers is generally easy, we can consider how many carriers are needed for a given ε_∞ and m^* to generate a permittivity crossover at a desired wavelength. Figure 15 highlights the range of ε_∞ and m^* (indicated by points within the colored band) that gives rise to a permittivity crossover between 1400 and 1600 nm for various free carrier densities (indicated by the colored bands) at a mobility of 40 $cm^2/(V\,s)$. While ε_∞ and m^* both affect the crossover wavelength, it is evident from Fig. 15 that m^* has a larger effect (especially in the range of low m^* materials which are important for NIR applications) and should be critically considered when exploring alternative materials.

In addition to these parameters, other parameters such as the bandgap, conduction band non-parabolicity and mobility also have an influence, especially on the nonlinear performance. For example, in the case of intraband nonlinearities, a high CB non-parabolicity

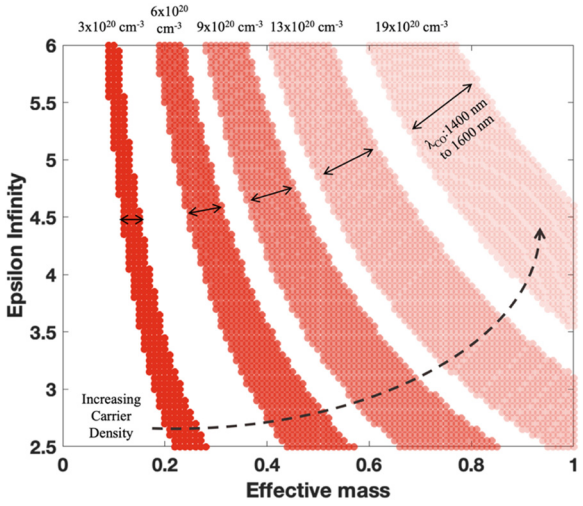

FIG. 15. Based on the Drude model, this graph displays a range of crossover wavelengths between 1400 and 1600 nm (shown by the red band), as a function of high frequency permittivity ε_∞, electron effective mass m^* and free carrier density N_c (indicated by the shade of red, where lighter shades indicate higher free carrier densities). Mobility is fixed at a commonly found value for materials of 40 $cm^2/(V\,s)$. In the case of low m^* ($\approx$0.2–0.3), free carrier densities of 3×10^{20} cm^{-3} suffice to achieve a crossover of $\approx$1500 nm. However, as m^* approaches $\approx$0.6 or higher, depending on ε_∞, instances exist where even 1×10^{21} cm^{-3} will not result in a $\approx$1500 nm crossover. Thus, amongst the two material specific properties, m^* plays the critical role in determining the crossover wavelength.

parameter dm/dE is desirable, as an increase in average effective mass is the primary driver of index change. Moreover, since this is an absorption driven affect, a high mobility (μ) is not desirable as this decreases the optical loss (scattering time, $\tau = \mu m^*_{avg}/e$) and thus the absorption of the pump (A_{pump}). However, a low mobility also leads to a shallow index dispersion (dn_{probe}/dm^*) which hampers the magnitude of index change. Work by Secondo *et al.*[40] captures this trade-off between steep index dispersion and absorption of the pump, in a figure of merit (FoM) given by

$$FOM_{IR} = A_{pump}\left[\frac{1}{m^*_{avg}}\frac{dm}{dE}\right]\left[\frac{1}{N_c}\frac{dn_{probe}}{dm^*}\right], \tag{17}$$

where m^*_{avg} is the average effective mass of electron in CB, dm/dE is the change in effective mass as a function of energy levels (in other words, CB non-parabolicity) and dn_{probe}/dm^*_{avg} denotes the index dispersion with respect to the average effective mass. On the other hand, in the case of interband nonlinearities, a small CB non-parabolicity parameter is desirable since the effective mass tends to increase for high momentum states in non-parabolic bands, limiting the contribution of the added electron to Drude response. Thus, a quasi-parabolic bound would ensure that each excess electron in the CB experiences an approximately constant m^* regardless of its location in band. Moreover, since absorption is dictated by loss at the band edge rather than free carrier absorption in the ENZ region, the absorption-dispersion trade-off of the intraband case is removed such that the loss at ENZ (mobility) is desired to be low (high) to obtain a steep index dispersion. As a result, materials stand to benefit from a lower loss at ENZ and higher absorption at the pumping frequency with the limit arising due to impedance matching when the refractive index at ENZ approaches zero. A recent work by Secondo *et al.*,[148] captures the intricacies of interband pumping with a FoM given by

$$FOM_{UV} = \left[\frac{A_{pump}}{E_g}\right]\left[\frac{1}{N_c}\frac{dN_c}{dE}\right]\left[\frac{-1}{m^*}\frac{dn_{probe}}{dN_c}\right], \tag{18}$$

where E_g is the bandgap and N_c, is the free carrier density. Here, the absorption is normalized by the bandgap energy, as wide-bandgap materials require more energy to generate the same number of excess carriers, due to the relation: $\Delta N_c \propto A/\hbar\omega$ with $\hbar\omega > E_g$. Finally, a large initial free carrier density or a high effective mass tend to decrease the efficiency per unit energy. Table I summarizes the desired materials properties with respect to inter- and intra-band nonlinearities at telecommunication wavelengths. These properties can be readily found in TCOs and perovskite oxides and will be discussed next.

2. Transparent conducting oxides

Transparent conducting oxides (TCOs) are a group of semiconductors that are highly conductive, yet transparent, especially across the visible spectrum. They have been used in several applications for over 70 years, with initial studies dating back to early 1900s.[234,235] While ITO is by far the most widely used TCO, across all applications, some of the other well explored materials have been impurity-doped ZnO, In_2O_3, and SnO_2, as well as multicomponent oxides composed of combinations of these binary compounds [Figs. 16(a) and 16(b)].[232] These materials have been tailored for various opto-electronic applications which favor properties such as high transmission in the visible, high conductivity, high refractive index, reduced use of In (scarce compound in nature) or a combination of the above. On the other hand, ENZ nonlinearities benefit from materials that exhibit a low m^*, low ε_∞, and accept high levels of doping, as summarized in Table I.

While there have been no reports that screen all these parameters, a study by Hautier *et al.*[233] does so for electron effective mass and bandgap. They filter the periodic table for binary and ternary oxides with low effective masses and a bandgap higher than 3 eV calculated using the *ab initio* method. They conclude that while it is unlikely to find oxides with substantially lower effective masses than that of ZnO and In_2O_3, there exists a whole range of compounds that exhibit similar effective masses, including $ZnSb_2O_6$, Cd_2GeO_4, and $Cd_2Ge_7O_{16}$. Unfortunately, all the compounds, except $ZnSb_2O_6$, either contain toxic or scarce elements. Some other compounds such as $CdGa_2O_4$, $MgIn_2O_4$, $ZnGa_2O_4$, Ga_2O_3, and $InGaO_3$ also exhibit low effective masses, but have a bandgap between 1 and 3 eV.[233] Although not suitable for use as TCOs, these materials can be explored for their potential ENZ properties in the NIR and MIR. While estimates of low effective mass from *ab initio* calculations is certainly a step in the right direction, future studies are needed to estimate dopant solubility limits, CB non-parabolicity and other related metrics.

One such work by Secondo *et al.*[40] analyses an eclectic but limited mix of conducting oxides and nitrides for their intraband nonlinearities. They study the band structures of ZnO, ITO, Ga_2O_3, GaN, and CdO and find that the CB non-parabolicity of all considered materials lies within a factor of 2, with Ga_2O_3 exhibiting the highest non-parabolicity. As a result, the work concludes that the nonlinearities will

TABLE I. Inter-band vs intra-band nonlinearities and associated desirable material properties.

Parameter	Inter-band excitation	Intra-band excitation
Effect on plasma freq. (ω_p)	Blue shifts	Red shifts
Driving factor	Increase in N_c in the CB	Increase in m^*_{avg} of the CB
Free carrier density	Moderate (ENZ at or > 1550 nm)	High (ENZ at 1550 nm)
Mobility	High [>60 $cm^2/(V\,s)$]	Low [≈ 20 $cm^2/(V\,s)$]
Effective mass	Low (<0.3 m^*_{avg})	Low (<0.3 m^*_{avg})
High frequency contribution ε_∞	Low	Low
CB non-parabolicity	Low	High
Bandgap	Small, but > ≈ 1 eV	Not critical, but > ≈ 1.6 eV[a]

[a]Not critical, but over 2 times that of operating frequency to avoid 2 photon absorption.

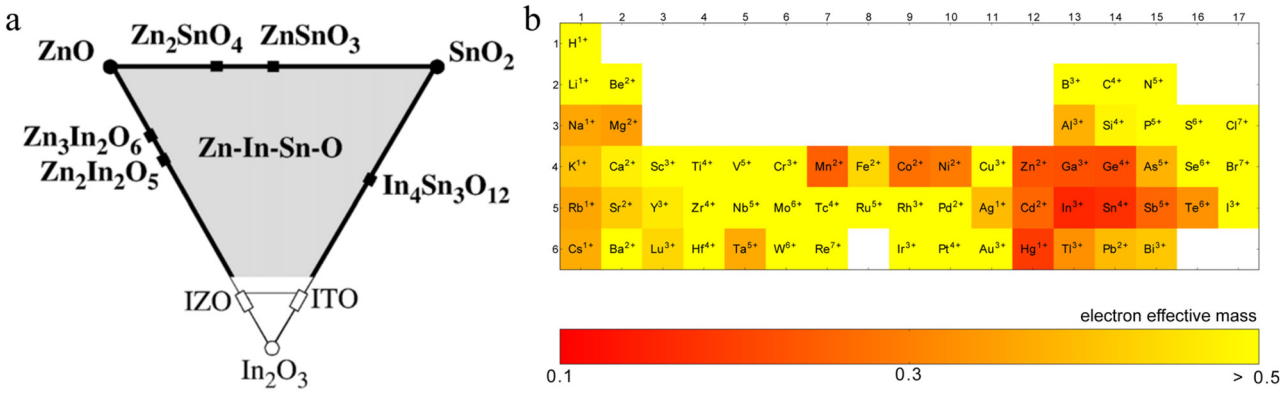

FIG. 16. (a) Summary of useful TCO materials such as ZnO, In_2O_3, SnO_2, and their multicomponent oxides.[232] Reproduced with permission from Minami, Thin Solid Films **516**(7), 1314–1321, (2008). Copyright 2007 Elsevier B.V. (b) Lowest effective mass of each cation plotted in rows and columns of the periodic table for binary and ternary oxides.[233] Reproduced with permission from Hautier *et al.*, Chem. Mater. 26(19), 5447–5458, (2014). Copyright 2014 American Chemical Society.

be in the same order of magnitude as well. Figure 17(a) elucidates the role of loss in these films. The peak FOM is achieved for ZnO films with mobilities in the range of $\approx 15\,\mathrm{cm^2/(V\,s)}$ ($\varepsilon''(\omega_{pump}) \approx 0.6$), as high mobility films suffer from decreased absorption while low mobility films suffer from a shallow index dispersion. This is in stark contrast to UV pumping, which benefits from a high mobility as the absorption of the pump is dependent on interband transition and not Ohmic losses.

Since mobility is critical to the performance of TCOs generally, especially when pumping at energies above the bandgap, it is imperative to maximize this for a given material. The mobility of degenerately doped TCOs is mainly limited by ionized impurity scattering, i.e., Coulomb interactions between electrons and the dopants.[237,238]

Furthermore, the dopant also influences the material's band structure and effective mass. Taking the example of Sn-doped In_2O_3 (ITO), the strong orbital hybridization between the Sn and In 5s states is known to renormalize the CB minima, thus leading to a higher effective mass and in turn, a lower mobility. In addition, since each Sn dopant can only donate a maximum of one excess electron into In_2O_3, a high doping density of Sn is required to achieve free carrier densities leading to NIR ENZ wavelengths. This illustrates that while ITO has been widely used, Sn is not an ideal dopant for In_2O_3.[239–243] In search of better suited dopants, Xu *et al.*[244] report on Zr, Hf, and Ta as dopants for In_2O_3. This is due to the size and orientation of the 5d orbital and localized 5d defect states. Recent experimental data also support these findings.[245–247] For example, Swallow *et al.*[236] show that Mo doping exhibits higher mobility than Sn doping of In_2O_3 across carrier concentrations up to $6 \times 10^{20}\,\mathrm{cm^{-3}}$ [Fig. 17(b)]. Due to the minimum perturbation of the CB with Mo doping, it also has a narrower CB dispersion with a

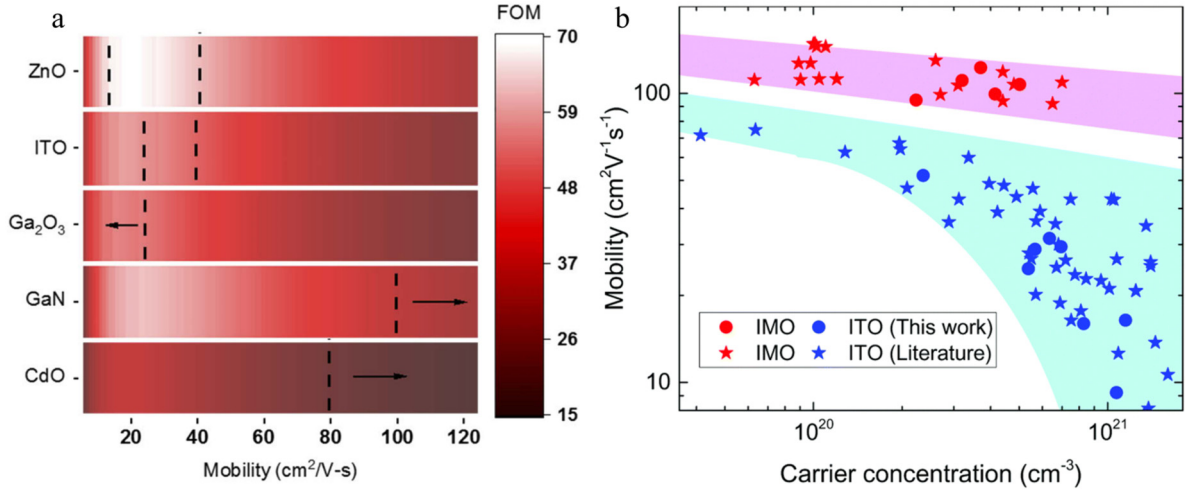

FIG. 17. (a) Figure of merit for the selected materials as a function of mobility, based on Eq. (17). Gray dashed lines represent the range of mobilities achieved by films published in literature.[40] Reproduced with permission from Secondo *et al.*, Opt. Mater. Express **10**(7), 1545 (2020). Copyright 2020 Optical Society of America (b) Figure plots the hall mobility vs free carrier concentration for Sn and Mo doped indium oxide films. In this carrier concentration regime, the electron mobility is limited by ionized impurity scattering.[236] Reproduced with permission from Swallow *et al.*, Mater. Horizons **7**(1), 236–243, (2020). Copyright 2020 Royal Society of Chemicals.

lower effective mass than ITO. This results in Mo:In_2O_3 being well suited for both interband and intraband pumping studies. Similarly, InZrO was recently explored for its nonlinearity in a recent work by Ghobadi *et al.*[42] While a comparison of InZrO NL with other TCOs was not in the scope of the work, the films exhibited mobilities on the order of $\approx 70\,cm^2/(V\,s)$, higher than what is commonly seen with commercially available ITO, indicating a strong potential for an improved nonlinear response at ENZ.

3. Perovskite oxides

Perovskite oxides are a group of inorganic compounds with an ABO_3 type chemical formula, where the A site cation can be an alkaline earth (Mg, Ca), a rare-earth (Nd, Y) or an alkali element (Na, K), the B site cation can be a transition or post-transition metal element from periods 4, 5 or 6 (Cu, Ti) and where O is an oxygen anion.[248] A basic perovskite oxide structure is shown in Fig. 18(a), where the B cations reside at the center, A at the corners and O at the middle of the faces. This forms a unit cell of a more complex 3D framework where the B cations are octahedrally coordinated to oxygen atoms, and the BO_6 octahedra shares corners across the three directions of the crystal [Fig. 18(b)]. This framework leads to these materials exhibiting a range of interesting properties such as superconductivity,[249] metal-insulator transition,[250] photovoltaic effect,[251] ferroelectricity,[251,252] and transparent conductivity.[253–257] These wide-ranging properties, which are due to strong interactions between the charge, orbital, structural and spin properties, enable the realization of devices with functionalities beyond those possible with standard semiconductors. Arguably, perovskites represent one of the most important crystal structures among transition metal oxides.

In addition to the above-mentioned properties, some perovskites have been shown to exhibit high room temperature mobilities and can accept large levels of doping.[254,256,258] These enhanced electronic properties are mainly the function of relatively large static dielectric permittivity, which promotes screening of the electron-charge interaction.[259] The combination of rich electronic properties and the potential to exhibit zero permittivity in the NIR, makes these materials an attractive alternative to conventional TCOs, especially as this could result in devices with greater functionality.[248,260–262]

Some of the more heavily explored perovskite oxides have been stannates,[258] vanadates,[263] titanates,[264,265] and germanates.[266] While most of these can be readily grown with high doping levels, titanates and vanadates are known to exhibit large effective masses ($BaTiO_3$:5.4m_0, $SrVO_3$:3.0m_0), making them unsuitable for ENZ nonlinearities. The large effective mass primarily arises from strong electron correlations in these materials. Titanates and vanadates have partially filled d-orbitals in their crystal structure, which interact strongly with each other and with the oxygen ions in the structure, via Coloumbic and exchange interactions. Because of this strong interaction, the electrons behave more like heavy particles with high effective mass.[256,267,268] On the other hand, stannates and germanates, have been shown to exhibit low effective masses ($SrGeO_3$:0.22m_0 and $BaSnO_3$:0.19m_0).[259,266,269] Unlike titanates, which have the CB minima dominated by the localized 3d states, first-principal calculations show that CB minima is dominated by dispersive Sn and Ge 5s states, leading to smaller effective masses.[269]

Among several potential stannates and germanates, doped $BaSnO_3$ is particularly promising for ENZ nonlinearities, due to the following properties: mobilities ranging in between 50 and $350\,cm^2/(V\,s)$, effective masses below 0.25m_0, ε_∞ of 4.5 and free carrier densities up to the mid $10^{20}\,cm^{-3}$ range.[254,270,273,274] However, there is a dearth of literature exploring the ENZ properties of $BaSnO_3$. More recently however, it was explored for its NIR plasmonic properties as an alternative plasmonic material. Yang *et al.*[272] deposited La doped $BaSnO_3$ using sol-gel method and showed that infrared plasmons sustained by it are superior in spatial confinement ratio compared to those in noble metals, primarily due to their lower carrier densities which places the plasmon energies in the region of interest, IR in this case [Figs. 19(f) and 19(g)]. Similarly, Kim *et al.*[270] demonstrated epitaxial $BaSnO_3$ films on $SrTiO_3$ with a crossover wavelength as low as 2050 nm and a mobility of $65\,cm^2/(V\,s)$ [Figs. 19(a) and 19(b)].[270] With crossover wavelengths approaching the telecommunication window, IR pumping also becomes potentially feasible. In this sense, $BaSnO_3$ is very attractive, as the CB non-parabolicity parameter is

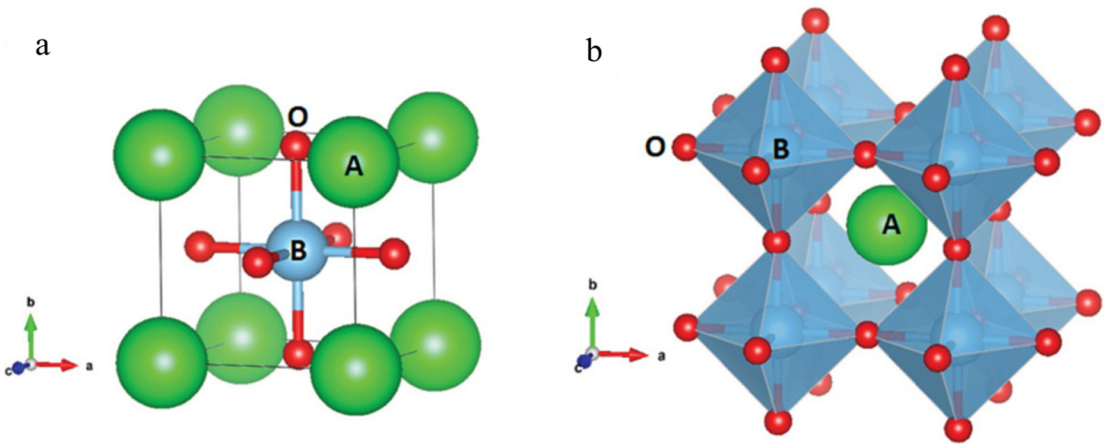

FIG. 18. (a) Schematic of a basic perovskite unit cell.[248] (b) The unit cell is part of a more complex 3D framework where B cations are octahedrally coordinated to oxygen atoms, and the BO_6 octahedra shares corners across the three directions of the crystal.[248] Reproduced with permission from Sun *et al.*, Adv. Energy Mater. **11**(2), 2000459 (2021). Copyright 2021 Wiley-VCH.

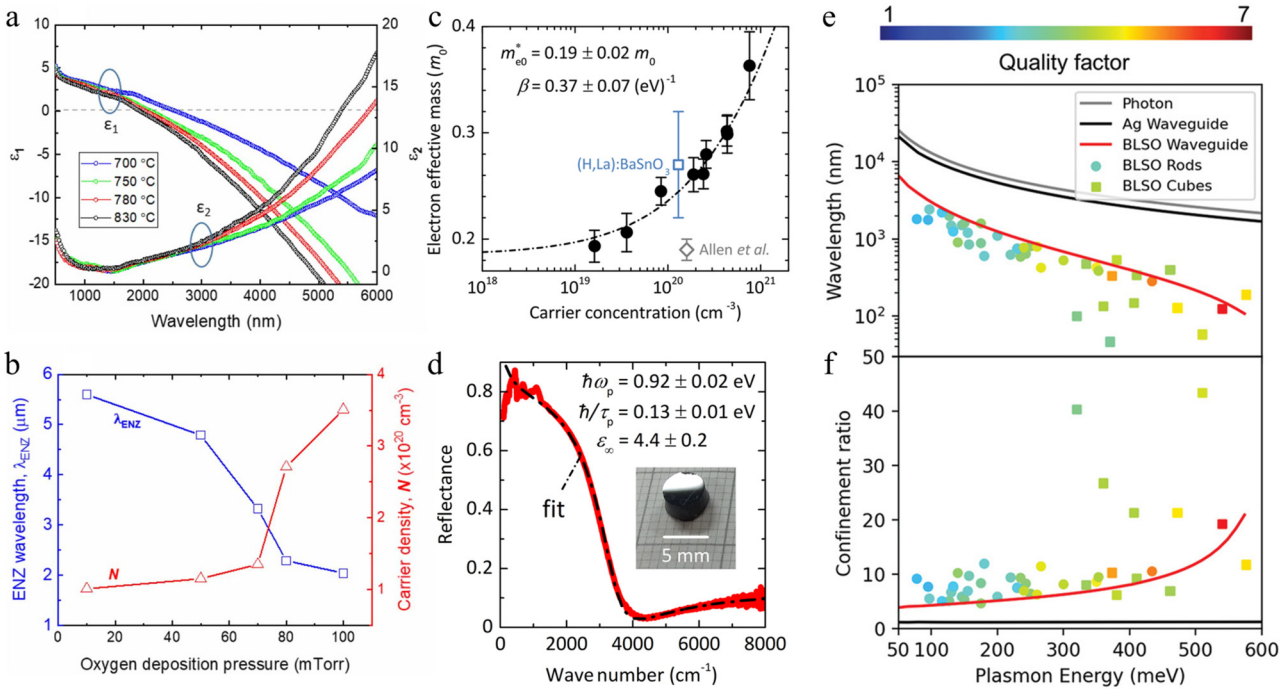

FIG. 19. (a) Real (ε_1) and imaginary (ε_2) parts of permittivity of 100 nm thick LBSO films deposited on $SrTiO_3$ substrates at various temperatures (700–830 °C).[270] (b) ENZ wavelength and carrier density of the LBSO films as a function of oxygen deposition pressure.[270] Reproduced with permission from Kim *et al.*, J. Phys. D **53**(36), 365103 (2020). Copyright 2020 IOP Publishing. (c) Average effective mass of the electron in CB as a function of free carrier density for La:$BaSnO_3$ films.[271] Reproduced with permission from Niedermeier *et al.*, Phys. Rev. B **95**(16), 161202 (2017). Copyright 2017 American Physical Society. (d) IR reflectance spectrum of La:$SrGeO_3$ polycrystalline pellet.[259] Reproduced with permission from Niedermeier *et al.*, Phys. Rev. B **101**(12), 125206 (2020). Copyright 2020 American Physical Society. (e) Measured IR plasmon wavelengths in La:$BaSnO_3$ nanoparticles (symbols) compared with calculated values obtained for La:$BaSnO_3$ (red curve) and Ag (black curve) waveguides with a cross section of $50 \times 50\,nm^2$. Also shown is the free-space photon dispersion (gray curve) for reference. (f) Confinement ratio obtained from (e) as the ratio of the plasmon excitation wavelength to the free-space photon wavelength.[272] Reproduced with permission from Yang *et al.*, Small **18**(16), 2106897 (2022). Copyright 2022 Wiley-VCH GmbH.

experimentally determined to be $\beta \approx 0.37\,eV^{-1}$, which is over twice as large as that of ITO ($\beta \approx 0.18\,eV$) and GZO ($\beta \approx 0.14\,eV$), as shown in Fig. 19(c).[271]

One other perovskite oxide of interest is doped $SrGeO_3$. It has properties like that of $BaSnO_3$, with undoped $SrGeO_3$ predicted to exhibit mobility as high as $390\,cm^2/(V\,s)$.[259,275] In a recent work by Nierdermeier *et al.*,[259] single crystal La doped $SrGeO_3$ was grown, which resulted in a mobility of $42\,cm^2/(V\,s)$ at free carrier densities of $1.5 \times 10^{20}\,cm^{-3}$. Furthermore, from the sharp rise of reflection in the reflectivity spectra, we can conclude that the permittivity crossover occurred between wavelengths of 2500 and 3000 nm in these samples [Fig. 19(c)]. More interestingly however, the authors establish a guideline for the exploration of high mobility semiconductors. A combination of small effective mass and large polarization of the hardest LO mode should support high room temperature mobilities despite electron–phonon interactions. While $BaSnO_3$ and $SrGeO_3$ have been actively explored, alkaline earth stannates such as $ASnO_3$ (A = Sr, Ca, Zn, and Cd) have also been predicted to have effective masses and band gaps in the range of 0.15–0.25 and 1.5–4.5 eV, respectively.[256,262,269,276–279] However, as evident from the sparse literature available for epitaxial films or single crystals, these materials have yet to be widely investigated.

Several of the perovskite oxides appear to be promising candidates for ENZ nonlinearities, however very few reports have explored these materials. This is primarily because the properties of these materials are not substrate agnostic, often requiring the use of precisely lattice matched substrates to achieve the frequently touted record electrical properties. Work by Kim *et al.*[273] reported that single crystals of $BaSnO_3$ exhibited mobility in the range of $200–320\,cm^2/(V\,s)$ (with carrier densities 1×10^{19} to $4 \times 10^{20}\,cm^{-3}$), while epitaxial films exhibited $70\,cm^2/(V\,s)$. This was mainly attributed to increased carrier scattering due to dislocations and grain boundaries, which were presumably created by the 4% lattice mismatch between the substrate $SrTiO_3$ and La:$BaSnO_3$. Such stringent conditions of lattice matching and careful tuning of the deposition parameters result in scarce availability of the oxides. Thus, from a practical standpoint, a method to achieve high quality films on various substrates is highly desirable. To address this issue, researchers have explored methods to transfer these films using various methods such as sacrificial etching, mechanical exfoliation and spalling.[280] For example, the family of water soluble $(Ca,Sr,Ba)_3Al_2O_6$ materials have been used as a sacrificial layer. Not only do these materials have a good structural and chemical compatibility with perovskite oxides, but their lattice parameters can be tuned from 0.3819 nm (100% Ca) to 0.4124 nm (100% Ba). This presumably could lead to not only easier access to perovskite oxides, but also improved compatibility with device fabrication processes. Finally, to provide a quantitative estimate of improvement, Fig. 20 compares some of the upcoming perovskites to other widely explored TCOs.

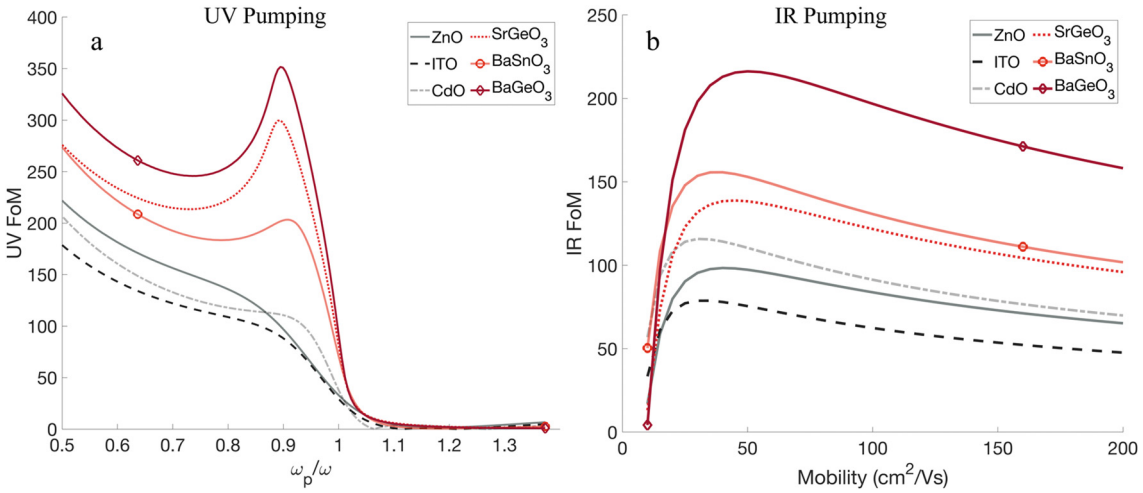

FIG. 20. To compare some of the upcoming perovskites to the commonly used TCOs, this figure plots the UV and IR figures of merits against normalized plasma frequency and mobility, respectively. (a) UV FoM shown against samples with varying plasma frequencies normalized to the frequency ω corresponding to free-space wavelength of 1550 nm, which can also be thought of as samples with varying carrier concentrations. (b) IR FoM shown against samples with varying mobilities. The carrier concentration is adjusted such that each of these materials exhibit a crossover wavelength of 1550 nm. A detailed list of assumptions can be found in Tables S2 and S3.

Figure 20(a) plots the figure of merit of these materials [Eq. (18)] when pumped above the bandgap with enough power to excite a free carrier concentration of $1 \times 10^{20}\,\mathrm{cm}^{-3}$. The FoM is plotted as a function of different starting base plasma frequencies (or varying free carrier densities) normalized to the frequency corresponding to 1550 nm. The power needed to excite a free carrier concentration of $1 \times 10^{20}\,\mathrm{cm}^{-3}$ ranges from 10 to 50 GW/cm^2, if 100% of the incident energy is absorbed. Other assumed parameters are shown in Table S2 and S3. Due to a combination of low base effective mass (m^*_{avg}, lower scattering rate, thus steeper Drude dispersion), moderate band non-parabolicity (dm/dE, lower counteraction to increasing N_c) and high mobility (μ, steeper Drude dispersion), $BaGeO_3$ is predicted to outperform all other materials under the assumed conditions. Furthermore, perovskites are predicted to outperform the commonly used TCOs by a factor of at least 2, within their ENZ spectral region around 1550 nm. Figure 20(b), on the other hand, plots a figure of merit of these materials when they are pumped in the IR, at their respective ENZ wavelengths, as a function of mobility. The carrier concentration of all the materials has been adjusted such that they exhibit an ENZ wavelength of 1550 nm. While conduction band non-parabolicity has been thought of as the metric to determine the strength of IR nonlinearity, it turns out that effective mass is just as important, if not more. This is observed by the fact that, while CdO has the largest dm/dE, it is outperformed by all perovskites with lower non-parabolicities. This is because of low m^*_{avg}, especially observed in $BaGeO_3$. Furthermore, although the dm/dE term, of $BaGeO_3$, is much lower than most materials in the graph, it is the low m^*_{avg} that drives the outperformance. This leads further credence to the fact that m^*_{avg} is an important parameter to consider, as was evident in Fig. 15 as well. Ultimately, both figures highlight the complex interplay that exists between these parameters, underscoring the need for in-depth DFT based modeling and experimental exploration to improve the performance of nonlinear materials utilizing ENZ effects.

In summary, semiconductors such as doped tin, zinc, Cd, and perovskite oxides have been explored for their properties as a transparent conductor. Key to this is transparency in the visible, or a large bandgap. Some of these materials have also found their way into the field of ENZ nonlinearities and led to fascinating demonstrations. However, materials tailored for ENZ nonlinearities, especially in the telecommunication spectrum, do not need to have a large bandgap. In fact, a smaller bandgap would enable interband pumping of these materials in the visible spectrum, which is more readily accessible. Furthermore, parameters such as CB non-parabolicity and effective mass are arguably more important than overall conductivity or transmission through the visible spectrum (which are key to good TCOs). Furthermore, the general push so far has been toward improving mobilities, which is not strictly required, especially considering intraband nonlinearities. Therefore, a significant opportunity lies in moving beyond conventional TCOs, exploring materials that have been tailored for ENZ nonlinearities and not just adopted. Furthermore, with the advent of AI/ML based high throughput material discovery pipelines,[281–284] the process of discovering materials is only being accelerated. While the research community might conclude that ENZ nonlinearities using conventional TCOs are the best we can achieve, the possibility of not only drastically improving light–matter interaction, but also bringing it into the realm of practicality, makes this question worth exploring.

B. Time varying physics with ENZ media

In addition to the search for new materials to optimize nonlinear interactions in ENZ, there has been a surge of interest in exploring time-varying optical interactions. These interactions, which we generally classify as time varying effects, occur when a photon interacts with a material or refractive index perturbation moving near the speed of light, and includes perturbation that can have either, temporal or spatiotemporal variations. While early theoretical works considered moving mirrors as a test case,[285] the ability of homogeneous ENZ materials to provide a unity-order index change on the sub-picosecond scale is quite an interesting combination. It facilitates the exploration of the

unique effects of time-varying interactions without needing to accelerate a material to near the speed of light.

The inclusion of time as an additional degree of freedom in engineering light–matter interaction is of particular interest because of various exotic physical phenomena associated with this approach. One such prominent effect that arises from light propagating in a time-varying medium (TVM) is frequency conversion. Historically, the concept had its roots in plasma physics, with early exploration focused on the realm of relativistic photon propagation[286–291] where the interaction of intense laser pulses with dense gaseous mediums yielded a moving ionized plasma front. The generation of free carriers during ionization caused temporal variations in the medium's refractive index along the trajectory of the pulse. The interaction of photons with this dynamic front, acting as a moving "mirror" of sorts (where the increasing free carriers in the Drude term correspondingly decreased the refractive index, leading to heightened reflectivity), resulted in a frequency upshift of the propagating photons. As we advanced into the 21st century, the concept of TVM expanded its horizons to encompass a broader array of optical mediums ranging from tens of kHz to hundreds of THz, through acousto-optics, microwave-based system, optomechanics, metamaterials and more recently, epsilon-near-zero (ENZ) films.[292] The significance of the frequency conversion achieved through these techniques is noteworthy for several reasons.

For many of the techniques used to achieve frequency conversion, including ENZ films, the process is a non-resonant process. It predominantly acts upon the linear refractive index and facilitates the spectral transference of electromagnetic energy without being bound by conventional phase matching conditions or selection rules, thereby introducing the potential for continuous and deterministic frequency adjustments.[291] While conventional nonlinear optical descriptions can be used to describe the effect, e.g., four-wave-mixing, frequency conversion via TVMs is distinct in that it results in the frequency conversion of all photons within the material. Continued development in this realm holds the promise of providing new avenues to address spectral gaps[293] that arise from varying operational regimes of different optical network components (emitters, detectors, fibers, etc.). Additionally, unlike conventional $\chi^{(2)}$ based systems limited by phase matching conditions,[294] TVM-based frequency conversion can dynamically convert photon frequency while preserving quantum states, bridging spectral gaps, and advancing quantum network realization.[295–297]

Beyond frequency shifting, another noteworthy time-varying effect is the generation of a time-reversed (TR) wave. Upon interaction with the temporal interface formed with the abrupt perturbation in material index, electromagnetic waves can evolve into a new state with its phase evolving backward in time.[298–300] Although modern signal processing techniques have already enabled the generation of time-reversed waves in lower frequency systems,[299] its implementation in optical regime is quite complicated as requires independent control over spatial, temporal and polarization degrees of freedom.[301] TVM-induced TR generation is attractive in this regard because it does not rely on sampling or recording, as needed for in signal processing. However, the requirement of ultrafast and uniform change of medium properties remains a challenge in realizing optical TR in TVM.[302]

TVMs also allow for realizing highly sought after nonreciprocity in linear optical system with broken time-reversal symmetry. Nonreciprocity via temporal modulation is achieved by allowing directional mode conversion between orthogonal traveling modes under phase matching conditions which is fulfilled only for either forward or backward propagating wave, and thus, provides isolation for the restricted direction without bulky traditional magneto-optic biasing.[303–305] Overall, the time-varying physics discussed above can lead to versatile application scopes like inverse prisms,[306] "perfect lens" for subwavelength imaging,[307] imaging in random media,[308] optical circulators,[309] optical power combiners,[310] temporal beam splitters,[311] Fresnel drag,[312] surface wave generation with temporal grating without subwavelength fabrication,[313] temporal waveguides,[314] antireflection temporal coatings,[315] temporal aiming of pulses,[316] all-optical beam steering,[317] pulse shaping,[318] as well as interesting physics like temporal diffraction and interference[319–321] to name a few. For further information on time-varying physics, please see the following review.[292]

Clearly, adding the time-dimension to our ability to control light is crucial and unlocks quite unique and impactful opportunities. As we move ahead, we will dig more deeply into how some of these effects can be realized utilizing ENZ media. We will start with one of the hallmarks of TVMs, frequency shifting, highlighting the factors that limit achievable frequency shifts in realistic scenarios. Within this context, we will also review the experimental endeavors related to both ENZ and non-ENZ approaches, aiming to assess the advantages and limitations of each scheme. Following that, we will briefly discuss the dynamics underlying the generation of time-reversed waves, along with an overview of reported implementations in the literature. Finally, we will introduce and briefly evaluate a prominent application direction within TVM, referred to as the "photonic time crystal" while considering its potential for realization within the optical realm.

1. Frequency shifting in TVM

While TVMs offer a broad range of distinct yet unique phenomena to be explored, e.g., photon acceleration,[322,323] time-reversed wave generation,[298,300,324] photonic time crystals,[325–327] a common thread among them is the frequency shift experienced by EM waves. Hence, most of the recent experimental endeavors in realizing optical TVM have been directed toward frequency shifting.

The fundamental physics behind frequency shift can be explained from the standpoint of simple geometric optics. As light crosses a boundary between media with different properties, its trajectory maintains translation symmetry to preserve tangential momentum. In static media, an interaction with the boundary conserves the energy or frequency (ω) but modifies the momentum or wavevector (k), as shown in Figs. 21(a) and 21(b). This process leads to the well-known formula of refraction or general Snell's law to determine the propagation direction of light from the relation $n_1 \sin\theta_1 = n_2 \sin\theta_2$ where n_1,θ_1 (n_2,θ_2) denotes the index and angle of the incident (refracted) light respectively. In contrast, when light encounters a "temporal" boundary formed through an abrupt change in the refractive index of a homogenous medium at some specific instant of time, the wavevector (k) representing the spatial distribution of light energy—must remain constant. However, the index of the media has been altered. Thus, to maintain this momentum, the frequency, $\omega = kc/n$, adjusts to compensate for the sudden change in refractive index. Moreover, waves interacting with such a "time boundary" produce a "time-refracted" and 'time reflected/reversed' wave in a similar fashion as is observed at a spatial boundary. However, since the time axis is unidirectional, the "reflected" wave cannot go back in time, and both the refracted and reflected waves spatially propagate with different frequencies and

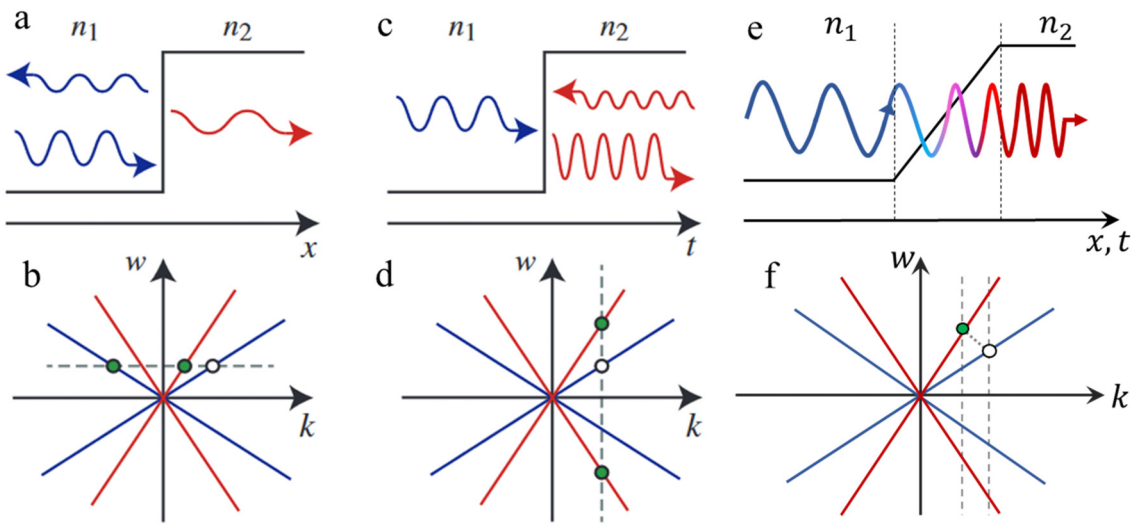

FIG. 21. Illustration of the generalized concept of refraction and reflection for (a) and (b) space ($dn/dt = 0$) (c) and (d) time ($\frac{dn}{dt} \rightarrow \infty$) and (e) and (f) space-time ($dn/dt \approx$ finite) boundaries. The lower panels (b), (d), and (f) depicts the corresponding change in wavevector and/or frequency in the phase space diagram depending on the type of interface encountered during propagation. When the change from n1 to n2 happens over a time longer than the period of the input wave, adiabatic changes occur to both wavelength and frequency as shown in (e) and (f). Figures (a)–(d) are adapted from Galiffi *et al.*, Adv. Photonics **4**(1), 014002 (2022). Copyright 2022 Author(s). Licensed under a Creative Commons Attribution License.

phases according to $\omega_2 = \omega_1.(\frac{n_1 \sin\theta_1}{n_2 \sin\theta_2})$ and $\omega_3 = \omega_1.(\frac{\sin\theta_1}{\sin\theta_3})$, where ω_1 (θ_1), ω_2 (θ_2), and ω_3 (θ_3), are the frequencies and angles of propagation (with respective to normal to the temporal interface) for the incident, time-refracted and time-reflected beams, respectively at any time t [Figs. 21(c) and 21(d)].[291] This geometric approximation holds for an ideal scenario of a nondispersive medium where the index variation can be instantaneous (e.g., the index boundary has infinite speed). However, causality and the non-instantaneous response of physical materials cause the index change in the media to happen at a "fast" but finite speed (i.e., index boundary moves at $v_g \approx c$). From a relativistic perspective, in this case, a more general space-time refraction effect occurs where both the frequency and momentum of propagating light must change to conserve energy and momentum [Figs. 21(e) and 21(f)]. Such relativistic events are often explained from various perspectives including photon acceleration,[322,328,329] photon energy lifting,[330] and self-phase modulation[331] where the frequency of the light is gradually modified, or "adiabatically shifted" from one frequency to another due to the interaction with the moving boundary, very similar to an acoustic Doppler shift.

Frequency conversion through TVMs is important because unlike nonlinear wave mixing processes, this process is not restricted by conditions like phase matching or photon energy conservation and can have 100% internal conversion efficiency for all photons within the TVM, leading to a shift of entire spectrum. Furthermore, the final frequency shift can be tuned by adjusting the strength of the index modulation.

The basic expression for TVM induced frequency shift can be simply derived by taking the time derivative of momentum conservation condition $k(\omega)c = \omega n(\omega)$, given as

$$\frac{d}{dt}(\omega n) = \omega \frac{dn}{dt} + n\frac{d\omega}{dt} = \frac{d}{dt}(kc) = 0; \rightarrow \frac{d\omega}{\omega} = -\frac{dn}{n}. \tag{19}$$

The above equation shows the direct relationship between frequency shift and index modulation. Note here, the expression for frequency shift in Eq. (19) is not exact and only valid for qualitative analysis, one must resort to a full derivative approach to account for dispersion and other relevant complexities in a quantitative analysis.[132] Along with index modulation, another important factor is how fast the change occurs. In a TVM, modulation occurring on a timescale shorter than the cycle time of the signal wave effectively creates a temporal boundary [Figs. 21(c) and 21(d)] whereas longer yet comparable modulation time leads to the space-time boundary scenario [Figs. 21(e) and 21(f)]. The magnitude of frequency shift occurring from the interaction with any of these two boundaries therefore depends primarily on two factors—(a) modulation strength (larger the dn, more shift), and (b) modulation duration (the time, Δt_{change} it takes for the index to change by $dn_{\max}$) in comparison to the cycle of interacting wave.

To realize temporal boundaries in the optical regime (≈100s of Terahertz scale) the modulation period (Δt_{change}) needs to be less than or approximately on the order of 1–10 fs scale. Given that, achieving femtosecond-scale modulation of permittivity is most likely feasible through optical methods such as nonlinear interactions via electron polarization or free carrier absorption.[48] In the ideal scenario, when considering instantaneous index changes in a nondispersive TVM, the temporal slope of index change, $\frac{dn}{dt} \approx \left(\frac{\Delta n}{\Delta t_{\text{change}}}\right)$ tends to infinity as $\Delta t_{\text{change}} \rightarrow 0$ implying the relative frequency shift ($\Delta\omega/\omega$) to be proportional only to the relative index change ($\Delta n/n$) for EM field of any frequency [Eq. (19)].

Complexities arise when considering real dispersive materials where the index modulation is limited by strength vs speed trade-off between various nonlinear approaches [refer to Fig. 1(b) and discussion in Sec. IV on types of Drude nonlinearities]. In conventional dielectrics, only the bound electronic polarization nonlinearities can induce the change in susceptibilities on the desired femtosecond

timescale but lack in modulation strength (although recent advances in free carrier effects are enabling fast rise times as well, further details see Sec. IV). For example, with reference to Kerr nonlinearity, the maximum achievable index change (Δn) is on the order of 0.04 for Si and 0.006 for Si_3N_4 in the near IR spectrum even at 1 TW/cm^2 excitation.[332] This is neither sufficient nor practical to achieve any appreciable frequency shift. Another approach of optical frequency shift has been reported with RF signal driven electro-optic modulators by changing the modulating frequency but maximum achievable shift through such process is limited (only a few gigahertz level) and inefficient due to sideband generation.[333,334] This dilemma explains the inherent challenges in developing an optical TVM based frequency converter compared to early experimental approaches employed in various systems such as mechanical,[335] optomechanical,[336] acousto-optic,[337] and electro-optic[338] ranging from kilohertz to gigahertz operational regime. However, space-time refraction relaxes the modulation frequency limit and allows for adiabatic frequency conversion (AFC) with modulation time slightly longer than the optical cycle given that the modulation strength is large. This fits quite well with the strengths of free carrier nonlinearities and has led to several recent studies of AFC using semiconductor, ENZ, and cavity resonance approaches. More on these approaches will be discussed shortly.

AFC in recent approaches can be classified into two types depending on whether the conversion happens to photons residing in a cavity/resonator or while propagating through a medium (film/waveguide). Regardless, the duration or length of interaction plays an important role in improving the efficiency of the adiabatic frequency shift. The modulation duration (Δt_{change}) ideally needs to occur on a timescale less than or equal to the propagation time (t_{prop}) of the signal through the system ($\Delta t_{\text{change}} \leq t_{\text{prop}}$). In the context of resonator/cavity medium, this condition can be interpreted in that the modulation should be much faster than photon lifetime (τ_p) in the cavity while being slower than the cavity round trip time (τ_{rt}) for gradual change to occur ($\tau_{rt} < \Delta t_{\text{change}} \ll \tau_p$).[132]

To further elucidate the interplay between the modulation period and interaction limit, we first need to understand the role of excitation pulse characteristics in the process of index modulation across the TVM. When considering an ideal time boundary in the optical regime, it can be understood as an optically modulated index front moving with an infinite speed. Therefore, all photons within the medium can uniformly and simultaneously experience the induced change. In this case, an implicit assumption for the optical excitation that would induce such instantaneous change in index is to be an impulse or Dirac-delta function of $\int_{-\infty}^{+\infty} \delta(t)dt = 1$ (implying it is a spike of infinite amplitude with no temporal/spatial width). This assumption is based on the fact that the excitation pulse's envelope shapes the spatio-temporal profile of modulated index. However, real-life experiments mostly rely on Gaussian pulses of finite duration and spatial width and the modulated refractive index profile ($n + \Delta n$) in TVM will closely follow the Gaussian envelope of pump.

In general, the spatial (Δ_p) and temporal pulse width (t_p) of a Gaussian pulse are linked with the group velocity ($v_{g,exc}$) via the relation $\Delta_p = v_g\, t_p$. For a fast nonlinearity induced index change, we can assume the propagation velocity of the modulation front to be the same as the group velocity of the excitation pulse ($v_{\text{change}} = v_{g,exc}$). As the modulation closely follows the temporal slope of the pulse front, and hence the modulation duration can be approximated as $\Delta t_{\text{change}} \approx t_p/2$ [Fig. 22(a)].

Because of the finite speed and pulse width of the excitation, it also creates a spatial index gradient along its trail. Because of the gradient, the index modulation of the medium is nonuniform and the index contrast felt by the photons at any instant ($\frac{dn}{dt}$) becomes dependent on the slope of the spatial index profile and its velocity [Fig. 22(b)], which can be expressed as

$$\frac{dn}{dt} = \frac{\Delta n}{\Delta t_{change}} \approx \frac{2\Delta n}{t_p} = \frac{2\Delta n}{\Delta_p}.v_{change}. \tag{20}$$

Therefore, maximizing the index contrast through a traveling modulation front necessitates a spatially and temporally compressed excitation pulse (small Δ_p,t_p), characterized by its short duration. This preference holds true irrespective of the dispersion of the material. Hence, a short pulse with a low group velocity condition is favored for the small spatial width of the excitation pulse. However, it introduces a trade-off between requiring a short pulse and needing it to be fast too [Eq. (20)]. If the group velocity (v_{change}) becomes too low, the process of AFC will not occur. In terms of relativistic photon propagation, the shifted frequency ($\omega_1 \rightarrow \omega_1 \pm \Delta\omega$) owing to the index modulation of the medium ($n_1 \rightarrow n_2$) has been shown to be related to signal photon velocity in the following form:[291]

$$\Delta\omega = \omega_1 \left(\frac{1-\beta_1}{1-\beta_2} \mp 1\right), \quad \text{where } \beta_i = n_i.\frac{v_{change}}{c}. \tag{21}$$

This relation shows that when the modulation velocity becomes too low, this results in almost no frequency shift (as $v_{\text{change}} \rightarrow 0$, consequently $\Delta\omega \rightarrow 0$). On the other extreme, modulation velocity as fast as the signal photons ($\beta \rightarrow 1$) leads to no frequency shift as well, because there is no relative velocity between copropagating the modulation front and probing photons to realize the temporal change. However, in this situation, photons with velocity not same but just above the modulation velocity will theoretically experience a large frequency shift. Yet/However as we have seen from above discussion, fast moving modulation also implies spatial expansion of the excitation pulse ($\Delta_p\uparrow$) which consequently negates the positive contribution of fast-moving modulation toward increasing temporal index contrast $\frac{dn}{dt}$ [Eq. (20)]. The interplay between the amount of index changes and the modulation velocity on the frequency shift based on Eq. (21) has been shown in Fig. 22(d). While it partially explains the intuitive idea of achieving large shift in frequency for faster modulation even with very small index change, the magnitude and direction of change in frequency is counterintuitive for regions of lower modulation velocities [left region of yellow dashed line in Fig. 22(d)]. The reason for such discrepancy in these values compared to the experimental demonstrations can be attributed to the consideration of signal photon's phase velocity in place of group velocity to account for the relativistic effect which reflect neither the dispersion condition present in real materials as an origin of lower group velocities nor the finite size of the medium limiting the interaction time. Therefore, one must exercise caution in interpreting the shift suggested by this formulation and its extensions accounting for counter-propagating modulation front and off-normal incidence as discussed in Ref. 291.

The optimal approach is then to obtain a short pulse width on the timescale of $\frac{1}{f_{\text{signal}}}$, which subsequently allows one to achieve a steep

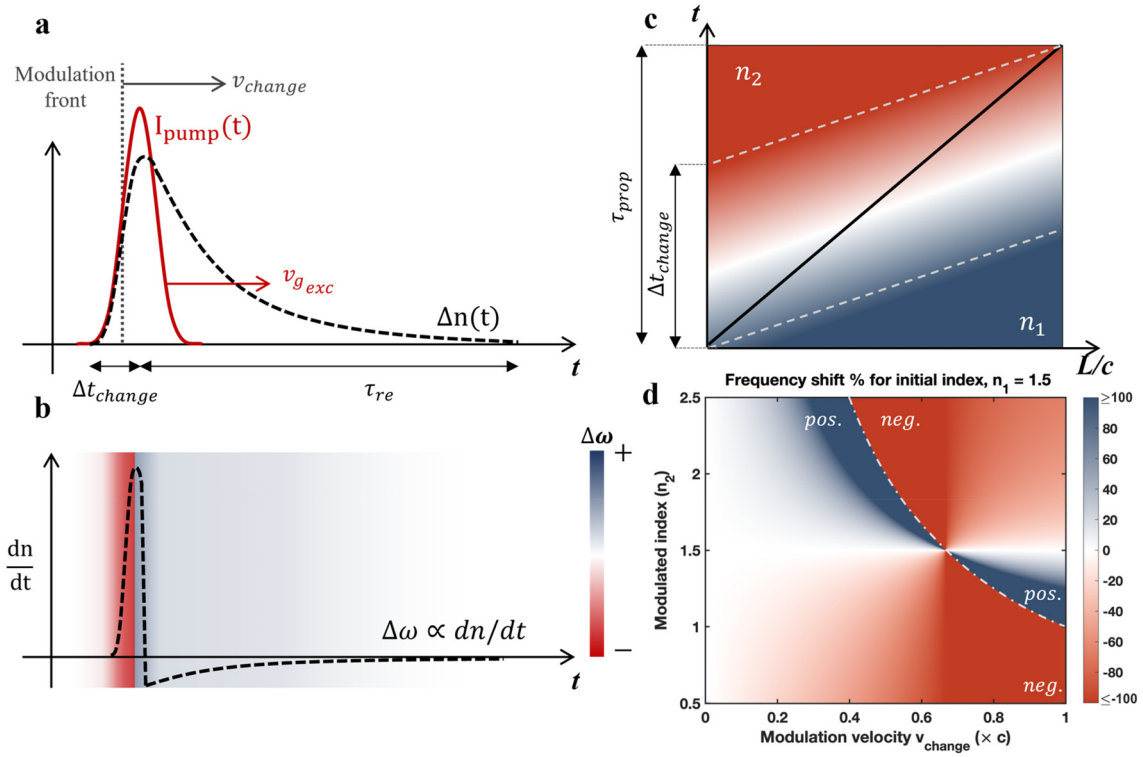

FIG. 22. Illustrations of the frequency shift dynamics depending on spatiotemporal characteristics of optical pump-induced index modulation. (a) Schematic depicting the temporal dynamics of the pump pulse, shown in red and the induced index change, shown in black. As an example, a typical index change profile, of widely explored free carrier nonlinearities involving real transitions, is shown. Since, the rise in the index change is nearly instantaneous and it follows the pump's temporal response, we can assume the propagation velocity of the modulation front to be the same as the group velocity of the excitation pulse ($v_{change} = v_{g,exc}$). Furthermore, since the frequency shift ($\Delta\omega$) is proportional to the rate of change of index (dn/dt), (b) depicts the rate of change of index in a black curve, and underlaid on the figure is the magnitude and direction of frequency shift of the signal photons, which are assumed to be stationary, for simplicity. The shift direction (blue for $\omega_2 > \omega_1$, red for $\omega_2 < \omega_1$) is usually opposite to the change of index experienced by the signal photons according to the time refraction relation given as $\omega_2 = \omega_1\, n_1/n_2$. While both, red and blue shift of the frequency are possible, the largest frequency shift is observed at the rising edge (hence also labeled the modulation front). (c) When considering a finite size medium of length L, and signal photon propagating with a finite velocity v (black line shows the position of signal photon over time, t, the background color corresponds to the index, which varies linearly between n_1 and n_2, and the dashed gray lines correspond to the bounds of index changed experiences by the photon), there exists a bound on Δt_{change}, if the signal photons were to experience the full extent of index change ($n_1 \rightarrow n_2$). The condition is that Δt_{change} should be faster than the propagation time, τ_{prop}, and the interplay is shown in (c). In other words, this implies pulses with small temporal widths are preferred. At the same time, (d) highlights the importance of a large v_{change}. A plot of the percentage shift calculated from Eq. (21) as a function of modulated index, n_2 and modulation velocity v_{change} for photon of base wavelength 1550 nm normally incident upon a nondispersive medium with initial index, $n_1 = 1.5$, is shown. The region to the right of the asymptote (white dashed line) shows that faster modulation velocity achieves large shifts for even smaller index changes. Near the lower extreme of v_{change} the shift becomes negligible. The equation used for the calculation is based on a simplistic model of relativistic photon propagation and therefore shift magnitudes/signs calculated from it are not exact but highlight the need of a large v_{change}. With v_{change} (or $v_{g,exc}$) linked to Δt_{change}, by the relation $\Delta_p = v_{g,exc}\, 2\Delta t_{change}$, there exists a trade-off, since small temporal widths (Δ_p), small spatial widths and large group velocities, are not all simultaneously achievable, especially for fs pulses. Positive (pos.) and Negative (neg.). Panel (c) is adapted from Ref. 132.

$\frac{dn}{dt}$ for a reasonably fast group velocity. Nonetheless, achieving this is technically challenging and constrained by the operating frequency. Contemporary ultrafast laser technology allows the generation of femtosecond pulses below 10 fs which is almost on the scale of a single optical cycle (≈1 fs to ≈10 fs) for central wavelength ranging from visible to mid IR (≈300 nm to ≈3 μm).[132] However, as 30–100 fs pulses are more common, alternatively, one could work with a longer pulse and slow them down so long as the speed of the index front is sufficient to achieve frequency shifting.

With the understanding of pulse characteristics and its impact on the induced modulation profile, we can revisit our discussion on the dependence of AFC efficiency on interaction time/length with the modulation front. When the TVM of interest is a bulk medium with length $l \gg \Delta_p$, signal photons traveling through the medium with velocity $v_{g_{signal}}$ can experience the maximum attainable index contrast generated from the nonlinear excitation over Δt_{change} as its propagation time is $t_{prop} = \frac{1}{v_{g\,signal}} \gg \Delta t_{change}$ (for simplicity, here we assume probe signal as impulse function with $v_{g\,signal} \approx v_{change}$) [Fig. 22(c)]. Therefore, theoretically all photons existing in the medium during the modulation event could achieve the maximum frequency shift. The same goes for static signal photons residing within a cavity with a long cavity lifetime. In this case, the resonance of the cavity gets shifted in response to the index perturbation of the cavity and when the shifting happens within a cavity photon lifetime (τ_p), the frequency of the light stored in the microcavity also subsequently changes. However, when

the medium length is considerably less than the pulse length in that medium ($l < \Delta_p$), the signal photons exit the medium before interacting with the full index gradient because of $t_{\text{prop}} < \Delta t_{\text{change}}$ (for cavity when $\tau_p < \Delta t_{\text{change}}$). Therefore, the effective length of the medium experienced by the probe becomes smaller than the spatial extent of the induced change and it leads to a decrease in the maximum achievable frequency shift by a factor of $\frac{t_{\text{prop}}}{\Delta t_{\text{change}}}$.[132] In the limit of thin film, t_{prop} becomes almost negligible and therefore further reduces the interaction between the probe signal.

In this analysis so far, we have not considered free carrier induced non-instantaneous index perturbation which may induce strong index change but at the cost of characteristic long relaxation time ($\tau_{re} > t_p > \Delta t_{\text{change}}$) implying the perturbed index of the medium will take quite longer than Δt_{change} to revert to its original state. It affects the achievable frequency shift with restricted time-width for AFC modulation repeatability. In this regard, one must also consider the free carrier associated absorptive loss in the material which is proportional to the propagation length. It can counteract the effects of lengthened interaction owing to bulk propagation and oppositely benefit the thin film when the TVM is operating in a lossy regime. Also, for thin films, while lowering the group velocity of the probing signal might help to compensate for low interaction time with increased the effective t_{prop}, it simultaneously increases loss owing to low carrier mobility.[132] Furthermore, in reality the probe signal would also have a finite pulse width. Pulse characteristics are important in trajectory-based frequency conversion where excitation and signal pulse train are co or counterpropagating through TVM. In such case, the overall interaction is dependent on the relative input timings, group velocities, temporal overlap and propagation lengths and may lead to interesting effects like self-phase modulation, soliton compression etc.[339,340]

2. Experimental approaches of TVM frequency conversion

After discussing the factors at play for the frequency conversion effect, we shift our focus to the various approaches reported in the literature. Initial efforts to realize TVM-induced optical frequency conversion were implemented with various non-ENZ mediums like photonic crystal cavities[341,342] and waveguides,[343,344] dielectric metasurfaces,[329] and micro resonators.[345,346] In early years of 2000, pioneering works by Yanik *et al.*,[347] Reed *et al.*,[348] and Notomi *et al.*,[342] explored the idea of linear wavelength conversion by dynamic index tuning of optical cavity/resonator in a duration shorter than photon lifetime. Since the intrinsic nonlinearity of these materials is quite low, such photonic approaches typically employed optical resonances with medium-to-high quality (Q) factors (e.g., 10^2–10^5) to increase the photon lifetime (τ_p) which helps to lengthen the photon interaction time with the index modulation. Upon external excitation, the index modulation of the medium shifts the cavity resonance along with rapid phase variation of the confined pulse which leads to the temporal shift of its optical frequency. The frequency-shifted photons ultimately escape the optical cavity and can be measured. Following the theoretical predictions, Preble *et al.*[346] experimentally demonstrated resonance tuning of a Si ring resonator with quality factor >18 000 via optically injected free carriers and achieved a wavelength shift of about 0.25 nm from the initial resonant peak. Later, Tanabe *et al.*[341] also showed short pulse generation as a result of about 50% Q factor detuning of a Si photonic crystal nanocavity under pump influence. To broaden the scope beyond static tuning of trapped light within resonator and enable on-chip devices, dynamic conversion technique was introduced where the modulation is applied to the propagating signal in the waveguide leading to frequency shift up to 0.6 THz.[343,349,350] Overall, while these approaches have used the TVM implementation over a broad spectrum by engineering the structure with desired resonance spectra as well as low power requirements, they incurred several limitations such as weaker index modulation (small $\Delta n/n$) owing to high-index materials (large ε as well as low dispersion)[48] which limits the overall wavelength shift of the resonance to a few tens of nanometers.

In the past decade, ENZ materials (e.g., TCOs) have been used to demonstrate ultrafast nonlinear responses along with near unity index change at sub-picosecond timescales[28,32,39,165] and have been used in several optical metasurfaces[351–353] to explore various TVM implementations.[322,354] Apart from the strong and ultrafast index modulation, operating at ENZ also allows for lower group velocity which can benefit the AFC process by enhancing the interaction. While the slow light condition is also achievable by engineering dispersion with structural schemes (e.g., Bragg grating, ring resonator, waveguide, or photonic crystal),[110,111,355,356] the perks of ENZ medium is that it fulfills the slow light condition inherently without the ordeal of complex fabrication constraints and reduces bulk implementations. To reduce the inevitable carrier-induced loss associated with the ENZ condition, most TCO based TVM experiments have opted for thin film-based implementation.

In recent years, a series of studies performed with ITO and AZO thin films have demonstrated an adiabatic shift of frequency in the range from 1 to 12 THz with a pump-probe setup [Figs. 23(c)–23(e)].[132,323,357–361] They have verified the theory that the magnitude and sign of frequency shift are primarily related to the temporal overlap between the pump and probe (signal) pulse. For intraband excitation as observed in these studies, when the signal arrives after (before) the pump, it experiences a rising (falling) index change in the medium and this leads to redshift (blueshift) of the probe frequency [Figs. 23(a) and 23(b)].[359] To theoretically estimate the shift observed in the experiments, various approaches has been adopted. In one of the early experiments by Shaltout *et al.*,[362] the frequency shift was modeled as the rate of change in phase accumulation of the propagating field through TVM (AZO thin film) while considering the index variation only as function of time (dn/dt) as shown in Eq. (19). While a simple method that captured the essence of the AFS process, this method was incomplete because it neglected the dynamic translation of material dispersion which was significant in the ENZ region. To estimate the hot carrier-induced shift in plasma frequency and resulting nonlinear index change in ENZ as a function of pump intensity, two temperature model (TTM) and hydrodynamic model have been found to be the most comprehensive in explaining the complex nonlinear electrodynamics in ENZ thin films.[363] TTM primarily accounts for the temperature dependence of plasma frequency, while the hydrodynamic model extends this formulation to account for the nonlocal effects (viscosity and pressure of electron gas), time dependent plasma frequency, bound and free electron contribution in nonlinearity along with often ignored surface, magnetic nonlinearities. However, due to the computational complexity of these sophisticated models, they are yet to be explored/developed in the context of TVM for estimating frequency shift. Nevertheless, it is intuitive to understand that ENZ thin

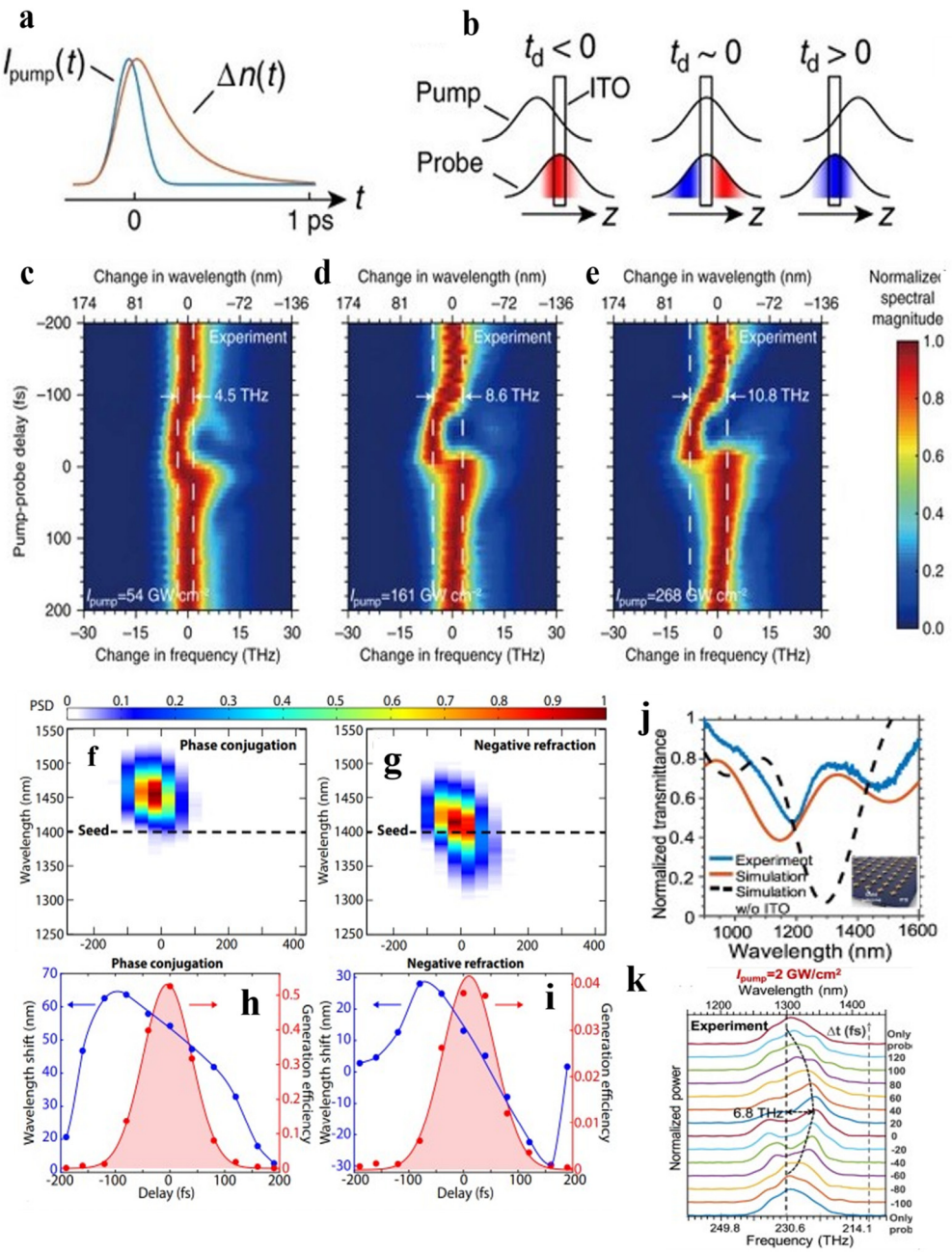

FIG. 23. Frequency conversion process demonstrated in various ENZ based experiments with thin films ITO,[359] AZO,[358] and ITO-gold metasurface.[361] (a) depicts a simplified illustration of the temporal index change $\Delta n(t)$ of ITO excited by a pump pulse. (b) shows the dynamics of pump induced changes observed for the probe in relation to the relative delay between the arrival of two pulses. The frequency of the probe redshifts (blueshifts) if the pump beam lags (leads) the probe. At near-zero delay both redshift and blueshift can occur. Reproduced with permission from Nat. Comm. **11**(1), 2180, (2020). Copyright 2020 Authors, licensed under a Creative Commons Attribution Unported License. (c)–(e) shows the experimental probe spectra as a function of the pump-probe delay time for varying pump intensities where probe wavelength is 1235 nm. The spectral magnitude for each pump-probe delay is normalized individually. For smaller delays near at $t_d \approx 0$, the leading portion of the probe pulse experiences an increase in refractive index (thus redshifts), whereas the trailing portion experiences a decrease in refractive index (thus blueshifts). The magnitude of shifts increases with applied pump intensity as expected. Reproduced with permission from Bruno *et al.*, Appl. Sci. **10**(4), 1318 (2020). Copyright 2020 Authors, licensed under a Creative Commons Attribution Unported License. (f)–(i) A FWM experiment on 500 nm AZO film have shown frequency shifted TR wave in the phase conjugated form along with negative refraction. The shifts are shown in reference to the seed or the signal pulse. (j) and (k) A ITO metasurface based on gold nano-antenna array exhibits frequency shift similar to the ITO film based experiment[359] as shown in (c)–(e) but with much lower excitation intensity because of exploiting the plasmonic antennas for extrinsic enhancement. Reproduced with permission from Pang *et al.*, Nano Lett. **21**(14), 5907–5913 (2021). Copyright 2021 American Chemical Society.

films achieve comparable or enhanced frequency shift compared to other dielectric TVMs even with higher loss and shorter propagation distance due to the presence of strong dispersion ($dn/d\omega$) near ENZ, which naturally allows for a slower group velocity. Hence, Khurgin *et al.*[132] emphasized on the role of this small group velocity in ENZ that contributes to the lengthened interaction time as well as enhanced nonlinearity exhibited in ENZ and expressed the frequency shift based on full derivation of $dn(\omega)/dt$, which is given as

$$\frac{\delta\omega}{\omega} = \frac{1}{\omega}\frac{d}{dt}\phi_{NL} = \frac{\delta n(\omega)}{n_g} \approx \chi^{(3)\prime}\in_0\eta^2 I_{pump}L, \tag{22}$$

where, ϕ_{NL} refers to the nonlinear phase accumulation through propagation, n_g refers to the group index, $\chi^{(3)'}$ represents the time derivative of effective third order susceptibility originating from free carrier induced nonlinearity, η refers to the impedance of the medium, I_{pump} refers to the pump intensity and L is the propagation length over which the index modulation occurs. The approach of this model for estimating the shift observed around ENZ of the AZO film is more comprehensive and precise when compared to the relativistic photon model of Eq. (20) because of the model's consideration of finite dimensional dispersive medium and group velocity of both pump and signal photons.

Along with low group velocity, tuning the incidence angle to access the ENZ or Berremen mode in the thin film can also extrinsically boost the nonlinearity and consequently enhance the temporal interaction within the thin film (see Secs. IV E and IV F).[360,364] In a contemporary study by Bohn *et al.*,[360] of ITO thin film, the incidence angle is found to also provide another degree of freedom by decoupling amplitude modulation that occurs alongside spatiotemporal tuning of the frequency shift. In addition to free carrier induced modulation, parametric processes like four-wave-mixing (FWM) have also been shown to cause broad frequency shift of the mixing generated idler waves. In a degenerate FWM experiment with 500 nm AZO film reported by Bruno *et al.*,[358] an extraordinary shift of about 60 nm has been observed [Figs. 23(f)–23(i)]. A faster nonlinearity along with the added benefit of enhanced absorption and nonlinearity due to operation near ENZ[32,358] partially explains for such large adiabatic shift, although it still calls for further study of the underlying processes.

To enhance the sensitivity of the effective material in response to a pump, often hybrid ENZ approaches with plasmonic metasurface are sought out. The metasurface at resonant conditions extrinsically enhances the nonlinearity, lowering the required energy but at the cost of fast saturation and the bandwidth limited by metasurface design. For example, an experiment with a bare ITO film by Zhou *et al.*,[359] had an energy requirement of ≈58 mJ/cm^2 to obtain a +9% frequency shift which has been shown to reduce 240-fold with the inclusion of plasmonic metasurface to enhance light coupling to a much thinner film [Figs. 23(j) and 23(k)].[361]

Table II enlists some of the pioneering experimental studies that have observed frequency shifts owing to time-varying physics implemented in TCO-based systems. To compare the performance of these approaches, we have adopted the figure of merit (FOM) described by Khurgin *et al.*,[365] in terms of the relative frequency shift ($\frac{\Delta\omega}{\omega}$), the pump intensity ($I_{\text{pump}}$), propagation length (medium thickness, L), which is given as

$$FOM_{AFC} = \frac{\Delta\omega}{\omega I_{pump}L}. \tag{23}$$

In the context of this FOM, ENZ metasurface-based demonstrations outperform thin films because of the low power requirement, as expected. While the insights obtained through the reported experimental studies contribute toward identifying underlying factors to account for the temporal effects observed in ENZ medium from a theoretical perspective, a complete computational model is yet to be developed to simultaneously account for temporal dynamics of electron distribution in response to propagating excitation and the resulting transient optical response. This hinders the understanding of nonlinearities occurring in an ENZ based TVMs. As pointed out by Bohn *et al.*,[360] modeling the complex dynamics between spatiotemporal index profile and temporal shift of frequency and absorption peak is challenging because the present theories describing the hybrid nonlinearities are still in progress. In this effort, Baxter *et al.*[366] have recently reported a FDTD based multiphysics model that uses a TTM to implement the temporal dynamics of the intensity-dependent refractive index, time refraction in transmission and reflection, and the nonlinear

TABLE II. Optical frequency shift observed for experimental studies with TCO operating near ENZ regime. PD is propagation distance; FT is the film thickness.

Device	Type	Shift (THz)	Pump intensity (GW/cm^2)	Pump pulse duration (fs)	Central λ (nm)	PD or FT (nm)	FOM cm/GW	Notes
Subwavelength-thick ITO film[359]	ENZ	−11.1/+3.8	480	120	1235	620	1.54/0.53	Non-resonant, tunable ENZ in 1 μm to 3 μm range
Four-wave mixing in AZO film[358]	ENZ	−55.8	770	105	1400	500	6.77	Degenerate FWM
Subwavelength-thick ITO film[360]	ENZ	−1	400	107	1499	407	0.31	Higher Drude scattering rate in film
Subwavelength thick AZO film[132]	ENZ	−13.8/+2.28	870	115	1285	900	0.76/0.13	Non-degenerate pump/probe
ITO+ gold metasurface[323]	Hybrid ENZ	+1.6	4	60	1240	92	179.88	Self-induced, exhibits spectral compression
ITO + gold meta surface[361]	Hybrid ENZ	−11.2	4	50	1257	63	1863.5	Pump/probe, Broadband 1257 nm to 1404 nm.

response of plasmonic metasurfaces interacting with TCO-based ENZ media by reproducing the associated experiments found in the literature.

3. Time reflection

Apart from the frequency translation and "time-refraction," another interesting physical effect arising from the temporal interface is the formation of a "time-reflected" or "time reversed" (TR) wave. While causality does not allow the TR wave to go back in time, however, it generates a spatially backward propagating time reversed version of the input wave, implying the input's phase evolves backward in time in the TR version (in other words, the temporal order at which the incident wave encounters the time boundary, the order flips for the TR wave generated at the interface). Figure 24(a) shows such an example in water, where the TR wave generated from an originally diverging wave, propagates backward in space to be refocused at the source of the input signal.[299,300] This concept is often linked to negative refraction where the negative index of a medium[367] causes the incoming wave to refract with temporally backward phase evolution, like a TR wave, but in the forward direction. Nonetheless, the retrieval of temporal phase evolution with TVM-induced TR waves has led to explore diverse application scopes like imaging in random media,[308] subwavelength focusing,[368] inverse prisms,[306] temporal antireflection coating,[315] pulse shaping[318] as well as interesting physics like temporal diffraction and interference[319–321] to name a few.

The generation of a TR wave in TVM was predicted in the last century in seminal theories by Morgenthaler,[369] Fante,[370] and others[371,372] investigating the characteristics of EM wave propagating in TVM in which the permittivity or permeability is subject to an abrupt change. The theoretical analysis shows that to maintain the continuity of the EM flux fields ($\vec{D}$ and $\vec{B}$) across the temporal transition/boundary, a reflected wave arises which is a phase conjugated version of the incident wave.[373] In a homogeneous medium for the temporal transition of material property $\left[\epsilon(t),\ \mu(t) \rightarrow \begin{cases} \epsilon_1,\ \mu_1\ at\ t < 0; \\ \epsilon_2,\ \mu_2\ at\ t \geq 0. \end{cases}\right]$ the expression for the wave field before and after time boundary can be given as[369]

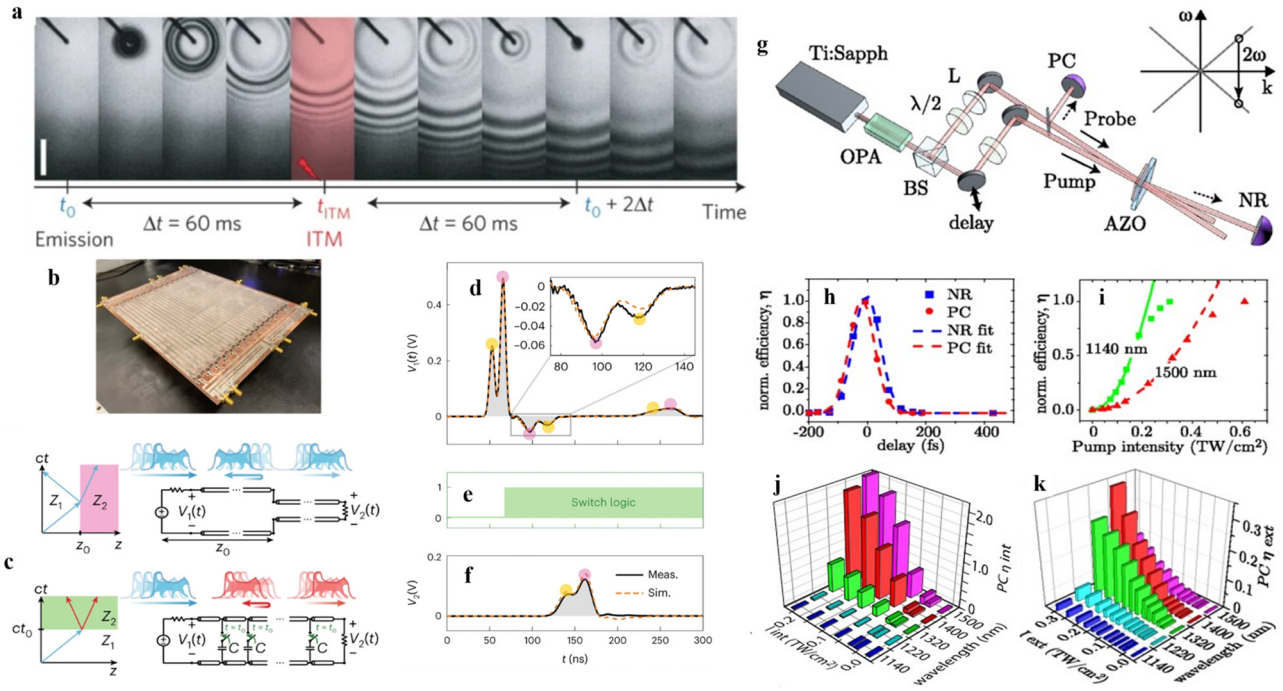

FIG. 24. Demonstrations of TVM induced time reversed wave with (a) water wave,[375] (b)–(f) RF signal in a transmission line metamaterial (TLM),[320] (g)–(k) phase conjugated optical pulse generated from a FWM experiment on ENZ film.[298] (a) shows the image sequence of one of the early TVM experiment with water, at time t_0 a point source creates diverging waves that travel away from the source. After Δt time, the medium experiences a sudden vertical jolt which disrupts the surface wave celerity as an equivalent of index perturbation in TVM. This event generates TR wave the converges back to the source point after $t_0 + 2\Delta t$. Reproduced with permission from Bacot *et al.*, Nat. Phys. **12**(10), 972–977 (2016). Copyright 2016 Springer Nature Group. (b) shows the fabricated TLM circuit where broadband RF signal is injected through one of the ports and when the signal is fully within the microstrip lines of the TLM, the capacitance of the medium is switched with control signal. Illustrations in (c) compare the response of spatial (upper panel) and time (lower panel) interface and show the evolution of the reflected wave in each case. The spatial reflection inverts the signal profile whereas the time reflection does not. Therefore, an observer/receiver located at the input port (V_1) receives the reflected signal in a reversed temporal order compared to the sent version in the case of temporal reflection which is shown as zoomed in (d) (f) shows the time refracted signal obtained at output port (V_2). Reproduced with permission from Moussa *et al.*, Nat. Phys. **19**(6), 863–868 (2023). Copyright 2023 Springer Nature Group. (g) shows the experimental setup of the FWM experiment where the parametric oscillations at 2ω induced by the pump wave causes the signal probe is at ω to transform into both phase-conjugate (PC) and negative-refraction (NR) waves at $-\omega$ frequency, because of thin film phase matching condition. For the same experiment, (h) and (i) shows normalized PC and NR signals as a function of pump-probe time delay and PC at two wavelengths as a function of incident pump intensity respectively. (j) and (k) plots internal and external efficiency of PC for different wavelengths as a function of pump intensity. Reproduced with permission from Vezzoli *et al.*, Phys. Rev. Lett. **120**(4), 043902 (2018). Copyright 2017 American Physical Society.

$$E_1(@t=0^-) = E_0 u(x,y)\exp\left[i\phi(x,y)\right]\exp\left[i(kz-\omega_1 t)\right] + c.c.; \tag{24a}$$

$$\begin{aligned} E_2(@t=0^+) &= E_0 u(x,y)\exp\left[i\phi(x,y)\right]\exp(ikz) \\ &\times \left[T\exp(-i\omega_2 t) + R^*\exp(i\omega_2 t)\right] + c.c. = \ldots \\ &= E_0\exp(-i\omega_2 t)\Big\{Tu(x,y)\exp\left[i\phi(x,y)\right]\exp(ikz) \\ &+ Ru(x,y)\exp\left[-i\phi(x,y)\right]\exp(-ikz)\Big\} + c.c. \end{aligned} \tag{24b}$$

The exponential terms in the above equations include the phase information of the incident (E_1) [Eq. (24a)] and "time refracted/reflected" (E_2) fields [Eq. (24b)]. Here the assumption is that the abrupt change in permittivity occurs uniformly through the entire space occupied by the wave, resulting in a constant wavevector (k) and frequency conversion ($\omega_1 = \frac{ck}{\sqrt{\epsilon_1}}$ at $t<0 \rightarrow \omega_2 = \frac{ck}{\sqrt{\epsilon_2}}$ at $t \geq 0$). The field after the temporal transition [Eq. (24b)] includes the refracted and reflected fields with oppositely signed frequency components (ω_2) corresponding to a time reversal. The negative frequency of the reflected field can also be interpreted as a positive frequency wave propagating in the backward direction by expanding into the complex conjugate terms ($k, \omega \rightarrow -k, \omega$). The expanded terms in Eq. (24b) thus show that while the transmitted field travels in the same direction as the incident field ($+k$), the conjugated phase term in the reflected wave $\left[\exp(-ikz)\right]$ causes it to travel in opposite direction ($-k$) with a π phase shift. The coefficients of transmissivity T and reflectivity R* can be deduced from the continuity condition, $B = \mu_1 H_1 = \mu_2 H_2$ and $D = \epsilon_1 E_1 = \epsilon_2 E_2$ at temporal boundary (t = 0) and expressed as

$$T = \frac{1}{2}\left(\frac{\epsilon_1}{\epsilon_2} + \sqrt{\frac{\mu_1\epsilon_1}{\mu_2\epsilon_2}}\right); \tag{25a}$$

$$R^* = \frac{1}{2}\left(\frac{\epsilon_1}{\epsilon_2} - \sqrt{\frac{\mu_1\epsilon_1}{\mu_2\epsilon_2}}\right). \tag{25b}$$

Interestingly, Eq. (25b) for the conjugate reflectivity coefficient also shows that for invariant impedance across the temporal boundary ($\sqrt{\frac{\mu_1}{\epsilon_1}} = \sqrt{\frac{\mu_2}{\epsilon_2}}$), there will be no reflected wave. However, the derivations here assume the ideal scenario of an abrupt change which is challenging to realize practically. For substantial TR detection from TVM, modulation of the medium's index needs to happen in a timescale less than the signal's oscillation period, implying a constraint of $\Delta t_{\text{change}} \leq 2\pi/\omega_1$.[373] Furthermore, such fast and uniformly strong modulation of the material property have substantial energy requirements.[374] These challenges have led early demonstrations of time reversal to exploit the holographic principle with emitter-receptor antennas where forward propagating waves are digitally sampled, stored, and transformed to re-emit in a time reversed manner, resulting in backward propagating TR wave.[375] Such an approach has been implemented with waves in the low frequency regime such as water waves,[375] acoustics,[376] and radio frequency (RF).[320] Only in the last decade, the first experimental demonstration of time interface induced TR wave in water has been reported in a seminal work by Bacot *et al.*,[375] where sudden perturbation of the surface wave propagation causes the generation of TR wave that refocused at the source [see Fig. 24(a)]. Very recently, Moussa *et al.*,[320] reported observation of TR of RF wave (30–60 MHz) by inducing temporal interface in a transmission line metamaterial medium [see Figs. 24(b)–24(f)]. In this work, a time boundary has been achieved innovatively by connecting external reactance to the TLM via a series of switches within a time faster than the signal period (≈30 ns) rather than temporal modulation of reactance. The work also explored the wave-interference effects resulting from the application of multiple time interfaces (effectively forming a temporal slab where a perturbed medium is modulated again to revert to its original condition). However, the realization of time-reversal in the optical range has remained elusive to date.

Although optical modulation of the medium uniformly at fs timescale is difficult to achieve, there is an alternative approach of realizing wave-front reversal through phase conjugation by means of nonlinear parametric processes like degenerate FWM.[377–380] Here, parametric oscillations at 2ω induced by the pump wave cause the signal probe at ω to transform into both phase-conjugated (PC) and negatively refracted (NR) waves at $-\omega$ frequency, as a consequence of thin film phase matching condition.[381] Building on Pendry's proposed scheme to realize a perfect lens combining the conventional TR and NR wave[300] using this method, Vezzoli *et al.*[298] implemented the experimental setup of the FWM in an ENZ medium to realize the time reversal of the carrier wave of the signal pulse with the added benefit of strong ENZ induced nonlinearity [Figs. 24(g)–24(k)]. The generation of both TR and NR waves in FWM process can be also explained by the concept of holography.[377] In this regard, the signal and pump wave act as the object and reference wave, respectively, and their interference creates a dynamic hologram through the index modulation leading to the reconstruction of a PC wave as an image of the object wave as well as a conjugate image or NR wave when read by the "reference" pump. The generation of NR wave in this case is favored by relaxed phase matching condition enabled by short propagation distance. While the AZO film used in this experiment is optically thick (500 nm), yet the ENZ condition of the film relaxes the phase-matching condition in propagation direction, thereby enabling the film to act as time-reversing surface.

Recently, there has been an increasing interest in realizing a theoretical concept named "photonic time crystal" (PTC) which involves manifesting the interference effects arising from multiple time boundary induced TR waves. In Sec. VII B 4, we will briefly introduce PTC and discuss the recent development toward ENZ based implementation of this TR application.

4. Photonic time crystal

So far, our discussion has been focused on the optical time varying effects arising from light's interaction with a single temporal boundary or moving spatial boundary which can be explained considering the spatially equivalent effects in many aspects. This striking analogy extends similarly for light propagating in periodic temporal boundaries, which can lead to unique properties like momentum gap generation (temporal equivalent of energy gap formed in photonic crystal[382]) via interference between multiple time-reflected and time-refracted waves.[383] Such media that experiences abrupt change of its dielectric properties via periodic external temporal modulation is referred to as PTC[383–385] and it holds the key to achieving tunable and enhanced spontaneous emission from free electron/quantum emitters owing to the momentum gap [Fig. 25(a)].[383] It is important to note that the concept of PTC is fundamentally different than that of a "time

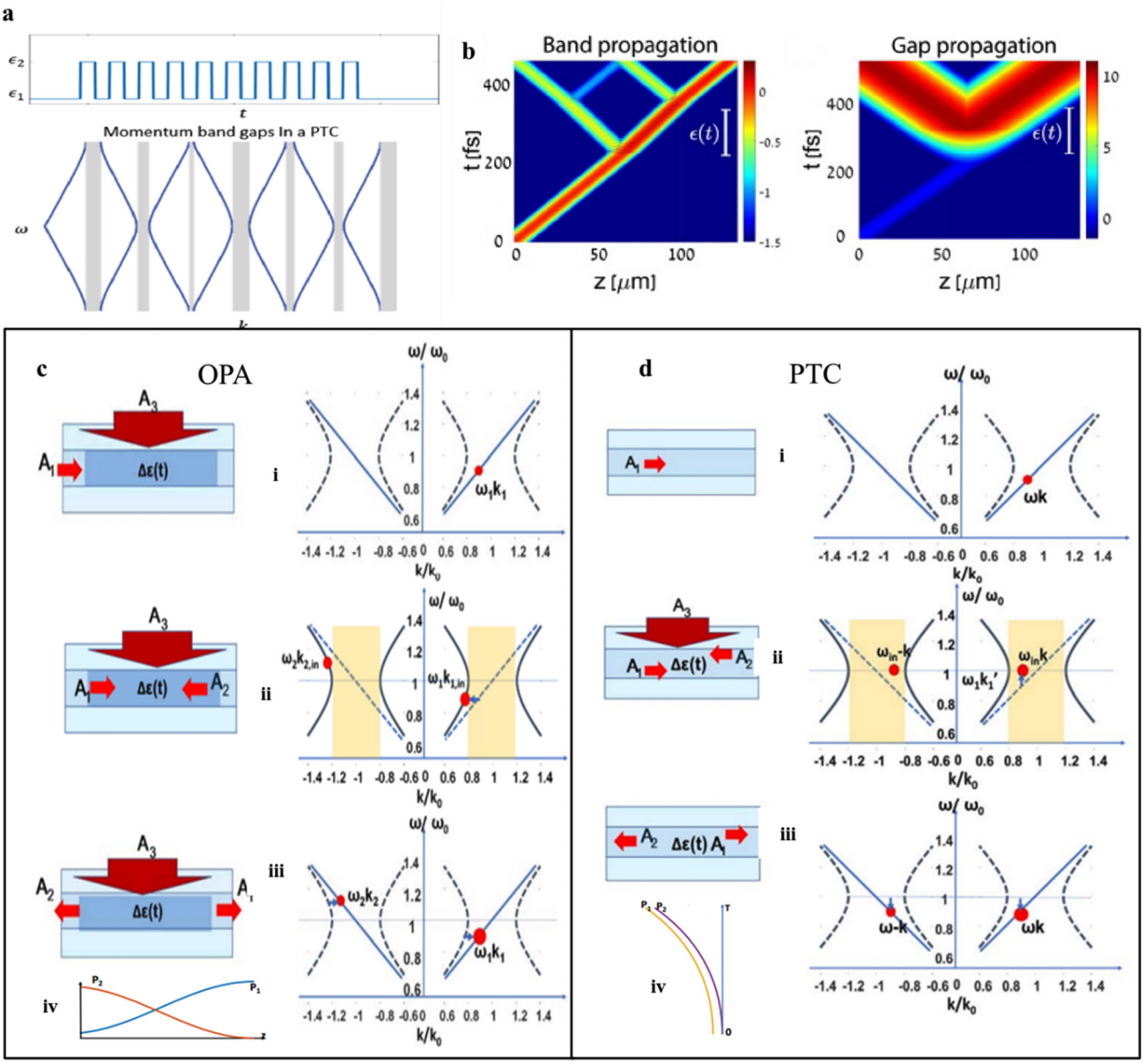

FIG. 25. Dispersion dynamics of PTC. (a) depicts the periodic modulation of medium permittivity and corresponding typical band diagram in the PTC. The gray shaded regions refer to the momentum bandgap in analogy with energy bandgap formed in photonic crystals.[385] Reproduced with permission from Lustig *et al.*, Opt. Express **31**(6), 9165–9170 (2023). Copyright 2023 Optical Society of America. (b) Pulse propagation modes in PTC for when the pulse momentum is within the allowed band (Band propagation) and in the bandgap (Gap propagation).[385] (c) and (d) The sequential change in momentum and frequency for light propagating through the time modulated medium has been shown for OPA and PTC respectively.[365] For OPA arrangement, (c-i) before light enters the modulated zone, it follows the linear dispersion (ω,k) (dashed line) corresponding to the unmodulated medium, (c-ii) when it enters the medium, boundary condition requires energy or frequency conservation alongside generation of counterpropagating idler. Since the change of momentum is allowed, new wavevectors ($k_{1_{in}}$, k_{2in}) only follow the dispersion curve of allowed momentums and "pushed" out of the bandgap in the momentum space if new wavevectors correspond to any values within it. (c-iii) Once the signal and idler photons leave the spatial boundary of the modulated region, wavevectors revert to the values corresponding to unmodulated region. (c-iv) The spatial distribution of signal (P_1)and idler (P_2) intensity indicating amplification of both along their respective propagation direction. For PTC arrangement, (d-i) signal is inside the nonlinear modulation region before modulation starts. (d-ii) When modulation starts, in response to the sudden change of the medium and restriction to conserve momentum, signal changes to a new complex frequency value along with generation of counterpropagating idler while preserving the wavevector. In this case, even if the wavevector falls within the bandgap (shaded) zone, corresponding frequency values are still accessible by the wave within the limits of time modulation period. (d-iii) When time modulation stops, the signal and idler frequencies revert to original frequency. (d-iv) Since the new frequencies within the modulation period can be of complex value, the imaginary frequency components lead to exponential growth of signal and idler in time. Reproduced with permission from J. B. Khurgin, "Photonic time crystals and parametric amplification: Similarity and distinction," arXiv:2305.15243 (2023). Copyright 2023 Authors, licensed under a Creative Commons Attribution Unported License.

crystal" where the system exhibits spontaneous periodic oscillations over time due to many body quantum interactions.[386]

Theoretically, a pulse within the PTC can experience energy amplification only when its momentum falls within the associated gap otherwise it will propagate through PTC by twice-splitting into time reversed-refracted modes, as shown in Fig. 25(b). The interesting features associated with the momentum gap in PTC occur due to the existence of two Floquet modes of complex frequency that can evolve forward in time directed by causality and one of these modes may lead to exponential amplification during the modulation cycle depending on the state of different topological phases between two adjacent PTCs.[387] However, the amplified gap mode has zero group velocity implying propagation is prohibited as long as the PTC modulation is occurring [Fig. 25(b)]. The amplification in a PTC is often compared to the parametric gain observed in conventional nonlinear optical parametric amplifiers (OPA).[48] In this effort, an analytical derivation by Khurgin *et al.*[365] regarding the nonlinear polarization for both PTC and OPA process reveals the presence of similar dispersion characteristics with momentum bandgap in the nonlinear material being modulated at a frequency twice the signal frequency as shown in Figs. 25(c) and 25(d). Fundamentally, propagation is prohibited for any pulse associated with gap momentum irrespective of OPA/PTC system. However, an OPA allows momentum change while conserving frequency, and for PTC opposite is true. Therefore, in OPA, a restricted pulse with gap momentum can convert to a propagating mode with 'allowed' momentum adhering to the dispersion [Fig. 25(c)]. In the case of PTC, such a restricted pulse can retain its gap momentum and continue to exist with complex frequencies until PTC ends [Fig. 25(d)]. Such distinctive boundary conditions for each process leads to the oscillatory character of propagation in the generated idler signal vs exponential growth of the time boundary generated TR waves in PTC.[365] Further details of PTC dynamics can be found in the following works.[383,385,387–389]

While the realization of PTC in the optical range is yet to be demonstrated, owing to relaxed modulation period constraint for longer wavelength, PTC-dominated effects such as the exponential growth of EM waves in a temporally varying metasurface, has been demonstrated in the microwave regime.[390] Furthermore, the advancements in ultrafast laser technology along with high damage threshold of TCOs has enabled demonstration of index modulation within a single cycle,[391] a noteworthy progress toward PTC realization. Despite such promising development, one should keep in mind that such fast modulation requires power density on the order of tens of TW/cm^3 to observe a PTC with moderately wide momentum gap. Thus, the observation of PTC effects ultimately depends on the material's capacity to withstand the maximum absorbed energy, as it limits the maximum possible duration of the periodic temporal modulation and the resulting momentum bandgap-widths.[374] Therefore, alongside ultrafast modulation schemes, damage threshold of materials needs to be considered.[327]

Overall, all-optically induced ultrafast and enhanced nonlinearities of ENZ TCOs have been a promising medium to observe time-varying effects, such as frequency shifting and time-reflection, at optical frequencies. However, the enormous energy requirements to create appreciable index contrast and saturation of index modulation due to slow relaxation times are major challenges. The continued quest for new materials solutions as well as exploring index modulation schemes such as two-color pumping,[129] and interband excitations for steeper temporal index contrast may also pave the way to finding the desired breakthrough in ENZ-based TVM research efforts.

VII. CONCLUSION

Over the last decade, nonlinear optical interactions in epsilon-near-zero and related vanishing property materials have been a key area of inquiry within the fields of nanophotonics and nonlinear optics. By making use of well-established materials (namely, the transparent conducting oxides), enhancements to a wide range of nonlinear processes have been demonstrated, headlined by the ability to provide near-unity index modulation on a sub-picosecond timescale. Since early demonstrations, largely led by experimental efforts, work has sought to unravel the reasoning for the improved nonlinearities leading to an improved understanding of the foundations and origins of the effects while experimental efforts employed well-known tools of structural dispersion and extrinsic enhancements to push the efficiency of nonlinearities further.

From these efforts, we now have a good picture of what ENZ nonlinearities can provide and what their limitations are. As highlighted in this review, the primary advances enabled by ENZ are the simultaneous and automatic ability to use real transitions, which improve the intrinsic nonlinearity of the material, alongside slow light and confinement, which add an extrinsic enhancement factor to the overall nonlinear response. For virtual nonlinear processes such as wave mixing, intrinsic nonlinearities are found to be comparable to other leading semiconductor compounds, while slow light effects of ENZ provide an order of magnitude improvement [e.g., $\chi^{(3)} \approx 3.5 \times 10^{-18}$ m^2 V^{-2} for ITO, and $\chi^{(3)} \approx 1.5 \times 10^{-20}$ m^2 V^{-2} for undoped ZnO]. For real nonlinear processes, such as the intensity dependent index, the result is a four to five order of magnitude leap compared to virtual nonlinear processes in wide-bandgap semiconductors and a one to two order of magnitude increase in the nonlinearity when compared to similar real processes in non-ENZ materials such as Si and GaAs. Thus, when compared to materials/processes of a similar class ENZ is observed to provide a moderate enhancement to the nonlinearity for both virtual and real processes. The "secret sauce" of the common ENZ compounds is that they are readily available, are well understood due to their wide-spread industrial use (films of ITO that provide ENZ enhancement at a wavelength around 1200 nm can be commercially purchased), as well as exhibit extreme damage thresholds exceeding of 1 TWcm^{-2}.

While ENZ materials effect is useful and relatively broadband, the primary price paid for employing the ENZ effect today is introduction of optical loss—skin depths in common compounds in the ENZ region are on the order of 0.5–1 μm. As a result, it remains challenging to scale ENZ effects to improve absolute efficiencies, and thermal dissipation remains an open problem for the oft-mentioned high-speed operation of ENZ materials that will need to be addressed as applications as explored. Moreover, the properties of many of the commonly studied ENZ compounds are already near their optimal values, leaving little room to improve the nonlinearity without shifting to new spectral regions. To combat this, various techniques have been employed utilizing nanostructuring and excitation to push ENZ effects into new spectral regions, to engineer loss[216] and to optimize extrinsic enhancements, but these approaches typically have tradeoffs, such as a narrow operating spectrum, lower damage threshold, or slower

response, the limitations of which must be considered based on the intended application.

Within this view, we can summarize a few key points and questions that we believe are of interest to the optics community in the coming years:

(1) Interband effects in common ENZ films remain an area where improved modeling is needed to accurately describe band edge effects with free carrier effects and match experiments.
(2) Short pulse (sub 10 fs) interactions in ENZ materials are an emerging area of study with little theoretical backing.
(3) What are the limits in operating speed of ENZ effects imposed by thermal dissipation?
(4) Can new materials, tailored for ENZ nonlinearities, provide an improved compromise between efficiency and loss?
(5) Can the efficiencies of various processes be improved to a level that would facilitate the combination of ENZ with compact sources such as fiber lasers or diodes?
(6) Can the nonlinearity in ENZ films impact current or emerging applications of interest?

It is ultimately this final point which is perhaps the most important question to be addressed. Clearly, ENZ materials provide unique traits and are widely available from commercial vendors. As such, they are likely to remain a consistent operator in academic exercises while the ability to support quite extreme pumping scenarios allows them to serve as a testbed to explore light-matter interactions and any number of emerging optical processes—such as the space-time effects highlighted here. What is not yet clear is if the limitations of ENZ materials will ultimately outweigh their benefits. As the community continues to study nonlinear ENZ effects, expanding to new materials and focusing on key applications, we look forward to seeing many of these questions answered.

SUPPLEMENTARY MATERIAL

See the supplementary material for details (a) n_{2eff} coefficients of epsilon-near-zero materials, with associated experimental parameters, (b) UV index change calculation details, and (c) IR index change calculation details.

ACKNOWLEDGMENTS

Dr. Nathaniel Kinsey acknowledges the Air Force Office of Scientific Research (Nos. FA9550-1-18-0151 and FA9550-16-10362). Dr. Henri Lezec and Dr. Dhruv Fomra also acknowledge support under the Professional Research Experience Program (PREP), administered through the Department of Chemistry and Biochemistry, University of Maryland. Research performed in part at the National Institute of Standards and Technology Center for Nanoscale Science and Technology. The views and conclusions are those of the authors and should not be interpreted as representing the official policies of the funding agency.

This work was supported by the Air Force Office of Scientific Research (Nos. FA9550-1-18-0151, FA9550-16-10362, and FA9550-22-1-0383) and National Science Foundation (Nos. 1808928 and 2322891).

Certain equipment, instruments, software, or materials, commercial or noncommercial, are identified in this paper in order to specify the experimental procedure adequately. Such identification is not intended to imply recommendation or endorsement of any product or service by NIST, nor is it intended to imply that the materials or equipment identified are necessarily the best available for the purpose.

AUTHOR DECLARATIONS

Conflict of Interest

The authors have no conflicts to disclose.

Author Contributions

Dhruv Fomra: Conceptualization (equal); Data curation (equal); Formal analysis (equal); Writing – original draft (equal); Writing – review & editing (equal). **Adam Ball:** Data curation (equal); Formal analysis (equal); Writing – original draft (equal); Writing – review & editing (equal). **Samprity Saha:** Data curation (equal); Writing – original draft (equal); Writing – review & editing (supporting). **Jingwei Wu:** Writing – original draft (supporting). **Md. Ariful Hoque Sojib:** Writing – original draft (supporting). **Amit Agrawal:** Writing – review & editing (equal). **Henri J. Lezec:** Writing – review & editing (equal). **Nathaniel Kinsey:** Writing – review & editing (equal).

DATA AVAILABILITY

The data that support the findings of this study are available from the corresponding author upon reasonable request.

REFERENCES

[1]S. A. Maier, *Plasmonics: Fundamentals and Applications* (Springer, 2007).
[2]A. A. Maradudin, J. R. Sambles, and W. Barnes, *Modern Plasmonics* (Elsevier, 2014).
[3]D. K. Gramotnev and S. I. Bozhevolnyi, "Plasmonics beyond the diffraction limit," Nat. Photonics **4**(2), 83–91 (2010).
[4]W. Cai and V. Shalaev, *Optical Metamaterials: Fundamentals and Applications* (Springer, New York, 2010).
[5]W. Cai, U. K. Chettiar, A. V. Kildishev, and V. M. Shalaev, "Optical cloaking with metamaterials," Nat. Photonics **1**(4), 224–227 (2007).
[6]N. I. Zheludev and Y. S. Kivshar, "From metamaterials to metadevices," Nat. Mater. **11**(11), 917–924 (2012).
[7]D. R. Smith, J. B. Pendry, and M. C. K. Wiltshire, "Metamaterials and negative refractive index," Science **305**(5685), 788–792 (2004).
[8]A. V. Kildishev, A. K. Sarychev, H.-K. Yuan, U. K. Chettiar, V. M. Shalaev, V. P. Drachev, and W. Cai, "Negative index of refraction in optical metamaterials," Opt. Lett. **30**(24), 3356–3358 (2005).
[9]J. D. Joannopoulos, S. G. Johnson, J. N. Winn, and R. D. Meade, *Photonic Crystals: Molding the Flow of Light* (Princeton University Press, 2011).
[10]T. Baba, "Slow light in photonic crystals," Nat. Photonics **2**(8), 465–473 (2008).
[11]I. Liberal and N. Engheta, "Near-zero refractive index photonics," Nat. Photonics **11**(3), 149–158 (2017).
[12]R. A. Shelby, D. R. Smith, and S. Schultz, "Experimental verification of a negative index of refraction," Science **292**(5514), 77–79 (2001).
[13]J. B. Pendry, "Negative refraction makes a perfect lens," Phys. Rev. Lett. **85**(18), 3966 (2000).
[14]A. Poddubny, I. Iorsh, P. Belov, and Y. Kivshar, "Hyperbolic metamaterials," Nat. Photonics **7**(12), 948–957 (2013).
[15]C. T. Riley, J. S. T. Smalley, K. W. Post, D. N. Basov, Y. Fainman, D. Wang, Z. Liu, and D. J. Sirbuly, "High-quality, ultraconformal aluminum-doped zinc oxide nanoplasmonic and hyperbolic metamaterials," Small **12**(7), 892–901 (2016).
[16]D. Schurig, J. J. Mock, B. J. Justice, S. A. Cummer, J. B. Pendry, A. F. Starr, and D. R. Smith, "Metamaterial electromagnetic cloak at microwave frequencies," Science **314**(5801), 977–980 (2006).

[17]D. L. Sounas, R. Fleury, and A. Alù, "Unidirectional cloaking based on metasurfaces with balanced loss and gain," Phys. Rev. Appl. **4**(1), 014005 (2015).
[18]N. Kinsey, C. DeVault, A. Boltasseva, and V. M. Shalaev, "Near-zero-index materials for photonics," Nat. Rev. Mater. **4**(12), 742–760 (2019).
[19]J. Brown, "Artificial dielectrics having refractive indices less than unity," Proc. IEE-Part III **100**(67), 319–320 (1953).
[20]A. Alù, M. G. Silveirinha, A. Salandrino, and N. Engheta, "Epsilon-near-zero metamaterials and electromagnetic sources: Tailoring the radiation phase pattern," Phys. Rev. B **75**(15), 155410 (2007).
[21]N. Garcia, E. V. Ponizovskaya, and J. Q. Xiao, "Zero permittivity materials: Band gaps at the visible," Appl. Phys. Lett. **80**(7), 1120–1122 (2002).
[22]S. Enoch, G. Tayeb, P. Sabouroux, N. Guérin, and P. Vincent, "A metamaterial for directive emission," Phys. Rev. Lett. **89**(21), 213902 (2002).
[23]M. Silveirinha and N. Engheta, "Tunneling of electromagnetic energy through subwavelength channels and bends using ε-near-zero materials," Phys. Rev. Lett. **97**(15), 157403 (2006).
[24]M. G. Silveirinha and N. Engheta, "Theory of supercoupling, squeezing wave energy, and field confinement in narrow channels and tight bends using ε near-zero metamaterials," Phys. Rev. B **76**(24), 245109 (2007).
[25]R. W. Ziolkowski, "Propagation in and scattering from a matched metamaterial having a zero index of refraction," Phys. Rev. E **70**(4), 046608 (2004).
[26]C. Devault, V. A. Zenin, A. Pors, J. Kim, K. Chaudhuri, S. Bozhevolnyi, V. M. Shalaev, and A. Boltasseva, "Plasmonic antenna resonance pinning and suppression of near-field coupling from epsilon-near-zero substrate," in Conference on Lasers and Electro-Optics (CLEO), 2017.
[27]D. A. Powell, A. Alù, B. Edwards, A. Vakil, Y. S. Kivshar, and N. Engheta, "Nonlinear control of tunneling through an epsilon-near-zero channel," Phys. Rev. B **79**(24), 245135 (2009).
[28]N. Kinsey, C. DeVault, J. Kim, M. Ferrera, V. M. Shalaev, and A. Boltasseva, "Epsilon-near-zero Al-doped ZnO for ultrafast switching at telecom wavelengths," Optica **2**(7), 616 (2015).
[29]O. Reshef, I. De Leon, M. Z. Alam, and R. W. Boyd, "Nonlinear optical effects in epsilon-near-zero media," Nat. Rev. Mater. **4**(8), 535–551 (2019).
[30]S. Krastanov, M. Heuck, J. H. Shapiro, P. Narang, D. R. Englund, and K. Jacobs, "Room-temperature photonic logical qubits via second-order nonlinearities," Nat. Commun. **12**(1), 191 (2021).
[31]I. Liberal and N. Engheta, "Zero-index structures as an alternative platform for quantum optics," Proc. Natl. Acad. Sci. U. S. A. **114**(5), 822–827 (2017).
[32]L. Caspani, R. P. M. Kaipurath, M. Clerici, M. Ferrera, T. Roger, M. Pietrzyk, A. Di Falco, J. Kim, N. Kinsey, V. M. Shalaev, A. Boltasseva, and D. Faccio, "Enhanced nonlinear refractive index in ε-near-zero materials," Phys. Rev. Lett. **116**, 233901 (2016).
[33]Y. Yang, J. Lu, A. Manjavacas, T. S. Luk, H. Liu, K. Kelley, J. P. Maria, E. L. Runnerstrom, M. B. Sinclair, S. Ghimire, and I. Brener, "High-harmonic generation from an epsilon-near-zero material," Nat. Phys. **15**(10), 1022–1026 (2019).
[34]H. Suchowski, K. O'Brien, Z. J. Wong, A. Salandrino, X. Yin, and X. Zhang, "Phase mismatch-free nonlinear propagation in optical zero-index materials," Science **342**(6163), 1223–1226 (2013).
[35]J. R. Gagnon, O. Reshef, D. H. G. Espinosa, M. Z. Alam, D. I. Vulis, E. N. Knall, J. Upham, Y. Li, K. Dolgaleva, E. Mazur, R. W. Boyd *et al.*, "Relaxed phase-matching constraints in zero-index waveguides," Phys. Rev. Lett. **128**(2039), 203902 (2022).
[36]A. Ball, D. Fomra, N. Kinsey, and J. B. Khurgin, in *Advances in Nonlinear Photonics* (Elsevier, 2023), pp. 319–348.
[37]M. A. Vincenti, D. De Ceglia, A. Ciattoni, and M. Scalora, "Singularity-driven second- and third-harmonic generation at ε-near-zero crossing points," Phys. Rev. A **84**(6), 063826 (2011).
[38]A. Ciattoni, C. Rizza, and E. Palange, "Extreme nonlinear electrodynamics in metamaterials with very small linear dielectric permittivity," Phys. Rev. A **81**(4), 043839 (2010).
[39]M. Z. Alam, I. De Leon, and R. W. Boyd, "Large optical nonlinearity of indium tin oxide in its epsilon-near-zero region," Science **352**(6287), 795–797 (2016).
[40]R. Secondo, J. Khurgin, and N. Kinsey, "Absorptive loss and band nonparabolicity as a physical origin of large nonlinearity in epsilon-near-zero materials," Opt. Mater. Express **10**(7), 1545 (2020).
[41]I.-W. Un, S. Sarkar, and Y. Sivan, "Electronic-based model of the optical nonlinearity of low-electron-density Drude materials," Phys. Rev. Appl. **19**, 044043 (2023).
[42]H. Ghobadi, H. L. Offerhaus, J. A. Alvarez-Chavez, M. Morales-Masis, and I. De Leon, "Understanding the conditions for the optimum nonlinear refraction of epsilon-near-zero films based on transparent conducting oxides," Opt. Express **31**(5), 8775 (2023).
[43]E. Minerbi, S. Sideris, J. B. Khurgin, and T. Ellenbogen, "The role of epsilon near zero and hot electrons in enhanced dynamic THz emission from nonlinear metasurfaces," Nano Lett. **22**(15), 6194–6199 (2022).
[44]M. Z. Alam, S. A. Schulz, J. Upham, I. De Leon, and R. W. Boyd, "Large optical nonlinearity of nanoantennas coupled to an epsilon-near-zero material," Nat. Photonics **12**(2), 79–83 (2018).
[45]Y. Meng, Q. Liu, R. Wang, F. Hu, and M. Gong, "High-contrast optical bistability using a subwavelength epsilon-near-zero material," Opt. Lett. **48**(6), 1371–1374 (2023).
[46]S. Benis, P. Zhao, D. J. Hagan, and E. W. Van Stryland, in *Nonlinear Optics* (OSA, Washington, D.C., 2017).
[47]B. T. Diroll, P. Guo, R. P. H. Chang, and R. D. Schaller, "Large transient optical modulation of epsilon-near-zero colloidal nanocrystals," ACS Nano **10**(11), 10099–10105 (2016).
[48]R. W. Boyd, *Nonlinear Optics* (Elsevier Inc., 2008).
[49]Y. R. Shren, *The Principles of Nonlinear Optics*, 1st ed. (Wiley-Interscience, 1984).
[50]J. B. Khurgin, "Nonlinear optics from the viewpoint of interaction time," Nat. Photonics **17**, 545–551 (2023).
[51]N. Shibata, T. Seki, G. Sánchez-Santolino, S. D. Findlay, Y. Kohno, T. Matsumoto, R. Ishikawa, and Y. Ikuhara, "Electric field imaging of single atoms," Nat. Commun. **8**(1), 15631 (2017).
[52]W. Nie, "Optical nonlinearity: Phenomena, applications, and materials," Adv. Mater. **5**(7–8), 520–545 (1993).
[53]D. E. Chang, V. Vuletić, and M. D. Lukin, "Quantum nonlinear optics—Photon by photon," Nat. Photonics **8**(9), 685–694 (2014).
[54]D. V. Strekalov, C. Marquardt, A. B. Matsko, H. G. L. Schwefel, and G. Leuchs, "Nonlinear and quantum optics with whispering gallery resonators," J. Opt. **18**(12), 123002 (2016).
[55]T. Peyronel, O. Firstenberg, Q. Y. Liang, S. Hofferberth, A. V. Gorshkov, T. Pohl, M. D. Lukin, and V. Vuletić, "Quantum nonlinear optics with single photons enabled by strongly interacting atoms," Nature **488**(7409), 57–60 (2012).
[56]N. Kinsey and J. Khurgin, "Nonlinear epsilon-near-zero materials explained: Opinion," Opt. Mater. Express **9**(7), 2793 (2019).
[57]C. M. Cirloganu, N. Cox, M. Reichert, D. J. Hagan, G. Nootz, L. A. Padilha, H. Hu, S. Benis, D. Peceli, M. Woodall, T. Ensley, P. D. Olszak, E. W. Van Stryland, and S. Webster, "Three-photon absorption spectra and bandgap scaling in direct-gap semiconductors," Optica **7**(8), 888–899 (2020).
[58]J. B. Khurgin, M. Clerici, and N. Kinsey, "Fast and slow nonlinearities in epsilon-near-zero materials," Laser Photon Rev. **15**(2), 2000291 (2021).
[59]A. Pasquazi, M. Peccianti, L. Razzari, D. J. Moss, S. Coen, M. Erkintalo, Y. K. Chembo, T. Hansson, S. Wabnitz, P. Del'Haye, X. Xue, A. M. Weiner, and R. Morandotti, "Micro-combs: A novel generation of optical sources," Phys. Rep. **729**, 1–81 (2018).
[60]A. J. Metcalf, B. Niu, Y. Xuan, A. M. Weiner, L. Fan, M. Teng, J. A. Jaramillo-Villegas, X. Xue, C. Wang, D. E. Leaird, J. Wang, Y. Liu, A. Al Noman, K. Han, Y. J. Lee, P.-H. Wang, L. T. Varghese, S. Kim, and M. Qi, "High-Q silicon nitride microresonators exhibiting low-power frequency comb initiation," Optica **3**(11), 1171–1180 (2016).
[61]X. Ji, F. A. S. Barbosa, S. P. Roberts, A. Dutt, J. Cardenas, Y. Okawachi, A. Bryant, A. L. Gaeta, and M. Lipson, "Ultra-low-loss on-chip resonators with sub-milliwatt parametric oscillation threshold," Optica **4**(6), 619 (2017).
[62]A. L. Gaeta, M. Lipson, and T. J. Kippenberg, "Photonic-chip-based frequency combs," Nat. Photonics **13**(3), 158–169 (2019).
[63]S.-Y. Lin, V. M. Hietala, L. Wang, and E. D. Jones, "Highly dispersive photonic band-gap prism," Opt. Lett. **21**(21), 1771–1773 (1996).
[64]A. Imhof, W. L. Vos, R. Sprik, and A. Lagendijk, "Large dispersive effects near the band edges of photonic crystals," Phys. Rev. Lett. **83**, 2942–2945 (1999).

[65]F. Marquier, J.-J. Greffet, J.-P. Hugonin, and S. Vassant, "Berreman mode and epsilon near zero mode," Opt. Express **20**(21), 23971–23977 (2012).
[66]W. D. Newman, C. L. Cortes, J. Atkinson, S. Pramanik, R. G. Decorby, and Z. Jacob, "Ferrell–Berreman modes in plasmonic epsilon-near-zero media," ACS Photonics **2**(1), 2–7 (2015).
[67]M. F. Limonov, M. V. Rybin, A. N. Poddubny, and Y. S. Kivshar, "Fano resonances in photonics," Nat. Photonics **11**(9), 543–554 (2017).
[68]M. G. Wood, S. Campione, S. Parameswaran, T. S. Luk, J. R. Wendt, D. K. Serkland, and G. A. Keeler, "Gigahertz speed operation of epsilon-near-zero silicon photonic modulators," Optica **5**(3), 233 (2018).
[69]A. Anopchenko, S. Gurung, S. Bej, and H. W. H. Lee, "Field enhancement of epsilon-near-zero modes in realistic ultrathin absorbing films," Nanophotonics **12**(14), 2913–2920 (2023).
[70]J. Deng, Y. Tang, S. Chen, K. Li, A. V. Zayats, and G. Li, "Giant enhancement of second-order nonlinearity of epsilon-near-zero medium by a plasmonic metasurface," Nano Lett. **20**(7), 5421–5427 (2020).
[71]D. Smirnova, D. Leykam, Y. Chong, and Y. Kivshar, "Nonlinear topological photonics," Appl. Phys. Rev. **7**, 021306 (2020).
[72]G. Grinblat, Y. Li, M. P. Nielsen, R. F. Oulton, and S. A. Maier, "Efficient third harmonic generation and nonlinear subwavelength imaging at a higher-order anapole mode in a single germanium nanodisk," ACS Nano **11**, 953 (2017).
[73]L. Carletti, K. Koshelev, C. De Angelis, and Y. Kivshar, "Giant nonlinear response at the nanoscale driven by bound states in the continuum," Phys. Rev. Lett. **121**, 033903 (2018).
[74]B. Sain, C. Meier, and T. Zentgraf, "Nonlinear optics in all-dielectric nanoantennas and metasurfaces: A review," Advanced Photonics **1**(2), 024002 (2019).
[75]A. Krasnok, M. Tymchenko, and A. Alù, "Nonlinear metasurfaces: A paradigm shift in nonlinear optics," Mater. Today **21**(1), 8–21 (2018).
[76]M. Fox, *Optical Properties of Solid* (Oxford University Press, 2001).
[77]M. B. Lee, M. Kawasaki, M. Yoshimoto, M. Kumagai, and H. Koinuma, "Epitaxial growth of highly crystalline and conductive nitride films by pulsed laser deposition," Jpn. J. Appl. Phys., Part 1 **33**(11R), 6308 (1994).
[78]A. Catellani and A. Calzolari, "Plasmonic properties of refractory titanium nitride," Phys. Rev. B **95**(11), 115145 (2017).
[79]D. Shah, A. Catellani, H. Reddy, N. Kinsey, V. Shalaev, A. Boltasseva, and A. Calzolari, "Controlling the plasmonic properties of ultrathin TiN films at the atomic level," ACS Photonics **5**(7), 2816–2824 (2018).
[80]N. Izyumskaya, D. Fomra, K. Ding, H. Morkoç, N. Kinsey, Ü. Özgür, and V. Avrutin, "High-quality plasmonic materials TiN and ZnO:Al by atomic layer deposition," Phys. Status Solidi RRL **15**, 2100227 (2021).
[81]K. Ding, D. Fomra, A. V. Kvit, H. Morkoç, N. Kinsey, Ü. Özgür, and V. Avrutin, "A platform for complementary metal-oxide-semiconductor compatible plasmonics: High plasmonic quality titanium nitride thin films on Si (001) with a MgO interlayer," Adv. Photonics Res. **2**(7), 2000210 (2021).
[82]D. Fomra, R. Secondo, K. Ding, V. Avrutin, N. Izyumskaya, Ü. Özgür, and N. Kinsey, "Plasmonic titanium nitride via atomic layer deposition: A low-temperature route," J. Appl. Phys. **127**(10), 103101 (2020).
[83]D. Fomra, M. Mamun, K. Ding, V. Avrutin, Ü. Özgür, and N. Kinsey, "Plasmonic colors in titanium nitride for robust and covert security features," Opt. Express **29**(13), 19586 (2021).
[84]W.-P. Guo, R. Mishra, C.-W. Cheng, B.-H. Wu, L.-J. Chen, M.-T. Lin, and S. Gwo, "Titanium nitride epitaxial films as a plasmonic material platform: Alternative to gold," ACS Photonics **6**(8), 1848–1854 (2019).
[85]G. V. Naik, V. M. Shalaev, and A. Boltasseva, "Alternative plasmonic materials: Beyond gold and silver," Adv. Mater. **25**(24), 3264–3294 (2013).
[86]J. A. Briggs, G. V. Naik, T. A. Petach, B. K. Baum, D. Goldhaber-Gordon, and J. A. Dionne, "Fully CMOS-compatible titanium nitride nanoantennas," Appl. Phys. Lett. **108**(5), 051110 (2016).
[87]C. M. Zgrabik and E. L. Hu, "Optimization of sputtered titanium nitride as a tunable metal for plasmonic applications," Opt. Mater. Express **5**(12), 2786 (2015).
[88]S. Bagheri, C. M. Zgrabik, T. Gissibl, A. Tittl, F. Sterl, R. Walter, S. De Zuani, A. Berrier, T. Stauden, G. Richter, E. L. Hu, and H. Giessen, "Large-area fabrication of TiN nanoantenna arrays for refractory plasmonics in the mid-infrared by femtosecond direct laser writing and interference lithography [Invited]," Opt. Mater. Express **5**(11), 2625 (2015).
[89]M. Popović, M. Novaković, E. Schmidt, P. Schöppe, N. Bibić, C. Ronning, and Z. Rakočević, "Low-loss and tunable near-zero-epsilon titanium nitride," Opt. Mater. **72**, 775–780 (2017).
[90]P. Patsalas, "Zirconium nitride: A viable candidate for photonics and plasmonics?," Thin Solid Films **688**, 137438 (2019).
[91]P. Patsalas, N. Kalfagiannis, S. Kassavetis, G. Abadias, D. V. Bellas, C. Lekka, and E. Lidorikis, "Conductive nitrides: Growth principles, optical and electronic properties, and their perspectives in photonics and plasmonics," Mater. Sci. Eng. R **123**, 1–55 (2018).
[92]R. Sato, S. Ishii, T. Nagao, M. Naito, and Y. Takeda, "Broadband plasmon resonance enhanced third-order optical nonlinearity in refractory titanium nitride nanostructures," ACS Photonics **5**(9), 3452–3458 (2018).
[93]A. Capretti, Y. Wang, N. Engheta, and L. Dal Negro, "Comparative study of second-harmonic generation from epsilon-near-zero indium tin oxide and titanium nitride nanolayers excited in the near-infrared spectral range," ACS Photonics **2**(11), 1584–1591 (2015).
[94]D. D. Smith, Y. Yoon, R. W. Boyd, J. K. Campbell, L. A. Baker, R. M. Crooks, and M. George, "z-scan measurement of the nonlinear absorption of a thin gold film," J. Appl. Phys. **86**(11), 6200–6205 (1999).
[95]S. Benis, N. Munera, S. Faryadras, E. W. Van Stryland, and D. J. Hagan, "Extremely large nondegenerate nonlinear index and phase shift in epsilon-near-zero materials [Invited]," Opt. Mater. Express **12**(10), 3856 (2022).
[96]S. Benis, N. Munera, R. Acuna, D. J. Hagan, and E. W. Van Stryland, "Nonlinear Fresnel coefficients due to giant ultrafast nonlinearities in indium tin oxide (Conference Presentation)," Ultrafast Phenomena and Nanophotonics XXIII **10916**, 1091610 (2019).
[97]J. Bohn, T. S. Luk, C. Tollerton, S. W. Hutchings, I. Brener, S. Horsley, W. L. Barnes, and E. Hendry, "All-optical switching of an epsilon-near-zero plasmon resonance in indium tin oxide," Nat. Commun. **12**(1), 1017 (2021).
[98]D. Fomra, K. Ding, V. Avrutin, Ü. Özgür, and N. Kinsey, "Al:ZnO as a platform for near-zero-index photonics: Enhancing the doping efficiency of atomic layer deposition," Opt. Mater. Express **10**(12), 3060–3072 (2020).
[99]Y. Gui, M. Miscuglio, Z. Ma, M. H. Tahersima, S. Sun, R. Amin, H. Dalir, and V. J. Sorger, "Towards integrated metatronics: A holistic approach on precise optical and electrical properties of Indium Tin Oxide," Sci. Rep. **9**(1), 11279 (2019).
[100]A. Anopchenko, S. Gurung, L. Tao, C. Arndt, and H. W. H. Lee, "Atomic layer deposition of ultra-thin and smooth Al-doped ZnO for zero-index photonics," Mater. Res. Express **5**(1), 014012 (2018).
[101]Z. Wang, C. Chen, K. Wu, H. Chong, and H. Ye, "Transparent conductive oxides and their applications in near infrared plasmonics," Phys. Status Solidi A **216**(5), 1700794 (2019).
[102]E. L. Runnerstrom, K. P. Kelley, E. Sachet, C. T. Shelton, and J.-P. Maria, "Epsilon-near-zero modes and surface plasmon resonance in fluorine-doped cadmium oxide thin films," ACS Photonics **4**(8), 1885–1892 (2017).
[103]C. Y. Liu, B. P. Zhang, N. T. Binh, and Y. Segawa, "Third-harmonic generation from ZnO films deposited by MOCVD," Appl. Phys. B **79**(1), 83–86 (2004).
[104]B. Buchalter and G. R. Meredith, "Third-order optical susceptibility of glasses determined by third harmonic generation," Appl. Opt. **21**(17), 3221–3224 (1982).
[105]D. N. Christodoulides, I. C. Khoo, G. I. Stegeman, E. W. Van Stryland, and G. J. Salamo, "Nonlinear refraction and absorption: Mechanisms and magnitudes," Adv. Opt. Photonics **2**(1), 60–200 (2010).
[106]F. Zhang, X. Xiao, Y. Lu, J. Dong, and Y. Chen, "Broadband enhancement of optical nonlinearity in a plasmonic nanocavity coupled with an epsilon-near-zero film," J. Phys. Chem. C **127**, 3726 (2022).
[107]O. Reshef, P. Camayd-Muñoz, D. I. Vulis, Y. Li, M. Lončar, and E. Mazur, "Direct observation of phase-free propagation in a silicon waveguide," ACS Photonics **4**(10), 2385–2389 (2017).
[108]A. Ciattoni, A. Marini, C. Rizza, M. Scalora, and F. Biancalana, "Polariton excitation in epsilon-near-zero slabs: Transient trapping of slow light," Phys. Rev. A **87**(5), 053853 (2013).
[109]M. H. Javani and M. I. Stockman, "Real and imaginary properties of epsilon-near-zero materials," Phys. Rev. Lett. **117**(10), 107404 (2016).
[110]J. B. Khurgin, "Slow light in various media: A tutorial," Adv. Opt. Photonics **2**(3), 287 (2010).

[111]R. W. Boyd, "Material slow light and structural slow light: Similarities and differences for nonlinear optics [Invited]," J. Opt. Soc. Am. B **28**(12), A38–A44 (2011).
[112]A. Calzolari, A. Ruini, and A. Catellani, "Transparent conductive oxides as near-IR plasmonic materials: The case of Al-doped ZnO derivatives," ACS Photonics **1**(8), 703–709 (2014).
[113]R. Amin, J. B. Khurgin, and V. J. Sorger, "Waveguide-based electro-absorption modulator performance: Comparative analysis," Opt. Express **26**(12), 203–204 (2018).
[114]V. J. Sorger, N. D. Lanzillotti-Kimura, R. M. Ma, and X. Zhang, "Ultra-compact silicon nanophotonic modulator with broadband response," Nanophotonics **1**(1), 17–22 (2012).
[115]C. Fruhling, M. G. Ozlu, S. Saha, A. Boltasseva, and V. M. Shalaev, "Understanding all-optical switching at the epsilon-near-zero point: A tutorial review," Appl. Phys. B **128**(2), 34 (2022).
[116]J. Wu, Z. T. Xie, Y. Sha, H. Y. Fu, and Q. Li, "Epsilon-near-zero photonics: Infinite potentials," Photonics Res. **9**(8), 1616 (2021).
[117]V. E. Babicheva, A. Boltasseva, and A. V. Lavrinenko, "Transparent conducting oxides for electro-optical plasmonic modulators," Nanophotonics **4**(1), 165–185 (2015).
[118]I. C. Reines, M. G. Wood, T. S. Luk, D. K. Serkland, and S. Campione, "Compact epsilon-near-zero silicon photonic phase modulators," Opt. Express **26**(17), 21594 (2018).
[119]J. D. Caldwell, L. Lindsay, V. Giannini, I. Vurgaftman, T. L. Reinecke, S. A. Maier, and O. J. Glembocki, "Low-loss, infrared and terahertz nanophotonics using surface phonon polaritons," Nanophotonics **4**(1), 44–68 (2015).
[120]J. Kim, A. Dutta, G. V. Naik, A. J. Giles, F. J. Bezares, C. T. Ellis, J. G. Tischler, A. M. Mahmoud, H. Caglayan, O. J. Glembocki, A. V. Kildishev, J. D. Caldwell, A. Boltasseva, and N. Engheta, "Role of epsilon-near-zero substrates in the optical response of plasmonic antennas," Optica **3**(3), 339 (2016).
[121]N. C. Passler, I. Razdolski, D. S. Katzer, D. F. Storm, J. D. Caldwell, M. Wolf, and A. Paarmann, "Second harmonic generation from phononic epsilon-near-zero Berreman modes in ultrathin polar crystal films," ACS Photonics **6**(6), 1365–1371 (2019).
[122]Q. Hu, X. Yu, H. Liu, J. Qiu, W. Tang, S. Liang, L. Li, M. Du, J. Jia, and H. Ye, "Tunable organic ENZ materials with large optical nonlinearity," ACS Photonics **10**(10), 3612–3620 (2023).
[123]Y. U. Lee, E. Garoni, H. Kita, K. Kamada, B. H. Woo, Y. C. Jun, S. M. Chae, H. J. Kim, K. J. Lee, S. Yoon, E. Choi, F. Mathevet, I. Ozerov, J. C. Ribierre, J. W. Wu, and A. D'Aléo, "Strong nonlinear optical response in the visible spectral range with epsilon-near-zero organic thin films," Adv. Opt. Mater. **6**(14), 1701400 (2018).
[124]X. Yu, X. Yu, J. Qiu, J. Qiu, Q. Hu, K. Chen, J. Zheng, S. Liang, M. Du, M. Du, and H. Ye, "Tunable Berreman mode in highly conductive organic thin films," Opt. Express **30**(24), 43590–43600 (2022).
[125]M. H. Ebrahim, A. Marini, V. Bruno, N. Kinsey, J. B. Khurgin, D. Faccio, and M. Clerici, "Temporal dynamics of strongly coupled epsilon near-zero plasmonic systems," Appl. Phys. Lett. **119**(22), 221101 (2021).
[126]S. Foteinopoulou, G. C. R. Devarapu, G. S. Subramania, S. Krishna, and D. Wasserman, "Phonon-polaritonics: Enabling powerful capabilities for infrared photonics," Nanophotonics **8**, 2129–2175 (2019).
[127]M. T. Hassan, T. T. Luu, A. Moulet, O. Raskazovskaya, P. Zhokhov, M. Garg, N. Karpowicz, A. M. Zheltikov, V. Pervak, F. Krausz, and E. Goulielmakis, "Optical attosecond pulses and tracking the nonlinear response of bound electrons," Nature **530**(7588), 66–70 (2016).
[128]R. L. Sutherland, *Handbook of Nonlinear Optics*, 2nd ed. (CRC Press, 2003).
[129]M. Clerici, N. Kinsey, C. DeVault, J. Kim, E. G. Carnemolla, L. Caspani, A. Shaltout, D. Faccio, V. Shalaev, A. Boltasseva, and M. Ferrera, "Controlling hybrid nonlinearities in transparent conducting oxides via two-colour excitation," Nat. Commun. **8**, 15829 (2017).
[130]S. Benis, D. J. Hagan, and E. W. Van Stryland, in *Conference on Lasers and Electro-Optics* (OSA, Washington, DC, 2018).
[131]C. Li, X. Tian, G. Yang, S. U. Dev, M. S. Allen, J. W. Allen, and H. Harutyunyan, "Invertible optical nonlinearity in epsilon-near-zero materials," Phys. Rev. Res. **5**(1), 013198 (2023).
[132]J. B. Khurgin, M. Clerici, V. Bruno, L. Caspani, C. DeVault, J. Kim, A. Shaltout, A. Boltasseva, V. M. Shalaev, M. Ferrera, D. Faccio, and N. Kinsey, "Adiabatic frequency shifting in epsilon-near-zero materials: The role of group velocity," Optica **7**(3), 226 (2020).
[133]R. DeSalvo, A. A. Said, D. J. Hagan, E. W. Van Stryland, and M. Sheik-Bahae, "Infrared to ultraviolet measurements of two-photon absorption and n_2 in wide bandgap solids," IEEE J. Quantum Electron. **32**(8), 1324–1333 (1996).
[134]W. Tian, F. Liang, D. Lu, H. Yu, and H. Zhang, "Highly efficient ultraviolet high-harmonic generation from epsilon-near-zero indium tin oxide films," Photonics Res. **9**(3), 317 (2021).
[135]W. Jaffray, F. Belli, E. G. Carnemolla, C. Dobas, M. Mackenzie, J. Travers, A. K. Kar, M. Clerici, C. DeVault, V. M. Shalaev, A. Boltasseva, and M. Ferrera, "Near-zero-index ultra-fast pulse characterization," Nat. Commun. **13**(1), 3536 (2022).
[136]I. A. Kolmychek, V. B. Novikov, I. V. Malysheva, A. P. Leontiev, K. S. Napolskii, and T. V. Murzina, "Second-harmonic generation spectroscopy in gold nanorod-based epsilon-near-zero metamaterials," Opt. Lett. **45**(7), 1866 (2020).
[137]A. Capretti, Y. Wang, N. Engheta, and L. Dal Negro, "Enhanced third-harmonic generation in Si-compatible epsilon-near-zero indium tin oxide nanolayers," Opt. Lett. **40**(7), 1500 (2015).
[138]L. Rodríguez-Suné, M. Scalora, A. S. Johnson, C. Cojocaru, N. Akozbek, Z. J. Coppens, D. Perez-Salinas, S. Wall, and J. Trull, "Study of second and third harmonic generation from an indium tin oxide nanolayer: Influence of nonlocal effects and hot electrons," APL Photonics **5**(1), 010801 (2020).
[139]J. Wu, B. A. Malomed, H. Y. Fu, and Q. Li, "Self-interaction of ultrashort pulses in an epsilon-near-zero nonlinear material at the telecom wavelength," Opt. Express **27**(26), 37298 (2019).
[140]H. Wang, K. Du, C. Jiang, Z. Yang, L. Ren, W. Zhang, S. J. Chua, and T. Mei, "Extended Drude model for intraband-transition-induced optical nonlinearity," Phys. Rev. Appl. **11**(6), 064062 (2019).
[141]J. K. Chen, D. Y. Tzou, and J. E. Beraun, "A semiclassical two-temperature model for ultrafast laser heating," Int. J. Heat Mass Transfer **49**(1–2), 307–316 (2006).
[142]J. Hohlfeld, S. S. Wellershoff, J. Güdde, U. Conrad, V. Jähnke, and E. Matthias, "Electron and lattice dynamics following optical excitation of metals," Chem. Phys. **251**(1–3), 237–258 (2000).
[143]A. Block, M. Liebel, R. Yu, M. Spector, Y. Sivan, F. J. García De Abajo, and N. F. Van Hulst, "Tracking ultrafast hot-electron diffusion in space and time by ultrafast thermomodulation microscopy," Sci. Adv. **5**(5), eaav8965 (2019).
[144]A. Block, R. Yu, I.-W. Un, S. Varghese, M. Liebel, N. F. van Hulst, S. Fan, K.-J. Tielrooij, and Y. Sivan, "Observation of negative effective thermal diffusion in gold films," ACS Photonics **10**, 1150 (2023).
[145]J. B. Smith and H. Ehrenreich, "Frequency dependence of the optical relaxation time in metals," Phys. Rev. B **25**(2), 923 (1982).
[146]A. Schenk, "A model for the field and temperature dependence of Shockley-Read-Hall lifetimes in silicon," Solid-State Electron. **35**(11), 1585–1596 (1992).
[147]M. Haiml, U. Siegner, F. Morier-Genoud, U. Keller, M. Luysberg, R. C. Lutz, P. Specht, and E. R. Weber, "Optical nonlinearity in low-temperature-grown GaAs: Microscopic limitations and optimization strategies," Appl. Phys. Lett. **74**(21), 3134–3136 (1999).
[148]R. Secondo, A. Ball, B. Diroll, D. Fomra, K. Ding, V. Avrutin, Ü. Özgür, D. O. Demchenko, J. B. Khurgin, and N. Kinsey, "Deterministic modeling of hybrid nonlinear effects in epsilon-near-zero thin films," Appl. Phys. Lett. **120**(3), 031103 (2022).
[149]Y. Yang, K. Kelley, E. Sachet, S. Campione, T. S. Luk, J. P. Maria, M. B. Sinclair, and I. Brener, "Femtosecond optical polarization switching using a cadmium oxide-based perfect absorber," Nat. Photonics **11**(6), 390–395 (2017).
[150]A. A. Ionin, S. I. Kudryashov, S. V. Makarov, P. N. Saltuganov, L. V. Seleznev, D. V. Sinitsyn, and A. R. Sharipov, "Ultrafast electron dynamics on the silicon surface excited by an intense femtosecond laser pulse," JETP Lett. **96**(6), 375–379 (2012).
[151]J. Shah, R. F. Leheny, and C. Lin, "Dynamic Burstein shift in GaAs," Solid State Commun. **18**(8), 1035–1037 (1976).
[152]M. K. Hudait, P. Modak, and S. B. Krupanidhi, "Si incorporation and Burstein–Moss shift in n-type GaAs," Mater. Sci. Eng. **60**(1), 1–11 (1999).
[153]S. Benis, N. Munera, E. W. Van Stryland, and D. J. Hagan, "Enhanced nonlinear phase-shift in epsilon-near-zero materials: The effect of group and phase velocity," in Conference on Lasers and Electro-Optics Pacific Rim (CLEO-PR), 2020.

[154]P. Guo, R. D. Schaller, J. B. Ketterson, and R. P. H. Chang, "Ultrafast switching of tunable infrared plasmons in indium tin oxide nanorod arrays with large absolute amplitude," Nat. Photonics **10**(4), 267–273 (2016).
[155]E. S. Harmon, M. R. Melloch, J. M. Woodall, D. D. Nolte, N. Otsuka, and C. L. Chang, "Carrier lifetime versus anneal in low temperature growth GaAs," Appl. Phys. Lett. **63**(16), 2248–2250 (1993).
[156]A. J. Sabbah and D. M. Riffe, "Femtosecond pump-probe reflectivity study of silicon carrier dynamics," Phys. Rev. B **66**(16), 165217 (2002).
[157]H. Morkoç and Ü. Özgür, *Zinc Oxide: Fundamentals, Materials and Device Technology* (John Wiley & Sons, Hoboken, NJ, 2008).
[158]S. Gupta, J. F. Whitaker, and G. A. Mourou, "Ultrafast carrier dynamics in III-V semiconductors grown by molecular-beam epitaxy at very low substrate temperatures," IEEE J Quantum Electron. **28**(10), 2464–2472 (1992).
[159]N. P. Wells, P. M. Belden, J. R. Demers, and W. T. Lotshaw, "Transient reflectivity as a probe of ultrafast carrier dynamics in semiconductors: A revised model for low-temperature grown GaAs," J. Appl. Phys. **116**(7), 073506 (2014).
[160]M. Lobet, N. Kinsey, I. Liberal, H. Caglayan, P. A. Huidobro, E. Galiffi, J. R. Mejía-Salazar, G. Palermo, Z. Jacob, and N. Maccaferri, "New horizons in near-zero refractive index photonics and hyperbolic metamaterials," ACS Photonics **10**(11), 3805–3820 (2023).
[161]N. Vermeulen, D. Espinosa, A. Ball, J. M. Ballato, P. Boucaud, G. Boudebs, C. V. Campos, P. D. Dragic, A. Gomes, M. J. Huttunen, N. Kinsey, R. P. Mildren, D. Neshev, L. Padilha, M. Pu, R. Secondo, E. Tokunaga, D. Turchinovich, J. Yan, K. Yvind, K. Dolgaleva, and E. van Stryland," "Post-2000 nonlinear optical materials and measurements: Data tables and best practices," J. Phys. **5**, 035001 (2022).
[162]A. Ball, R. Secondo, B. T. Diroll, D. Fomra, K. Ding, V. Avrutin, Ü. Özgür, and N. Kinsey, "Gallium-doped zinc oxide: Nonlinear reflection and transmission measurements and modeling in the ENZ region," J. Phys. **5**(2), 024001 (2023).
[163]X. Li, M. Pietrzyk, D. Faccio, C. Rizza, A. Ciattoni, A. X. Li, and A. Di Falco, "Linear and nonlinear optical behavior of epsilon near zero metamaterials: Opportunities and challenges," Proc. SPIE **10111**, 101111O (2017).
[164]M. Ferrera, S. Saha, A. Boltasseva, V. M. Shalaev, and W. Jaffray, "Transparent conducting oxides: From all-dielectric plasmonics to a new paradigm in integrated photonics," Adv. Opt. Photonics **14**(2), 148–208 (2022).
[165]E. G. Carnemolla, L. Caspani, C. DeVault, M. Clerici, S. Vezzoli, V. Bruno, V. M. Shalaev, D. Faccio, A. Boltasseva, and M. Ferrera, "Degenerate optical nonlinear enhancement in epsilon-near-zero transparent conducting oxides," Opt. Mater. Express **8**(11), 3392 (2018).
[166]M. Y. Helali, M. M. Saadeldin, and M. Ibrahim, "Effects of laser irradiation on the microstructure and surface morphology of zinc oxide doped with different additives," Curr. Sci. **116**(11), 1818 (2019).
[167]N. Nosidlak, J. Jaglarz, P. Dulian, R. Pietruszka, B. S. Witkowski, M. Godlewski, W. Powroźnik, and T. Stapiński, "The thermo-optical and optical properties of thin ZnO and AZO films produced using the atomic layer deposition technology," J. Alloys Compd. **900**, 163313 (2022).
[168]A. Agrawal, J. T. Andrews, T. A. Dar, P. Sen, and P. K. Sen, "Negative thermo-optic coefficients and optical limiting response in pulsed laser deposited Mg-doped ZnO thin films," J. Opt. Soc. Am. B **33**(9), 2015–2019 (2016).
[169]E. Battal and A. K. Okyay, "Actively tunable thin films for visible light by thermo-optic modulation of ZnO," Phys. Status Solidi A **213**(5), 1340–1345 (2016).
[170]R. Secondo, D. Fomra, N. Izyumskaya, V. Avrutin, J. N. Hilfiker, A. Martin, Ü. Özgür, and N. Kinsey, "Reliable modeling of ultrathin alternative plasmonic materials using spectroscopic ellipsometry [Invited]," Opt. Mater. Express **9**(2), 760 (2019).
[171]R. Amin, J. K. George, S. Sun, T. Ferreira De Lima, A. N. Tait, J. B. Khurgin, M. Miscuglio, B. J. Shastri, P. R. Prucnal, T. El-Ghazawi, and V. J. Sorger, "ITO-based electro-absorption modulator for photonic neural activation function," APL Mater. **7**(8), 081112 (2019).
[172]Y. Wu, S. N. Chowdhury, L. Kang, S. S. Saha, A. Boltasseva, A. V. Kildishev, and D. H. Werner, "Zinc oxide (ZnO) hybrid metasurfaces exhibiting broadly tunable topological properties," Nanophotonics **11**(17), 3933–3942 (2022).
[173]Y. W. Huang, H. W. H. Lee, R. Sokhoyan, R. A. Pala, K. Thyagarajan, S. Han, D. P. Tsai, and H. A. Atwater, "Gate-tunable conducting oxide metasurfaces," Nano Lett. **16**(9), 5319–5325 (2016).
[174]L. Kang, R. P. Jenkins, and D. H. Werner, "Recent progress in active optical metasurfaces," Adv. Opt. Mater. **7**(14), 1801813 (2019).
[175]D. Ghindani, A. R. Rashed, M. Habib, and H. Caglayan, "Gate tunable coupling of epsilon-near-zero and plasmonic modes," Adv. Opt. Mater. **9**(22), 2100800 (2021).
[176]M. Sojib, D. Fomra, V. Avrutin, Ü. Özgür, and N. Kinsey, "Optimizing epsilon-near-zero based plasmon assisted modulators through surface-to-volume ratio," Opt. Express **30**(11), 19781 (2022).
[177]V. Bruno, C. Devault, S. Vezzoli, Z. Kudyshev, T. Huq, S. Mignuzzi, A. Jacassi, S. Saha, Y. D. Shah, S. A. Maier, D. R. S. Cumming, A. Boltasseva, M. Ferrera, M. Clerici, D. Faccio, R. Sapienza, and V. M. Shalaev, "Negative refraction in time-varying strongly coupled plasmonic-antenna-epsilon-near-zero systems," Phys. Rev. Lett. **124**(4), 043902 (2020).
[178]M. Ren, W. Cai, and J. Xu, "Tailorable dynamics in nonlinear optical metasurfaces," Adv. Mater. **32**(3), 1806317 (2020).
[179]A. Anopchenko, L. Tao, C. Arndt, and H. W. H. Lee, "Field-effect tunable and broadband epsilon-near-zero perfect absorbers with deep subwavelength thickness," ACS Photonics **5**(7), 2631–2637 (2018).
[180]T. S. Luk, D. de Ceglia, S. Liu, G. A. Keeler, R. P. Prasankumar, M. A. Vincenti, M. Scalora, M. B. Sinclair, and S. Campione, "Enhanced third harmonic generation from the epsilon-near-zero modes of ultrathin films," Appl. Phys. Lett. **106**(15), 151103 (2015).
[181]F. Hu, W. Jia, Y. Meng, M. Gong, and Y. Yang, "High-contrast optical switching using an epsilon-near-zero material coupled to a Bragg microcavity," Opt. Express **27**(19), 26405 (2019).
[182]B. Johns, "Dispersion engineering of infrared epsilon-near-zero modes by strong coupling to optical cavities," Nanophotonics **12**(16), 3301–3312 (2023).
[183]V. Caligiuri, M. Palei, M. Imran, L. Manna, and R. Krahne, "Planar double-epsilon-near-zero cavities for spontaneous emission and Purcell effect enhancement," ACS Photonics **5**(6), 2287–2294 (2018).
[184]X. Wen, G. Li, C. Gu, J. Zhao, S. Wang, C. Jiang, S. Palomba, C. Martijn de Sterke, and Q. Xiong, "Doubly enhanced second harmonic generation through structural and epsilon-near-zero resonances in TiN nanostructures," ACS Photonics **5**(6), 2087–2093 (2018).
[185]K. Wang, M. Li, H. H. Hsiao, F. Zhang, M. Seidel, A. Y. Liu, J. Chen, E. Devaux, C. Genet, and T. Ebbesen, "High contrast, femtosecond light polarization manipulation in epsilon-near-zero material coupled to a plasmonic nanoantenna array," ACS Photonics **8**(9), 2791–2799 (2021).
[186]Y. Lu, X. Feng, Q. Wang, X. Zhang, M. Fang, W. E. I. Sha, Z. Huang, Q. Xu, L. Niu, X. Chen, C. Ouyang, Y. Yang, X. Zhang, E. Plum, S. Zhang, J. Han, and W. Zhang, "Integrated terahertz generator-manipulators using epsilon-near-zero-hybrid nonlinear metasurfaces," Nano Lett. **21**(18), 7699–7707 (2021).
[187]S. Campione, I. Brener, and F. Marquier, "Theory of epsilon-near-zero modes in ultrathin films," Phys. Rev. B **91**(12), 121408 (2015).
[188]D. M. Solís, R. W. Boyd, and N. Engheta, "Dependence of the efficiency of the nonlinear-optical response of materials on their linear permittivity and permeability," Laser Photon Rev. **15**(12), 2100032 (2021).
[189]X. Niu, X. Hu, Q. Sun, C. Lu, Y. Yang, H. Yang, and Q. Gong, "Polarization-selected nonlinearity transition in gold dolmens coupled to an epsilon-near-zero material," Nanophotonics **9**(16), 4839–4851 (2020).
[190]K. Bae, J. Zhu, C. Wolenski, A. Das, T. M. Horning, S. Pampel, M. B. Grayson, M. Zohrabi, J. T. Gopinath, and W. Park, "Indium tin oxide nanoparticle-coated silica microsphere with large optical nonlinearity and high quality factor," ACS Photonics **7**(11), 3042–3048 (2020).
[191]Y. Li, C. T. Chan, and E. Mazur, "Dirac-like cone-based electromagnetic zero-index metamaterials," Light **10**(1), 203 (2021).
[192]R. Maas, J. Parsons, N. Engheta, and A. Polman, "Experimental realization of an epsilon-near-zero metamaterial at visible wavelengths," Nat. Photonics **7**(11), 907–912 (2013).
[193]G. Subramania, A. J. Fischer, and T. S. Luk, "Optical properties of metal-dielectric based epsilon near zero metamaterials," Appl. Phys. Lett. **101**(24), 241107 (2012).
[194]A. R. Rashed, B. Can Yildiz, S. R. Ayyagari, and H. Caglayan, "Hot electron dynamics in ultrafast multilayer epsilon-near-zero metamaterials," Phys. Rev. B **101**, 165301 (2020).
[195]G. V. Naik, B. Saha, J. Liu, S. M. Saber, E. A. Stach, J. M. K. Irudayaraj, T. D. Sands, V. M. Shalaev, and A. Boltasseva, "Epitaxial superlattices with titanium

nitride as a plasmonic component for optical hyperbolic metamaterials," Proc. Natl. Acad. Sci. U. S. A. **111**(21), 7546–7551 (2014).
[196]R. Lemasters, C. Zhang, M. Manjare, W. Zhu, J. Song, S. Urazhdin, H. J. Lezec, A. Agrawal, and H. Harutyunyan, "Ultrathin wetting layer-free plasmonic gold films," ACS Photonics **6**(11), 2600–2606 (2019).
[197]X. Huang, Y. Lai, Z. H. Hang, H. Zheng, and C. T. Chan, "Dirac cones induced by accidental degeneracy in photonic crystals and zero-refractive-index materials," Nat. Mater. **10**(8), 582–586 (2011).
[198]W. Rotman, "Plasma simulation by artificial dielectrics and parallel-plate media," IEEE Trans. Antennas Propag. **10**, 82–95 (1961).
[199]B. Edwards, A. Alù, M. E. Young, M. Silveirinha, and N. Engheta, "Experimental verification of epsilon-near-zero metamaterial coupling and energy squeezing using a microwave waveguide," Phys. Rev. Lett. **100**(3), 033903 (2008).
[200]E. J. R. Vesseur, T. Coenen, H. Caglayan, N. Engheta, and A. Polman, "Experimental verification of n = 0 structures for visible light," Phys. Rev. Lett. **110**(1), 013902 (2013).
[201]S. Suresh, O. Reshef, M. Z. Alam, J. Upham, M. Karimi, and R. W. Boyd, "Enhanced nonlinear optical responses of layered epsilon-near-zero metamaterials at visible frequencies," ACS Photonics **8**(1), 125–129 (2021).
[202]D. Genchi, I. G. Balasa, T. Cesca, and G. Mattei, "Tunable third-order nonlinear optical response in ϵ-near-zero multilayer metamaterials," Phys. Rev. Appl. **16**(6), 064020 (2021).
[203]A. D. Neira, N. Olivier, M. E. Nasir, W. Dickson, G. A. Wurtz, and A. V. Zayats, "Eliminating material constraints for nonlinearity with plasmonic metamaterials," Nat. Commun. **6**(1), 7757 (2015).
[204]I. A. Kolmychek, I. V. Malysheva, A. P. Leontiev, K. S. Napolskii, and T. V. Murzina, "Self-action effects in hyperbolic metamaterials based on gold nanorods," Opt. Lett. **47**(22), 6009 (2022).
[205]S. Yun, Z. H. Jiang, Q. Xu, Z. Liu, D. H. Werner, and T. S. Mayer, "Low-loss impedance-matched optical metamaterials with zero-phase delay," ACS Nano **6**(5), 4475–4482 (2012).
[206]J. Kuttruff, D. Garoli, J. Allerbeck, R. Krahne, A. De Luca, D. Brida, V. Caligiuri, and N. Maccaferri, "Ultrafast all-optical switching enabled by epsilon-near-zero-tailored absorption in metal-insulator nanocavities," Commun. Phys. **3**(1), 114 (2020).
[207]L. Kuznetsova and P. Kelly, "Pump-probe ultrashort pulse modulation in an AZO/ZnO metamaterial at the epsilon near zero spectral point," OSA Continuum **3**(11), 3225–3236 (2020).
[208]Z. T. Xie, Y. Sha, J. Wu, J. Wu, H. Y. Fu, and Q. Li, "Ultrafast dynamic switching of optical response based on nonlinear hyperbolic metamaterial platform," Opt. Express **30**(12), 21634–21648 (2022).
[209]J. Gosciniak, Z. Hu, M. Thomaschewski, V. J. Sorger, and J. B. Khurgin, "Bistable all-optical devices based on nonlinear epsilon-near-zero (ENZ) materials," Laser Photon Rev. **17**(4), 2200723 (2023).
[210]Y. Li and C. Argyropoulos, "Tunable nonlinear coherent perfect absorption with epsilon-near-zero plasmonic waveguides," Opt. Lett. **43**(8), 1806–1809 (2018).
[211]W. Shi, H. Liu, and Z. Wang, "Gain-assisted giant third-order nonlinearity of epsilon-near-zero multilayered metamaterials," Nanomaterials **12**(19), 3499 (2022).
[212]M. A. Vincenti, M. Scalora, and D. de Ceglia, "ENZ materials and anisotropy: Enhancing nonlinear optical interactions at the nanoscale," Opt. Express **28**(21), 31180–31196 (2020).
[213]S. Jahani, H. Zhao, and Z. Jacob, "Switching Purcell effect with nonlinear epsilon-near-zero media," Appl. Phys. Lett. **113**, 021103 (2018).
[214]N. Kumari, P. Yadav, Ankush, and R. K. Sinha, "Study of non-linear optical properties of an ENZ composite metamaterial," J. Phys. **2426**(1), 012006 (2023).
[215]Y. Li, Z. Zhou, Y. He, and H. Li, *Epsilon-Near-Zero Metamaterials* (Cambridge University Press, 2022).
[216]Y. Li, I. Liberal, and N. Engheta, "Structural dispersion–based reduction of loss in epsilon-near-zero and surface plasmon polariton waves," Sci. Adv. **5**(10), eaav3764 (2019).
[217]S. Saha, B. T. Diroll, J. Shank, Z. Kudyshev, A. Dutta, S. N. Chowdhury, T. S. Luk, S. Campione, R. D. Schaller, V. M. Shalaev, A. Boltasseva, and M. G. Wood, "Broadband, high-speed, and large-amplitude dynamic optical switching with yttrium-doped cadmium oxide," Adv. Funct. Mater. **30**(7), 1908377 (2020).
[218]P. Guo, R. D. Schaller, L. E. Ocola, B. T. Diroll, J. B. Ketterson, and R. P. H. Chang, "Large optical nonlinearity of ITO nanorods for sub-picosecond all-optical modulation of the full-visible spectrum," Nat. Commun. **7**(1), 12892 (2016).
[219]K. J. Palm, T. Gong, C. Shelden, E. Deniz, L. J. Krayer, M. S. Leite, and J. N. Munday, "Achieving scalable near-zero-index materials," Adv. Photonics Res. **3**(9), 2200109 (2022).
[220]Ü. Özgür, Y. Alivov, C. Liu, A. Teke, M. A. Reshchikov, S. Doğan, V. Avrutin, S.-J. Cho, and H. Morkoç, "A comprehensive review of ZnO materials and devices," J. Appl. Phys. **98**(4), 041301 (2005).
[221]K. Ellmer, F. Kudella, R. Mientus, R. Schieck, and S. Fiechter, "Influence of discharge parameters on the layer properties of reactive magnetron sputtered ZnO:Al films," Thin Solid Films **247**(1), 15–23 (1994).
[222]Y. Wang, W. Tang, L. Zhang, and J. Zhao, "Electron concentration dependence of optical band gap shift in Ga-doped ZnO thin films by magnetron sputtering," Thin Solid Films **565**, 62–68 (2014).
[223]H. Agura, A. Suzuki, T. Matsushita, T. Aoki, and M. Okuda, in *Thin Solid Films* (Elsevier, 2003), pp. 263–267.
[224]V. Bhosle, J. T. Prater, F. Yang, D. Burk, S. R. Forrest, and J. Narayan, "Gallium-doped zinc oxide films as transparent electrodes for organic solar cell applications," J. Appl. Phys. **102**(2), 023501 (2007).
[225]B. Macco and W. M. M. (Erwin) Kessels, "Atomic layer deposition of conductive and semiconductive oxides," Appl. Phys. Rev. **9**(4), 041313 (2022).
[226]J. A. Spencer, A. L. Mock, A. G. Jacobs, M. Schubert, Y. Zhang, and M. J. Tadjer, "A review of band structure and material properties of transparent conducting and semiconducting oxides: Ga_2O_3, Al_2O_3, In_2O_3, ZnO, SnO_2, CdO, NiO, CuO, and Sc_2O_3," Appl. Phys. Rev. **9**(1), 011315 (2022).
[227]S. J. Pearton, J. Yang, P. H. Cary, F. Ren, J. Kim, M. J. Tadjer, and M. A. Mastro, "A review of Ga_2O_3 materials, processing, and devices," Appl. Phys. Rev. **5**(1), 011301 (2018).
[228]A. Stadler, "Transparent conducting oxides—An up-to-date overview," Materials **5**, 661–683 (2012).
[229]G. T. Chavan, Y. Kim, M. Q. Khokhar, S. Q. Hussain, E.-C. Cho, J. Yi, Z. Ahmad, P. Rosaiah, and C.-W. Jeon, "A brief review of transparent conducting oxides (TCO): The influence of different deposition techniques on the efficiency of solar cells," Nanomaterials **13**(7), 1226 (2023).
[230]A. Klein, C. Körber, A. Wachau, F. Säuberlich, Y. Gassenbauer, S. P. Harvey, D. E. Proffit, and T. O. Mason, "Transparent conducting oxides for photovoltaics: Manipulation of Fermi level, work function and energy band alignment," Materials **3**(11), 4892–4914 (2010).
[231]H. Liu, V. Avrutin, N. Izyumskaya, Ü. Özgür, and H. Morkoç, "Transparent conducting oxides for electrode applications in light emitting and absorbing devices," Superlattices Microstruct. **48**, 458–484 (2010).
[232]T. Minami, "Substitution of transparent conducting oxide thin films for indium tin oxide transparent electrode applications," Thin Solid Films **516**(7), 1314–1321 (2008).
[233]G. Hautier, A. Miglio, D. Waroquiers, G.-M. Rignanese, and X. Gonze, "How does chemistry influence electron effective mass in oxides? A high-throughput computational analysis," Chem. Mater. **26**(19), 5447–5458 (2014).
[234]T. J. Coutts, J. D. Perkins, D. S. Ginley, and T. O. Mason, "Transparent conducting oxides: Status and opportunities in basic research," in Electrochemical Society Conference, 1999.
[235]K. Bädeker, "Über die elektrische Leitfähigkeit und die thermoelektrische Kraft einiger Schwermetallverbindungen," Ann. Phys. **327**(4), 749–766 (1907).
[236]J. E. N. Swallow, B. A. D. Williamson, S. Sathasivam, M. Birkett, T. J. Featherstone, P. A. E. Murgatroyd, H. J. Edwards, Z. W. Lebens-Higgins, D. A. Duncan, M. Farnworth, P. Warren, N. Peng, T.-L. Lee, L. F. J. Piper, A. Regoutz, C. J. Carmalt, I. P. Parkin, V. R. Dhanak, D. O. Scanlon, and T. D. Veal, "Resonant doping for high mobility transparent conductors: The case of Mo-doped In_2O_3," Mater. Horiz. **7**(1), 236–243 (2020).
[237]J. R. Bellingham, W. A. Phillips, and C. J. Adkins, "Electrical and optical properties of amorphous indium oxide," J. Phys. **2**(28), 6207–6221 (1990).
[238]R. A. Afre, N. Sharma, M. Sharon, and M. Sharon, "Transparent conducting oxide films for various applications: A review," Rev. Adv. Mater. Sci. **53**(1), 79–89 (2018).
[239]M. F. A. M. van Hest, M. S. Dabney, J. D. Perkins, D. S. Ginley, and M. P. Taylor, "Titanium-doped indium oxide: A high-mobility transparent conductor," Appl. Phys. Lett. **87**(3), 032111 (2005).

[240]T. Koida, H. Fujiwara, and M. Kondo, "Structural and electrical properties of hydrogen-doped In_2O_3 films fabricated by solid-phase crystallization," J. Non Cryst. Solids **354**(19–25), 2805–2808 (2008).
[241]R. K. Gupta, K. Ghosh, S. R. Mishra, and P. K. Kahol, "Opto-electrical properties of Ti-doped In_2O_3 thin films grown by pulsed laser deposition," Appl. Surf. Sci. **253**(24), 9422–9425 (2007).
[242]M. Morales-Masis, E. Rucavado, R. Monnard, L. Barraud, J. H. Holovský, M. Despeisse, M. Boccard, and C. Ballif, "Highly conductive and broadband transparent Zr-doped In_2O_3 as front electrode for solar cells," IEEE J. Photovoltaics **8**(5), 1202 (2018).
[243]R. K. Gupta, K. Ghosh, S. R. Mishra, and P. K. Kahol, "High mobility W-doped In_2O_3 thin films: Effect of growth temperature and oxygen pressure on structural, electrical and optical properties," Appl. Surf. Sci. **254**(6), 1661–1665 (2008).
[244]J. Xu, J. B. Liu, B. X. Liu, S. N. Li, S. H. Wei, and B. Huang, "Design of n-type transparent conducting oxides: The case of transition metal doping in In_2O_3," Adv. Electron. Mater. **4**(3), 1700553 (2018).
[245]K. O. Egbo, A. E. Adesina, C. v Ezeh, C. P. Liu, and K. M. Yu, "Effects of free carriers on the optical properties of high mobility transition metal doped In_2O_3 transparent conductors," Phys. Rev. Mater. **5**(9), 094603 (2021).
[246]T. Koida and J. Nomoto, "Effective mass of high-mobility In_2O_3-based transparent conductive oxides fabricated by solid-phase crystallization," Phys. Rev. Mater. **6**(5), 055401 (2022).
[247]T. Koida and M. Kondo, "High-mobility transparent conductive Zr-doped In_2O_3," Appl. Phys. Lett. **89**(8), 082104 (2006).
[248]C. Sun, J. A. Alonso, J. Bian, C. W. Sun, J. J. Bian, and J. A. Alonso, "Recent advances in perovskite-type oxides for energy conversion and storage applications," Adv. Energy Mater. **11**(2), 2000459 (2021).
[249]J. Biscaras, A. Kushwaha, T. Wolf, A. Rastogi, R. C. Budhani, and J. Lesueur, "Two-dimensional superconductivity at a Mott insulator/band insulator interface $LaTiO_3/SrTiO_3$," Nat. Commun. **1**, 89 (2010).
[250]A. Mercy, J. Bieder, J. Íñiguez, and P. Ghosez, "Structurally triggered metal-insulator transition in rare-earth nickelates," Nat. Commun. **8**(1), 1677 (2017).
[251]I. Grinberg, D. V. West, M. Torres, G. Gou, D. M. Stein, L. Wu, G. Chen, E. M. Gallo, A. R. Akbashev, P. K. Davies, J. E. Spanier, and A. M. Rappe, "Perovskite oxides for visible-light-absorbing ferroelectric and photovoltaic materials," Nature **503**, 509–512 (2013).
[252]J. H. Haeni, P. Irvin, W. Chang, R. Uecker, P. Reiche, Y. L. Li, S. Choudhury, W. Tian, M. E. Hawley, B. Craigo, A. K. Tagantsev, X. Q. Pan, S. K. Streiffer, L. Q. Chen, S. W. Kirchoefer, J. Levy, and D. G. Schlom, "Room-temperature ferroelectricity in strained $SrTiO_3$," Nature **430**(7001), 758–761 (2004).
[253]D. O. Scanlon, "Defect engineering of $BaSnO_3$ for high-performance transparent conducting oxide applications," Phys. Rev. B **87**(2), 161201 (2013).
[254]H. J. Kim, U. Kim, H. M. Kim, T. H. Kim, H. S. Mun, B.-G. Jeon, K. T. Hong, W.-J. Lee, C. Ju, K. H. Kim, and K. Char, "High mobility in a stable transparent perovskite oxide," Appl. Phys. Express **5**(6), 061102 (2012).
[255]X. Luo, Y. S. Oh, A. Sirenko, P. Gao, T. A. Tyson, K. Char, and S. W. Cheong, "High carrier mobility in transparent $Ba_{1-x}La_xSnO_3$ crystals with a wide band gap," Appl. Phys. Lett. **100**(17), 172112 (2012).
[256]H. He, Z. Yang, Y. Xu, A. T. Smith, G. Yang, and L. Sun, "Perovskite oxides as transparent semiconductors: A review," Nano Convergence **7**(1), 32 (2020).
[257]A. Prakash, P. Xu, A. Faghaninia, S. Shukla, J. W. Ager, C. S. Lo, and B. Jalan, "Wide bandgap $BaSnO_3$ films with room temperature conductivity exceeding 10^4 S cm^{-1}," Nat. Commun. **8**(1), 15167 (2017).
[258]S. Ismail-Beigi, F. J. Walker, S.-W. Cheong, K. M. Rabe, and C. H. Ahn, "Alkaline earth stannates: The next silicon?," APL Mater. **3**(6), 062510 (2015).
[259]C. A. Niedermeier, Y. Kumagai, K. Ide, T. Katase, F. Oba, H. Hosono, and T. Kamiya, "Phonon scattering limited mobility in the representative cubic perovskite semiconductors $SrGeO_3$, $BaSnO_3$, and $SrTiO_3$," Phys. Rev. B **101**(12), 125206 (2020).
[260]P. Kanhere and Z. Chen, "A review on visible light active perovskite-based photocatalysts," Molecules **19**(12), 19995–20022 (2014).
[261]A. Kumar, A. Kumar, and V. Krishnan, "Perovskite oxide based materials for energy and environment-oriented photocatalysis," ACS Catal. **10**(17), 10253–10315 (2020).
[262]K. P. Ong, X. Fan, A. Subedi, M. B. Sullivan, and D. J. Singh, "Transparent conducting properties of $SrSnO_3$ and $ZnSnO_3$," APL Mater. **3**(6), 062505 (2015).
[263]M. Mirjolet, M. Kataja, T. K. Hakala, P. Komissinskiy, L. Alff, G. Herranz, and J. Fontcuberta, "Optical plasmon excitation in transparent conducting $SrNbO_3$ and $SrVO_3$ thin films," Adv. Opt. Mater. **9**(17), 2100520 (2021).
[264]S. Abel, T. Stöferle, C. Marchiori, C. Rossel, M. D. Rossell, R. Erni, D. Caimi, M. Sousa, A. Chelnokov, B. J. Offrein, and J. Fompeyrine, "A strong electro-optically active lead-free ferroelectric integrated on silicon," Nat. Commun. **4**(1), 1671 (2013).
[265]M. Acosta, N. Novak, V. Rojas, S. Patel, R. Vaish, J. Koruza, G. A. Rossetti, and J. Rödel, "$BaTiO_3$-based piezoelectrics: Fundamentals, current status, and perspectives," Appl. Phys. Rev. **4**(4), 041305 (2017).
[266]H. Mizoguchi, T. Kamiya, S. Matsuishi, and H. Hosono, "A germanate transparent conductive oxide," Nat. Commun. **2**(1), 470 (2011).
[267]K. Ozdogan, M. Upadhyay Kahaly, S. R. Sarath Kumar, H. N. Alshareef, and U. Schwingenschlögl, "Enhanced carrier density in Nb-doped $SrTiO_3$ thermoelectrics," J. Appl. Phys. **111**(5), 054313 (2012).
[268]M. Mirjolet, F. Sánchez, and J. Fontcuberta, "High carrier mobility, electrical conductivity, and optical transmittance in epitaxial $SrVO_3$ thin films," Adv. Funct. Mater. **29**(14), 1808432 (2019).
[269]H.-R. Liu, J.-H. Yang, H. J. Xiang, X. G. Gong, and S.-H. Wei, "Origin of the superior conductivity of perovskite $Ba(Sr)SnO_3$," Appl. Phys. Lett. **102**(11), 112109 (2013).
[270]H. Kim, N. A. Charipar, and A. Piqué, "Tunable permittivity of La-doped $BaSnO_3$ thin films for near- and mid-infrared plasmonics," J. Phys. D **53**(36), 365103 (2020).
[271]C. A. Niedermeier, S. Rhode, K. Ide, H. Hiramatsu, H. Hosono, T. Kamiya, and M. A. Moram, "Electron effective mass and mobility limits in degenerate perovskite stannate $BaSnO_3$," Phys. Rev. B **95**(16), 161202 (2017).
[272]H. Yang, A. Konečná, X. Xu, S. Cheong, E. Garfunkel, F. J. García de Abajo, and P. E. Batson, "Low-loss tunable infrared plasmons in the high-mobility perovskite $(Ba,La)SnO_3$," Small **18**(16), 2106897 (2022).
[273]H. J. Kim, U. Kim, T. H. Kim, J. Kim, H. M. Kim, B.-G. Jeon, W.-J. Lee, H. S. Mun, K. T. Hong, J. Yu, K. Char, and K. H. Kim, "Physical properties of transparent perovskite oxides $(Ba,La)SnO_3$ with high electrical mobility at room temperature," Phys. Rev. B **86**(16), 165205 (2012).
[274]H. Kim, G. Kim, Y. Jeon, W. Lee, B. Lee, I. S. Kim, K. Lee, S. J. Kim, and J. Kim, "Perovskite lanthanum-doped barium stannate: A refractory near-zero-index material for high-temperature energy harvesting systems," Adv. Sci. **11**(2), 2302410 (2023).
[275]A. J. E. Rowberg, K. Krishnaswamy, and C. G. Van de Walle, "Prospects for high carrier mobility in the cubic germanates," Semicond. Sci. Technol. **35**(8), 085030 (2020).
[276]E. Baba, D. Kan, Y. Yamada, M. Haruta, H. Kurata, Y. Kanemitsu, and Y. Shimakawa, "Optical and transport properties of transparent conducting La-doped $SrSnO_3$ thin films," J. Phys. D **48**(45), 455106 (2015).
[277]E. Moreira, J. M. Henriques, D. L. Azevedo, E. W. S. Caetano, V. N. Freire, and E. L. Albuquerque, "Structural, optoelectronic, infrared and Raman spectra of orthorhombic $SrSnO_3$ from DFT calculations," J. Solid State Chem. **184**(4), 921–928 (2011).
[278]A. Prakash and B. Jalan, "Wide bandgap perovskite oxides with high room-temperature electron mobility," Adv. Mater. Interfaces **6**(15), 1900479 (2019).
[279]H. Wang, H. Huang, and B. Wang, "First-principles study of structural, electronic, and optical properties of $ZnSnO_3$," Solid State Commun. **149**, 1849–1852 (2009).
[280]F. M. Chiabrera, S. Yun, Y. Li, R. T. Dahm, H. Zhang, C. K. R. Kirchert, D. v Christensen, F. Trier, T. S. Jespersen, and N. Pryds, "Freestanding perovskite oxide films: Synthesis, challenges, and properties," Ann. Phys. **534**(9), 2200084 (2022).
[281]J. H. Montoya, M. Aykol, A. Anapolsky, C. B. Gopal, P. K. Herring, J. S. Hummelshøj, L. Hung, H. K. Kwon, D. Schweigert, S. Sun, S. K. Suram, S. B. Torrisi, A. Trewartha, and B. D. Storey, "Toward autonomous materials research: Recent progress and future challenges," Appl. Phys. Rev. **9**(1), 011405 (2022).
[282]M. L. Green, C. L. Choi, J. R. Hattrick-Simpers, A. M. Joshi, I. Takeuchi, S. C. Barron, E. Campo, T. Chiang, S. Empedocles, J. M. Gregoire, A. G. Kusne, J.

Martin, A. Mehta, K. Persson, Z. Trautt, J. Van Duren, and A. Zakutayev, "Fulfilling the promise of the materials genome initiative with high-throughput experimental methodologies," Appl. Phys. Rev. **4**(1), 011105 (2017).
[283]M. L. Green, B. Maruyama, and J. Schrier, "Autonomous (AI-driven) materials science," Appl. Phys. Rev. **9**(3), 030401 (2022).
[284]E. M. Garrity, C.-W. Lee, P. Gorai, M. B. Tellekamp, A. Zakutayev, and V. Stevanović, "Computational identification of ternary wide-band-gap oxides for high-power electronics," PRX Energy **1**(3), 033006 (2022).
[285]B. M. Bolotovskii and S. N. Stolyarov, "Reflection of light from a moving mirror and related problems," Usp. Fiz. Nauk **159**(9), 155 (1989).
[286]C. Yamanaka, T. Yamanaka, J. Mizui, and N. Yamaguchi, "Self-phase modulation of laser light in a laser-produced plasma," Phys. Rev. A **11**(6), 2138–2141 (1975).
[287]S. C. Wilks, J. M. Dawson, W. B. Mori, T. Katsouleas, and M. E. Jones, "Photon accelerator," Phys. Rev. Lett. **62**(22), 2600 (1989).
[288]R. L. Savage, C. Joshi, and W. B. Mori, "Frequency upconversion of electromagnetic radiation upon transmission into an ionization front," Phys. Rev. Lett. **68**(7), 946 (1992).
[289]A. J. Howard, D. Turnbull, A. S. Davies, P. Franke, D. H. Froula, and J. P. Palastro, "Photon acceleration in a flying focus," Phys. Rev. Lett. **123**, 124801 (2019).
[290]A. Nishida, N. Yugami, T. Higashiguchi, T. Otsuka, F. Suzuki, M. Nakata, Y. Sentoku, and R. Kodama, "Experimental observation of frequency upconversion by flash ionization," Appl. Phys. Lett. **101**(16), 161118 (2012).
[291]J. T. José and T. Mendonça, *Theory of Photon Acceleration* (Institute of Physics Pub, 2001).
[292]E. Galiffi, R. Tirole, S. Yin, H. Li, S. Vezzoli, P. A. Huidobro, M. G. Silveirinha, R. Sapienza, A. Alù, and J. B. Pendry, "Photonics of time-varying media," Adv. Photonics **4**(1), 014002 (2022).
[293]N. Somaschi, V. Giesz, L. De Santis, J. C. Loredo, M. P. Almeida, G. Hornecker, S. L. Portalupi, T. Grange, C. Antón, J. Demory, C. Gómez, I. Sagnes, N. D. Lanzillotti-Kimura, A. Lemaítre, A. Auffeves, A. G. White, L. Lanco, and P. Senellart, "Near-optimal single-photon sources in the solid state," Nat. Photonics **10**(5), 340–345 (2016).
[294]X. Wang, X. Jiao, B. Wang, Y. Liu, X. P. Xie, M. Y. Zheng, Q. Zhang, and J. W. Pan, "Quantum frequency conversion and single-photon detection with lithium niobate nanophotonic chips," npj Quantum Inf. **9**(1), 38 (2023).
[295]N. Lo Piparo, W. J. Munro, and K. Nemoto, "Quantum multiplexing," Phys. Rev. A **99**(2), 022337 (2019).
[296]N. Sinclair, E. Saglamyurek, H. Mallahzadeh, J. A. Slater, M. George, R. Ricken, M. P. Hedges, D. Oblak, C. Simon, W. Sohler, and W. Tittel, "Spectral multiplexing for scalable quantum photonics using an atomic frequency comb quantum memory and feed-forward control," Phys. Rev. Lett. **113**(5), 053603 (2014).
[297]J. Lawall, V. Verma, Q. Li, S. Höfling, J. Liu, A. Singh, C. Schneider, Y. Yu, X. Lu, K. Srinivasan, S. Liu, S. W. Nam, and R. Mirin, "Quantum frequency conversion of a quantum dot single-photon source on a nanophotonic chip," Optica **6**(5), 563–569 (2019).
[298]S. Vezzoli, V. Bruno, C. Devault, T. Roger, V. M. Shalaev, A. Boltasseva, M. Ferrera, M. Clerici, A. Dubietis, and D. Faccio, "Optical time reversal from time-dependent epsilon-near-zero media," Phys. Rev. Lett. **120**(4), 043902 (2018).
[299]G. Lerosey, J. de Rosny, A. Tourin, A. Derode, G. Montaldo, and M. Fink, "Time reversal of electromagnetic waves," Phys. Rev. Lett. **92**(19), 193904 (2004).
[300]J. B. Pendry, "Time reversal and negative refraction," Science **322**(5898), 71–73 (2008).
[301]M. Mounaix, N. K. Fontaine, D. T. Neilson, R. Ryf, H. Chen, J. C. Alvarado-Zacarias, and J. Carpenter, "Time reversed optical waves by arbitrary vector spatiotemporal field generation," Nat. Commun. **11**(1), 5813 (2020).
[302]O. Katz, E. Small, Y. Bromberg, and Y. Silberberg, "Focusing and compression of ultrashort pulses through scattering media," Nat. Photonics **5**(6), 372–377 (2011).
[303]X. Guo, Y. Ding, Y. Duan, and X. Ni, "Nonreciprocal metasurface with space–time phase modulation," Light **8**(1), 123 (2019).
[304]D. L. Sounas and A. Alù, "Non-reciprocal photonics based on time modulation," Nat. Photonics **11**(12), 774–783 (2017).
[305]Z. Yu and S. Fan, "Complete optical isolation created by indirect interband photonic transitions," Nat. Photonics **3**(2), 91–94 (2009).
[306]C. Caloz, N. Chamanara, and A. Akbarzadeh, "Inverse prism based on temporal discontinuity and spatial dispersion," Opt. Lett. **43**(14), 3297–3300 (2018).
[307]P. Y. Chen and A. Alù, "Subwavelength imaging using phase-conjugating nonlinear nanoantenna arrays," Nano Lett. **11**(12), 5514–5518 (2011).
[308]A. P. Mosk, A. Lagendijk, G. Lerosey, and M. Fink, "Controlling waves in space and time for imaging and focusing in complex media," Nat. Photonics **6**(5), 283–292 (2012).
[309]N. A. Estep, D. L. Sounas, J. Soric, and A. Alù, "Magnetic-free non-reciprocity and isolation based on parametrically modulated coupled-resonator loops," Nat. Phys. **10**(12), 923–927 (2014).
[310]X. Wang, V. S. Asadchy, S. Fan, and S. A. Tretyakov, "Space-time metasurfaces for power combining of waves," ACS Photonics **8**(10), 3034–3041 (2021).
[311]J. T. Mendonça, A. M. Martins, and A. Guerreiro, "Temporal beam splitter and temporal interference," Phys. Rev. A **68**, 043801 (2003).
[312]P. A. Huidobro, E. Galiffi, S. Guenneau, R. V. Craster, and J. B. Pendry, "Fresnel drag in space–time-modulated metamaterials," Proc. Natl. Acad. Sci. U. S. A. **116**(50), 24943–24948 (2019).
[313]E. Galiffi, Y. T. Wang, Z. Lim, J. B. Pendry, A. Alù, and P. A. Huidobro, "Wood anomalies and surface-wave excitation with a time grating," Phys. Rev. Lett. **125**(12), 127403 (2020).
[314]B. W. Plansinis, W. R. Donaldson, and G. P. Agrawal, "Temporal waveguides for optical pulses," J. Opt. Soc. Am. B **33**(6), 1112–1119 (2016).
[315]V. Pacheco-Peña and N. Engheta, "Antireflection temporal coatings," Optica **7**(4), 323–331 (2020).
[316]V. Pacheco-Peña and N. Engheta, "Temporal aiming," Light **9**(1), 129 (2020).
[317]M. Karimi, M. Z. Alam, J. Upham, O. Reshef, and R. W. Boyd, "Time-varying gradient metasurface with applications in all-optical beam steering," Nanophotonics **12**(9), 1733–1740 (2023).
[318]J. Baxter and L. Ramunno, "Inverse design of optical pulse shapes for time-varying photonics," Opt. Express **31**(14), 22671–22684 (2023).
[319]R. Tirole, S. Vezzoli, E. Galiffi, I. Robertson, D. Maurice, B. Tilmann, S. A. Maier, J. B. Pendry, and R. Sapienza, "Double-slit time diffraction at optical frequencies," Nat. Phys. **19**, 999 (2023).
[320]H. Moussa, G. Xu, S. Yin, E. Galiffi, Y. Ra'di, and A. Alù, "Observation of temporal reflection and broadband frequency translation at photonic time interfaces," Nat. Phys. **19**, 863–868 (2023).
[321]G. Castaldi, C. Rizza, N. Engheta, and V. Galdi, "Multiple actions of time-resolved short-pulsed metamaterials," Appl. Phys. Lett. **122**(2), 021701 (2023).
[322]M. R. Shcherbakov, K. Werner, Z. Fan, N. Talisa, E. Chowdhury, and G. Shvets, "Photon acceleration and tunable broadband harmonics generation in nonlinear time-dependent metasurfaces," Nat. Commun. **10**(1), 1345 (2019).
[323]C. Liu, M. Zahirul Alam, K. Pang, K. Manukyan, O. Reshef, Y. Zhou, S. Choudhary, J. Patrow, A. Pennathurs, H. Song, Z. Zhao, R. Zhang, F. Alishahi, A. Fallahpour, Y. Cao, A. Almaiman, J. M. Dawlaty, M. Tur, R. W. Boyd, and A. E. Willner, "Photon acceleration using a time-varying epsilon-near-zero metasurface," ACS Photonics **8**, 716 (2021).
[324]M. F. Yanik and S. Fan, "Time reversal of light with linear optics and modulators," Phys. Rev. Lett. **93**(17), 173903 (2004).
[325]E. Lustig, S. Saha, E. Bordo, C. Devault, S. N. Chowdhury, Y. Sharabi, A. Boltasseva, O. Cohen, V. M. Shalaev, and M. Segev, "Towards photonic time-crystals: Observation of a femtosecond time-boundary in the refractive index," in Conference on Lasers and Electro-Optics (CLEO), 2021.
[326]X. Wang, M. S. Mirmoosa, V. S. Asadchy, C. Rockstuhl, S. Fan, and S. A. Tretyakov, "Metasurface-based realization of photonic time crystals," Sci. Adv. **9**(14), eadg7541 (2022).
[327]S. Saha, O. Segal, C. Fruhling, E. Lustig, M. Segev, A. Boltasseva, and V. Shalaev, "Photonic time crystals: A materials perspective," Opt. Express **31**(5), 8267 (2023).
[328]R. T. Sandberg and A. G. R. Thomas, "Photon acceleration from optical to XUV," Phys. Rev. Lett. **130**(8), 085001 (2023).
[329]N. Karl, P. P. Vabishchevich, M. R. Shcherbakov, S. Liu, M. B. Sinclair, G. Shvets, and I. Brener, "Frequency conversion in a time-variant dielectric metasurface," Nano Lett. **20**(10), 7052–7058 (2020).

[330]M. Ghulinyan, F. Riboli, L. Pavesi, A. Recati, Z. Gaburro, and I. Carusotto, "Photon energy lifter," Opt. Express **14**(16), 7270–7278 (2006).
[331]L. O. Silva and J. T. Mendonça, "Photon kinetic theory of self-phase modulation," Opt. Commun. **196**(1–6), 285–291 (2001).
[332]C. J. Krückel, A. Fülöp, T. Klintberg, J. Bengtsson, P. A. Andrekson, and V. Torres-Company, "Linear and nonlinear characterization of low-stress high-confinement silicon-rich nitride waveguides," Opt. Express **23**(20), 25827 (2015).
[333]H.-P. Lo and H. Takesue, "Precise tuning of single-photon frequency using an optical single sideband modulator," Optica **4**(8), 919–923 (2017).
[334]M. Izutsu, T. Sueta, and S. Shikama, "Integrated optical SSB modulator/frequency shifter," IEEE J. Quantum Electron. **17**(11), 2225–2227 (1981).
[335]V. Bacot, G. Durey, A. Eddi, M. Fink, and E. Fort, "Phase-conjugate mirror for water waves driven by the Faraday instability," Proc. Natl. Acad. Sci. U. S. A. **116**(18), 8809–8814 (2019).
[336]M. Notomi, H. Taniyama, S. Mitsugi, and E. Kuramochi, "Optomechanical wavelength and energy conversion in high-Q double-layer cavities of photonic crystal slabs," Phys. Rev. Lett. **97**(2), 023903 (2006).
[337]Z. Y. Cheng and C. S. Tsai, "Baseband integrated acousto-optic frequency shifter," Appl. Phys. Lett. **60**(1), 12–14 (1992).
[338]Z. Wu and A. Grbic, "Serrodyne frequency translation using time-modulated metasurfaces," IEEE Trans. Antennas Propag. **68**(3), 1599–1606 (2020).
[339]T. Baba and K. Kondo, "Co- and counter-propagating slow light systems," Proc. SPIE **9763**, 97631C (2016).
[340]A. Blanco-Redondo, C. Husko, D. Eades, Y. Zhang, J. Li, T. F. Krauss, and B. J. Eggleton, "Observation of soliton compression in silicon photonic crystals," Nat. Commun. **5**(1), 3160 (2014).
[341]T. Tanabe, M. Notomi, H. Taniyama, and E. Kuramochi, "Dynamic release of trapped light from an ultrahigh-Q nanocavity via adiabatic frequency tuning," Phys. Rev. Lett. **102**(4), 043907 (2009).
[342]M. Notomi and S. Mitsugi, "Wavelength conversion via dynamic refractive index tuning of a cavity," Phys. Rev. A **73**(5), 051803 (2006).
[343]K. Kondo and T. Baba, "Dynamic wavelength conversion in copropagating slow-light pulses," Phys. Rev. Lett. **112**(22), 223904 (2014).
[344]K. Kondo and T. Baba, "Slow-light-induced Doppler shift in photonic-crystal waveguides," Phys. Rev. A **93**(1), 011802 (2016).
[345]W. Yoshiki, Y. Honda, M. Kobayashi, T. Tetsumoto, and T. Tanabe, "Kerr-induced controllable adiabatic frequency conversion in an ultrahigh Q silica toroid microcavity," Opt. Lett. **41**(23), 5482 (2016).
[346]S. F. Preble, Q. Xu, and M. Lipson, "Changing the colour of light in a silicon resonator," Nat. Photonics **1**(5), 293–296 (2007).
[347]M. F. Yanik and S. Fan, "Stopping light all optically," Phys. Rev. Lett. **92**(8), 083901 (2004).
[348]E. J. Reed, M. Soljačić, and J. D. Joannopoulos, "Color of shock waves in photonic crystals," Phys. Rev. Lett. **90**(20), 203904 (2003).
[349]J. Upham, Y. Tanaka, T. Asano, and S. Noda, "On-the-fly wavelength conversion of photons by dynamic control of photonic waveguides," Appl. Phys. Express **3**(6), 062001 (2010).
[350]M. Castellanos Muñoz, A. Yu. Petrov, and M. Eich, "All-optical on-chip dynamic frequency conversion," Appl. Phys. Lett. **101**(14), 141119 (2012).
[351]P. Moitra, Y. Yang, Z. Anderson, I. I. Kravchenko, D. P. Briggs, and J. Valentine, "Realization of an all-dielectric zero-index optical metamaterial," Nat. Photonics **7**(10), 791–795 (2013).
[352]A. M. Shaltout, A. V. Kildishev, and V. M. Shalaev, "Evolution of photonic metasurfaces: From static to dynamic," J. Opt. Soc. Am. B **33**(3), 501 (2016).
[353]A. Shaltout, A. Kildishev, and V. Shalaev, "Time-varying metasurfaces and Lorentz non-reciprocity," Opt. Mater. Express **5**(11), 2459 (2015).
[354]A. M. Shaltout, M. Clerici, N. Kinsey, R. Kaipurath, J. Kim, E. G. Carnemolla, D. Faccio, A. Boltasseva, V. M. Shalaev, and M. Ferrera, "Doppler-shift emulation using highly time-refracting TCO layer," in Conference on Lasers and Electro-Optics (CLEO), 2016.
[355]D. M. Beggs, T. F. Krauss, L. Kuipers, and T. Kampfrath, "Ultrafast tilting of the dispersion of a photonic crystal and adiabatic spectral compression of light pulses," Phys. Rev. Lett. **108**, 033902 (2012).
[356]F. Miyamaru, C. Mizuo, T. Nakanishi, Y. Nakata, K. Hasebe, S. Nagase, Y. Matsubara, Y. Goto, J. Pérez-Urquizo, J. Madéo, and K. M. Dani, "Ultrafast frequency-shift dynamics at temporal boundary induced by structural-dispersion switching of waveguides," Phys. Rev. Lett. **127**, 053902 (2021).
[357]C. Liu, C. Liu, M. Z. Alam, M. Z. Alam, K. Pang, K. Manukyan, J. R. Hendrickson, E. M. Smith, E. M. Smith, Y. Zhou, O. Reshef, H. Song, R. Zhang, H. Song, F. Alishahi, A. Fallahpour, A. Almaiman, R. W. Boyd, R. W. Boyd, M. Tur, and A. E. Willner, "Tunable Doppler shift using a time-varying epsilon-near-zero thin film near 1550 nm," Opt. Lett. **46**(14), 3444–3447 (2021).
[358]V. Bruno, S. Vezzoli, C. DeVault, E. Carnemolla, M. Ferrera, A. Boltasseva, V. M. Shalaev, D. Faccio, and M. Clerici, "Broad frequency shift of parametric processes in epsilon-near-zero time-varying media," Appl. Sci. **10**(4), 1318 (2020).
[359]Y. Zhou, M. Z. Alam, M. Karimi, J. Upham, O. Reshef, C. Liu, A. E. Willner, and R. W. Boyd, "Broadband frequency translation through time refraction in an epsilon-near-zero material," Nat. Commun. **11**(1), 2180 (2020).
[360]J. Bohn, T. S. Luk, S. Horsley, and E. Hendry, "Spatiotemporal refraction of light in an epsilon-near-zero indium tin oxide layer: Frequency shifting effects arising from interfaces," Optica **8**(12), 1532 (2021).
[361]K. Pang, M. Z. Alam, Y. Zhou, C. Liu, O. Reshef, K. Manukyan, M. Voegtle, A. Pennathur, C. Tseng, X. Su, H. Song, Z. Zhao, R. Zhang, H. Song, N. Hu, A. Almaiman, J. M. Dawlaty, R. W. Boyd, M. Tur, and A. E. Willner, "Adiabatic frequency conversion using a time-varying epsilon-near-zero metasurface," Nano Lett. **21**(14), 5907–5913 (2021).
[362]A. M. Shaltout, M. Clerici, N. Kinsey, R. Kaipurath, J. Kim, E. G. Carnemolla, D. Faccio, A. Boltasseva, V. M. Shalaev, and M. Ferrera, "Doppler-shift emulation using highly time-refracting TCO layer," in Conference on Lasers and Electro-Optics, 2016.
[363]M. Scalora, J. Trull, D. De Ceglia, M. A. Vincenti, N. Akozbek, Z. Coppens, L. Rodríguez-Suné, and C. Cojocaru, "Electrodynamics of conductive oxides: Intensity-dependent anisotropy, reconstruction of the effective dielectric constant and harmonic generation," Phys. Rev. A **101**(5), 053828 (2020).
[364]R. Tirole, E. Galiffi, J. Dranczewski, T. Attavar, B. Tilmann, Y. T. Wang, P. A. Huidobro, A. Alú, J. B. Pendry, S. A. Maier, S. Vezzoli, and R. Sapienza, "Saturable time-varying mirror based on an epsilon-near-zero material," Phys. Rev. Appl. **18**(5), 054067 (2022).
[365]J. B. Khurgin, "Photonic time crystals and parametric amplification: Similarity and distinction," arXiv:2305.15243 (2023).
[366]J. Baxter, A. Pérez-Casanova, L. Cortes-Herrera, A. C. Lesina, I. De Leon, and L. Ramunno, "Dynamic nanophotonics in epsilon-near-zero conductive oxide films and metasurfaces: A quantitative, nonlinear, computational model," Adv. Photonics Res. **4**(3), 2200280 (2023).
[367]V. G. Veselago, "The electrodynamics of substances with simultaneously negative values of ε and μ," Sov. Phys. Usp. **10**(4), 509 (1968).
[368]G. Lerosey, J. De Rosny, A. Tourin, and M. Fink, "Focusing beyond the diffraction limit with far-field time reversal," Science **315**(5815), 1120–1122 (2007).
[369]F. R. Morgenthaler, "Velocity modulation of electromagnetic waves," IEEE Trans. Microwave Theory Tech. **6**(2), 167–172 (1958).
[370]R. L. Fante, "Transmission of electromagnetic waves into time-varying media," IEEE Trans. Antennas Propag. **19**(3), 417–424 (1971).
[371]T. M. Ruiz, C. L. Wright, and J. Smith, "Characteristics of electromagnetic waves propagating in time varying media," IEEE Trans. Antennas Propag. **26**(2), 358–361 (1978).
[372]L. B. Felsen and G. M. Whitman, "Wave propagation in time-varying media," IEEE Trans. Antennas Propag. **18**(2), 242–253 (1970).
[373]J. C. AuYeung, "Phase-conjugate reflection from a temporal dielectric boundary," Opt. Lett. **8**(3), 148–150 (1983).
[374]Z. Hayran, J. B. Khurgin, and F. Monticone, "$\hbar\omega$ versus $\hbar k$: Dispersion and energy constraints on time-varying photonic materials and time crystals [Invited]," Opt. Mater. Express **12**(10), 3904 (2022).
[375]V. Bacot, M. Labousse, A. Eddi, M. Fink, and E. Fort, "Time reversal and holography with spacetime transformations," Nat. Phys. **12**(10), 972–977 (2016).
[376]M. Fink and C. Prada, "Acoustic time-reversal mirrors," Inverse Probl. **17**(1), R1 (2001).
[377]A. Yariv, "Phase conjugate optics and realtime holography," IEEE J. Quantum Electron. **14**(9), 650–660 (1978).
[378]D. A. B. Miller, "Time reversal of optical pulses by four-wave mixing," Opt. Lett. **5**(7), 300–302 (1980).
[379]J. H. Marburger, "Optical pulse integration and chirp reversal in degenerate four-wave mixing," Appl. Phys. Lett. **32**(6), 372–374 (1978).

[380]R. W. Hellwarth, "Generation of time-reversed wave fronts by nonlinear refraction," J. Opt. Soc. Am. **67**(1), 1–3 (1977).
[381]S. M. Rao, A. Lyons, T. Roger, M. Clerici, N. I. Zheludev, and D. Faccio, "Geometries for the coherent control of four-wave mixing in graphene multilayers," Sci. Rep. **5**(1), 15399 (2015).
[382]J. D. Joannopoulos, P. R. Villeneuve, and S. Fan, "Photonic crystals: Putting a new twist on light," Nature **386**(6621), 143–149 (1997).
[383]Y. Sharabi, E. Lustig, and M. Segev, "Topological aspects of photonic time crystals," Optica **5**(11), 1390–1395 (2018).
[384]Y. Sharabi, E. Lustig, A. Dikopoltsev, Y. Lumer, and M. Segev, "Spatiotemporal photonic crystals," Optica **9**(6), 585–592 (2022).
[385]E. Lustig, O. Segal, S. Saha, C. Fruhling, V. M. Shalaev, A. Boltasseva, and M. Segev, "Photonic time-crystals—fundamental concepts [Invited]," Opt. Express **31**(6), 9165–9170 (2023).
[386]F. Wilczek, "Quantum time crystals," Phys. Rev. Lett. **109**(16), 160401 (2012).
[387]M. Lyubarov, Y. Lumer, A. Dikopoltsev, E. Lustig, Y. Sharabi, and M. Segev, "Amplified emission and lasing in photonic time crystals," Science **377**(6604), 425–428 (1979).
[388]A. M. Shaltout, J. Fang, A. V. Kildishev, and V. M. Shalaev, "Photonic time-crystals and momentum band-gaps," in Conference on Lasers and Electro-Optics, 2016.
[389]J. R. Zurita-Sánchez and P. Halevi, "Resonances in the optical response of a slab with time-periodic dielectric function $\varepsilon(t)$," Phys. Rev. A **81**(5), 053834 (2010).
[390]X. Wang, M. S. Mirmoosa, V. S. Asadchy, C. Rockstuhl, S. Fan, and S. A. Tretyakov, "Metasurface-based realization of photonic time crystals," Sci. Adv. **9**(14), eadg7541 (2023).
[391]E. Lustig, O. Segal, S. Saha, E. Bordo, S. N. Chowdhury, Y. Sharabi, A. Fleischer, A. Boltasseva, O. Cohen, V. M. Shalaev, and M. Segev, "Time-refraction optics with single cycle modulation," Nanophotonics **12**(12), 2221–2230 (2023).